DIRECT SIMULATION OF FLEXIBLE PARTICLE SUSPENSIONS USING LATTICE–BOLTZMANN EQUATION WITH EXTERNAL BOUNDARY FORCE

A Thesis
Presented to
The Academic Faculty

by

Jingshu Wu

In Partial Fulfillment
of the Requirements for the Degree
Doctor of Philosophy in the
School of Mechanical Engineering

Georgia Institute of Technology
May 12 2010

DIRECT SIMULATION OF FLEXIBLE PARTICLE SUSPENSIONS USING LATTICE–BOLTZMANN EQUATION WITH EXTERNAL BOUNDARY FORCE

Approved by:

Dr. Cyrus K. Aidun, Advisor,
Committee Chair
School of Mechanical Engineering
Georgia Institute of Technology

Dr. Ajit P. Yoganathan, Co–Advisor
Department of Biomedical Engineering
Georgia Institute of Technology

Dr. S. Mostafa Ghiaasiaan
School of Mechanical Engineering
Georgia Institute of Technology

Dr. Marc K. Smith
School of Mechanical Engineering
Georgia Institute of Technology

Dr. Thorsten Stoesser
School of Civil and Environmental
Engineering
Georgia Institute of Technology

Dr. Victor Breedveld
School of Chemical and Biomolecular
Engineering
Georgia Institute of Technology

Date Approved: 17 March 2010

To my family,

Mama, Baba, Jiejie, Jiefu, Yuzi and Xizi

and my love, Quanquan

and our babies...

ACKNOWLEDGEMENTS

There are so many people whom I would like to acknowledge for their support, guidance, encouragement and friendship during my study at Georgia Tech. First, I would like to express my sincere thanks to my advisor, Dr. Cyrus Aidun who supported me, guided me and helped me during my PhD study. I have learned a great deal from him about both performing scientific research and managing time to complete the many tasks at the same time. I wish to thank Dr. Ajit Yoganathan, for his support and guidance in the last year of my PhD study. I would also like to thank Dr. Lakshmi Sankar, He gave me the best of the opportunities to discover the fascinating world of numerical simulation during my study at the school of aerospace engineering.

The members of the thesis committee: Dr. Victor Breedveld, Dr. Mostafa Ghiaasiaan, Dr. Marc Smith and Dr. Thorsten Stoesser has also enlightened me with their insights and criticisms. Special thanks go to Dr. Ejiang Ding, who was always so patient with me and taught me so much about lattice–Boltzmann method. He is more than a mentor and friend to me. I would like to thank all the past and present members of the lattice–Boltzmann research group, and the cardiovascular fluid mechanics research group. Each of them, in their own way, helped me go through the frustrating times of doing research :-p

Finally, last but not least, I could not have accomplished any of this without the support of my family, especially my lovely wife, Dan Wan. You were always there for me, help me, ready to listen, give wise advices, cheer me up. Thank you for your support, your patience... and for just being quanquan. You cooking is the BEST of the BEST! :-)

To all of you, Xiexie!

TABLE OF CONTENTS

LIST OF TABLES

LIST OF FIGURES

LIST OF SYMBOLS OR ABBREVIATIONS

$\boldsymbol{\sigma}$	Suspension stress tensor.
$\boldsymbol{E}$	Strain rate tensor.
$\boldsymbol{e}_k$	Discrete velocity vector for LBM.
$\boldsymbol{e_x}$	Unit vector on the flow direction.
$\boldsymbol{e_y}$	Unit vector on the velocity gradient direction.
$\boldsymbol{e_z}$	Unit vector on the vorticity axis direction.
$\boldsymbol{F}^{con}$	Contact force.
$\boldsymbol{F}^{ele}$	Electrical force.
$\boldsymbol{F}^{ext}$	External force.
$\boldsymbol{F}^{fsi}$	Force per unit volume acting on solid.
$\boldsymbol{F}_i$	Total force of the ith particle.
$\boldsymbol{F}_i^{sT}$	Spring force of the ith particle.
$\boldsymbol{F}^{lub}$	Lubrication force.
$\boldsymbol{g}$	Force per unit volume acting on fluid.
$\boldsymbol{\Omega}_i$	Angular velocity of the ith particle.
$\boldsymbol{I}_i$	Inertial tensor of the ith particle.
$\boldsymbol{p}$	Unit vector parallel to the fiber axis of symmetry.
$\boldsymbol{r}_{ij}$	Length between node i and j in LSM.
$\boldsymbol{r}_{ij}^{eq}$	The force free equilibrium spring length between node i and j in LSM.
$\boldsymbol{r}_{in}$	Position vector of hinge n in fiber i.
$\boldsymbol{r}_{jm}$	Position vector of hinge m in fiber j.
$\boldsymbol{T}_i$	Total torque of the ith particle.
$\boldsymbol{u}$	Fluid velocity.
$\boldsymbol{U}_f$	Fluid velocity at fluid–solid boundary.

$\boldsymbol{U}_i$	Velocity of the ith particle.
$\boldsymbol{U}_p$	Particle velocity at fluid–solid boundary.
$\boldsymbol{V}_{in}$	Velocity of hinge n in fiber i.
$\boldsymbol{V}_{in-jm}^{lub}$	Relative velocity component for lubrication force calculation.
$\boldsymbol{V}_{jm}$	Velocity of hinge m in fiber j.
$\boldsymbol{x}$	Position vector.
$\boldsymbol{x}_{ij}^l$	Position vector for the jth node on ith particle.
$\boldsymbol{x}_i^{lc}$	Center of gravity of the ith particle.
$\boldsymbol{Y}_{in}^b$	Bending moment on hinge n in fiber i.
$\boldsymbol{Y}_{in}^t$	Twisting moment on hinge n in fiber i.
BR	Fiber bending ratio.
Ca_P	Capillary number.
Ca_S	Shear Capillary number.
C_b	Orbit constant.
C_I	Interaction parameter for Folgar and Tucker's model.
C_j	Jeffery orbit constant.
C_r	Courant number.
c_s	Pseudo speed of sound.
c_{vf}	Fiber volume fraction.
D	Fiber diameter.
Δt^{LBM}	LBM time step.
Δx^{LBM}	Unit grid size of LBM.
Δx^{LSM}	Unit grid size of LSM.
DI_P	Deformation index of RBC.
$\dot{\gamma}$	Shear rate.
D_r	Brownian rotary diffusion coefficient.

D_{rDE}	Brownian rotary diffusion coefficient for Doi and Edwards's model.
EBF	External boundary force.
E_G	Shear modulus.
E_i	Elastic energy associated with the ith node for LSM.
η	Relative shear viscosity.
η^B	Relative shear viscosity from Batchelor's relation.
E_Y	Young's modulus.
FEM	Finite element methods.
f_k	LBM distribution function.
f_k^{eq}	LBM equilibrium distribution function.
FVM	Finite volume methods.
Γ	Fluid–solid boundary.
Γ_f	Set of fluid boundary nodes.
Γ_s	Set of solid boundary nodes.
Pe	Peclet number.
Re	Reynolds number.
κ	Flow confinement ratio.
k_B	Boltzmann constant.
K_c	Constant for Carter's model.
L	Fiber length.
LBM	Lattice Boltzmann method.
LDV	Laser Doppler velocimetry.
$\langle n_c \rangle$	Average number of contact points per fiber.
LSM	Lattice–spring model.
M_i	Mass of the ith particle.
m_i	Mass assigned to each node in LSM.

μ_{eff}	Effective shear viscosity.
μ_{fiber}	Dynamic viscosity parameter in Batchelor's equation.
n	The number of fiber per unit volume.
N	The number of rods per fiber.
N_1	First effective normal stress difference.
N_1^B	First effective normal stress difference from Batchelor's relation.
N_2	Second effective normal stress difference.
$p(C_b)$	Fiber orientation distribution function.
ϕ	Fiber orientation angle.
ϕ_0	Phase angle.
Π_f	Continuum fluid domain.
Π_f^M	Set of position vectors of the fluid nodes.
Π_s	Continuum solid domain.
Π_s^N	Set of position vectors of the solid nodes.
$p(\phi)$	Fiber orientation distribution function for ϕ.
RBC	Red blood cell.
r_e	Fiber effective aspect ratio.
ρ	Fluid density.
ρ_f	Fluid density.
r_p	Fiber aspect ratio.
SBB	Standard bounce–back.
T	Absolute temperature in degrees Kelvin.
τ	Single relaxation time constant for LBM.
θ	Fiber orientation angle between fiber axis and z axis.
T_p	Particle rotation period.
V_p	Volume of suspending particle.

SUMMARY

Determination of the relation between the bulk or rheological properties of a particle suspension and its microscopic structure is an old and important problem in physical science. In general, the rheology of particle suspension is quite complex, and the problem becomes even more complicated if the suspending particle is deformable. Despite these difficulties, a large number of theoretical and experimental investigations have been devoted to the analysis and prediction of the rheological behavior of particle suspensions. However, among these studies there are very few investigations that focus on the role of particle deformability.

A novel method for full coupling of the fluid–solid phases with sub–grid accuracy for the solid phase is developed. In this method, the flow is computed on a fixed regular 'lattice' using the lattice Boltzmann method (LBM), where each solid particle, or fiber, is mapped onto a Lagrangian frame moving continuously through the domain. The motion and orientation of the particle are obtained from Newtonian dynamics equations. The deformable particle is modeled by the lattice–spring model (LSM). The fiber deformation is calculated by an efficient flexible fiber model. The no–slip boundary condition at the fluid–solid interface is based on the external boundary force (EBF) method. This method is validated by comparing with known experimental and theoretical results.

The fiber simulation results show that the rheological properties of flexible fiber suspension are highly dependent on the microstructural characteristics of the suspension. It is shown that fiber stiffness (bending ratio BR) has strong impact on the suspension rheology in the range $BR < 3$. The relative viscosity of the fiber suspension under shear increases significantly as BR decreases. Direct numerical simulation

of flexible fiber suspension allows computation of the primary normal stress difference as a function of BR. These results show that the primary normal stress difference has a minimum value at $BR \sim 1$. The primary normal stress differences for slightly deformable fibers reaches a minimum and increases significantly as BR decreases below 1. The results are explained based on the Batchelor's relation for non–Brownian suspensions. The influence of fiber stiffness on the fiber orientation distribution and orbit constant is the major contributor to the variation in rheological properties. A least–squares curve–fitting relation for the relative viscosity is obtained for flexible fiber suspension. This relation can be used to predict the relative viscosity of flexible fiber suspension based on the result of rigid fiber suspension.

The unique capability of the LBM–EBF method for sub–grid resolution and multiscale analysis of particle suspension is applied to the challenging problem of platelet motion in blood flow. By computing the stress distribution over the platelet, the "blood damage index" is computed and compared with experiments in channels with various geometries [43]. In platelet simulation, the effect of 3D channel geometry on the platelet activation and aggregation is modeled by using LBM–EBF method. Comparison of our simulations with Fallon's experiments [43] shows a similar pattern, and shows that Dumont's BDI model [40] is more appropriate for blood damage investigation. It has been shown that channels with sharp transition geometry will have larger recirculation areas with high BDI values. By investigating the effect of hinge area geometry on BDI value, we intend to use this multiscale computational method to optimize the design of Bileaflet mechanical heart valves.

Both fiber simulations and platelet simulations have shown that the novel LBM–EBF method is more efficient and stable compare to the conventional numerical methods. The new EBF method is a two–way coupling method with sub–grid accuracy which makes the platelet simulations possible. The LBM–EBF is the only method to date, to the best of author's knowledge, that can simulate suspensions with large

number of deformable particles under complex flow conditions. It is hoped that future researchers may benefit from this new method and the algorithms developed here.

CHAPTER I

INTRODUCTION AND LITERATURE REVIEW

1.1 Background

Fluids with large numbers of particles are integral to many industrial and biological processes. The particles may be added to the fluid for the purpose of modifying the fluid's behavior as in paint; the interaction of particles may define the industrial product, as do fibers in paper making; or the particles may perform biological functions as do red blood cells and platelets. Newtonian fluids with suspensions usually show complex rheology and non–Newtonian flow characteristics. In some situations, the particles are deformable and make problems even more complicated. Treating these suspending particles as rigid particles ignores important physical behavior. For example, the effective viscosity of an actual fiber suspension is 7% to 13% larger than the equivalent rigid fiber suspension [46, 14, 54]. Understanding the underlying physical processes is very important in simulation and optimization of engineering applications.

Experimental techniques have certain drawbacks in these situations and the results are also critical for understanding the basic mechanism. It is difficult to measure the shape and deformation of deformable particles and rheological quantities such as self–diffusivities in experiments. Most experimental studies of the rheology of fiber suspensions have made an important contribution to the field, but the results are very system specific. Analytical solutions for both rigid and deformable particles are limited to dilute cases with simple and regular geometry. The existing numerical methods such as finite volume methods (FVM) or finite element methods (FEM) have proven too computationally expensive to perform large simulations. The "Immersed

boundary" and "Cartesian grid" methods can only handle rigid or high stiffness solid suspensions, and they use artificial penalty parameters which also affect the dynamics of suspensions. Regular LBM can simulate a large number of particles in the suspension, and is easy to parallelize, but it can cause instability under certain conditions. **An efficient and stable numerical technique to simulate flow with large numbers of deformable particles has not been published yet**, and the development of a novel method to simulate fluid–solid interaction, especially with deformable suspended particles, would improve the fundamental understanding of suspension rheology and microstructure.

It is very important to discover the relation between the bulk properties of a suspension and its microstructure. Volume concentration is the most widely used as a parameter in suspension of spherical particles. For fiber suspensions, however, this parameter, fiber volume fraction ($c_{vf} = nL\pi D^2/4$), is relatively meaningless when used alone. To classify the level of fiber concentration, this study follows Doi and Edwards's [38] classification of fiber concentration based on the value of nL^3, where n is the number of fibers per unit volume and L is the fiber length. In the dilute regime when $nL^3 < 1$, the fibers move without interference from other fibers. In the semi–dilute regime, $1 < nL^3 < L/D$, where D is the fiber diameter, some fiber contacts are possible. In the concentrated regime, $nL^3 > L/D$, fiber–fiber interaction is dominant. The fiber suspension parameters of relevance in this study are the fiber aspect ratio ($r_p = L/D$), fiber volume fraction ($c_{vf} = nL\pi D^2/4$) and fiber bending ratio (BR), which is the non–dimensional stiffness of the flexible fiber. It is defined by [46] and [52]

$$BR \equiv \frac{E_Y \left(\ln 2r_e - 1.5\right)}{2\left(\mu\dot{\gamma}\right){r_p}^4}. \tag{1}$$

Here, E_Y is the fiber Young's modulus, μ is the fluid viscosity and $\dot{\gamma}$ is the shear rate, and r_e is the effective aspect ratio.

2

Jeffery [69] has shown that an ellipsoidal particle will rotate in an orbit. Bretherton [18] expanded Jeffery's solution to any axisymmetric particle and used an effective aspect ratio r_e, which is equal to r_p for ellipsoidal particles. For a rigid cylinder of aspect ratio $r_p = L/D$, the equivalent aspect ratio has been derived by Cox [32], $r_e = 1.24r_p/\sqrt{\ln r_p}$. For a given suspending fiber and suspending fluid, BR decreases with increasing shear rate $\dot{\gamma}$. When the shear rate is higher than the critical shear rate $\dot{\gamma}_{crit}$, $BR < 1$, the suspending fiber is predicted to bend. Table 1 shows the critical shear rate for fibers with different material, suspended in castor oil, which has a viscosity of 5 Pa·s.

Table 1: The critical shear rate for fibers with different material, suspended in castor oil

Fiber Material	r_p	E_Y (GPa)	$\dot{\gamma}_{crit}$ (1/s)
Softwood Fibers	100	10.0	32.50
Hardwood Fibers	40	11.4	1088.56
Polypropylene	100	1.5	4.88
Nylon	100	3.0	9.75
Dacron	100	7.3	23.72
Rayon	100	26.4	85.80
Glass	100	50.0	162.49

For an axisymmetric slender particle in the Stokes flow of a Newtonian fluid, the governing equations are given by [69]

$$\dot{\phi} = \frac{\dot{\gamma}\left(r_e{}^2\cos^2\phi + \sin^2\phi\right)}{\left(r_e{}^2 + 1\right)}, \tag{2}$$

and

$$\dot{\theta} = \frac{\dot{\gamma}\left(r_e{}^2 - 1\right)\cos\phi\sin\phi\cos\theta\sin\theta}{\left(r_e{}^2 + 1\right)}. \tag{3}$$

Integrating equations (2) and (3) yields

$$\tan\phi = r_e\tan\left(\frac{2\pi t}{T_p} + \phi_0\right), \tag{4}$$
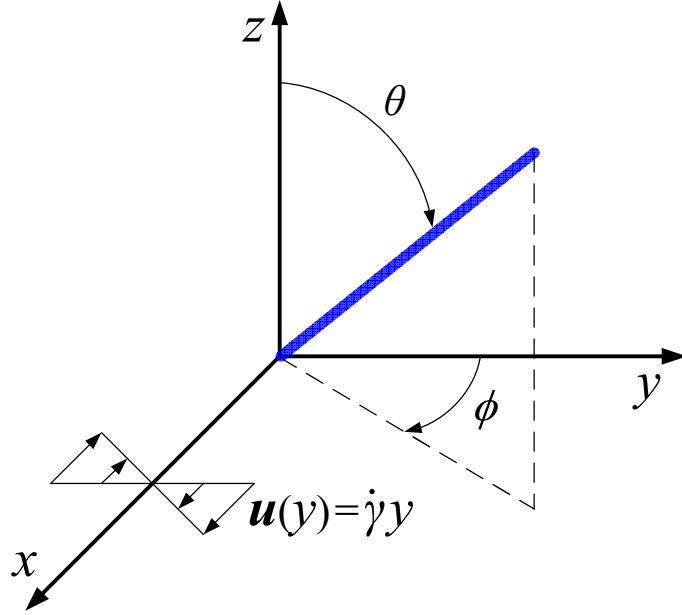
Figure 1.1: The spherical coordinate system for a fiber in an x, y simple shear flow.

$$\tan\theta = \frac{C_j r_e}{\left(r_e{}^2\cos^2\phi + \sin^2\phi\right)^{1/2}}, \tag{5}$$

respectively, where C_j and ϕ_0 are parameters known as the Jeffery orbit constant and phase angle, respectively. T_p is the particle rotation period. When $C_j = 0$, the fiber is oriented in the vorticity direction (z–direction). As C_j increases from 0, the orbits leave the vorticity axis and approach the flow velocity and its gradient plane (xy–plane). When $C_j = \infty$, the orbit is located in the xy–plane. It is advantageous to use $C_b \equiv C_j/(C_j + 1)$ since C_j takes values from 0 to ∞, while C_b is bound between 0 and 1. These equations show that the particle aspect ratio determines its angular velocity at different orientation angles. Long slender particles spend most of the time lined up in the flow direction and the 'flip–over' time is around $1/r_e$ of the rotation period.

If the position, orientation and velocity of every fiber at every time step are known, the microstructure of the fiber suspension can be described by the fiber orientation distribution function $p(C_b)$ and $p(\phi)$, the average number of contact points per fiber

$\langle n_c \rangle$, where the angle brackets represent an average over all the fibers of the suspension. Both orientation functions are equal to 0.5 if the particle orientation is statistically isotropic.

The relevant flow parameters in this research are the Peclet number, Pe, and the particle Reynolds number, Re$= \dot{\gamma}L^2/\nu$, where ν is the fluid kinematic viscosity, $\nu = \mu/\rho$. Due to the small size of the fiber, in most situations the particle Reynolds number is negligible. The Peclet number for rotational Brownian diffusion is defined as

$$\text{Pe} = \frac{\dot{\gamma}}{D_r}, \tag{6}$$

where D_r is the Brownian rotary diffusion coefficient. It has been presented by Brenner [17] as

$$D_r = \frac{k_B T}{6\mu V_p B_r}. \tag{7}$$

Here k_B is the Boltzmann constant ($k_B = 1.38 \times 10^{-23}$ J/K), T is the absolute temperature in degrees Kelvin, V_p is the volume of the suspending particle and B_r is given by

$$B_r = \frac{2}{9}\left[\left(\frac{r_p}{\ln r_p}\right)^2 (\ln 2r_p - 1) + \frac{3B_k}{8\pi}\right], \tag{8}$$

where $B_k = 5.45$ for cylinders with finite length where $r_p \gg 1$. It can be seen that the Peclet number is the ratio of viscous to Brownian forces. When Pe is small, the effects of Brownian motion are dominant, particles tend to orient randomly and the suspension become isotropic. When Pe is large, the effects of the bulk motion and the convection of the fluid become dominant, the effects of Brownian motion are negligible, and particles tend to align with the flow. In the simulations the fiber dimensions are of the order of a millimeter or larger and Pe $\simeq 10^{14}$, and the effects of Brownian motion are negligible.

The rheological properties of fiber suspensions in this study are the relative shear viscosity, η, which is defined as effective shear viscosity μ_{eff} divided by the viscosity

5

of the suspending fluid μ, and the first effective normal stress difference N_1. They are important in describing shear–induced migration of the fibers. The second effective normal stress difference N_2 is also calculated in these simulations. But it is found that the numerical noise is too high compared to the absolute value of N_2; the signal to noise ratio is less than 0.6 in all cases and the value of N_2 is an order of magnitude smaller than N_1. Therefore, no reliable results of N_2 for flexible fiber suspensions could be obtained. Experimentally measuring the effective normal stress differences is difficult, and the deviation between different investigators is quite large.

In this study, rheological properties are directly computed based on the averaged stress tensor in a cubic–box–shaped subdomain. The relative shear viscosity η is given by

$$\eta \equiv \frac{\mu_{eff}}{\mu} = \frac{\sigma_{xy}}{2\mu E_{xy}}, \tag{9}$$

where $E_{xy} = \dot{\gamma}/2$ is the shear strain component of the strain rate tensor, $\boldsymbol{E}$, and σ_{xy} is the shear stress component of the stress tensor $\boldsymbol{\sigma}$. The first effective normal stress difference is given by

$$N_1 \equiv \sigma_{xx} - \sigma_{yy}. \tag{10}$$

Batchelor [10] derived the rheological properties based on the suspension fiber's state, since the position and the orientation of every fiber is known explicitly at every time step. The Batchelor's relation [10] for the contribution of the suspended fibers to the stress in dilute suspensions without Brownian motion is given by

$$\boldsymbol{\sigma}^B = 2\mu\boldsymbol{E} + \mu_{fiber}\left(\langle\boldsymbol{pppp}\rangle - \frac{1}{3}\boldsymbol{I}_n\langle\boldsymbol{pp}\rangle\right) : \boldsymbol{E}, \tag{11}$$

where $\boldsymbol{E}$ is the strain rate tensor, $\boldsymbol{I}_n$ is the unit tensor. $\boldsymbol{p} = p_x\boldsymbol{e_x} + p_y\boldsymbol{e_y} + p_z\boldsymbol{e_z}$ is a unit vector parallel to the fiber axis of symmetry, and $\boldsymbol{e_x}$, $\boldsymbol{e_y}$ and $\boldsymbol{e_z}$ are the unit vector on the flow direction, velocity gradient direction and vorticity axis direction, respectively. μ_{fiber} is a function of fiber concentration, orientation distribution and

fiber aspect ratio. This relation was extended to semi–dilute regime by modifying μ_{fiber} by Koch, Shaqfeh and coworkers [107, 75, 84].

From equation (11), it can be shown that the relative viscosity from Batchelor's relation η^B is

$$\eta^B = \frac{\sigma_{xy}^B}{2\mu E_{xy}} = 1 + \frac{\mu_{fiber}}{\mu} \left\langle p_x{}^2 p_y{}^2 \right\rangle, \tag{12}$$

and the first effective normal stress differences N_1^B is

$$N_1^B = \sigma_{xx}^B - \sigma_{yy}^B = \mu_{fiber}\dot{\gamma} \left(\left\langle p_x{}^3 p_y \right\rangle - \left\langle p_y{}^3 p_x \right\rangle \right). \tag{13}$$

The rheological properties calculated from equations (12) and (13) depend on the accuracy of Batchelor's theory which requires that fibers move freely with no fiber–fiber interactions. In this paper, we investigate suspensions from the dilute to the concentrated regime, and all rheological properties are calculated directly from equation (9) and (10) without such restriction. The measurement is based on the average stress tensor in the bulk of the flexible fiber suspension. Here we list equations from Batchelor's theory because it clearly shows the relation between the fiber orientation distribution and the pure hydrodynamic contribution to the suspension stress. This feature is very helpful in the following discussions for the simulation results.

Both the relative shear viscosity and effective normal stress differences are important in describing the non–Newtonian nature of fiber suspensions. The effective normal stress difference shows the non-symmetric changes in the $p(\phi)$ distribution function. The moments in equation (10) are all zero if the orientation distribution function is symmetric with respect to the xz–plane. These moments are very small and sensitive, and they are difficult to measure by experimental techniques. Bibbo [12] confirmed that the transient normal stress difference was proportional to $\dot{\gamma}$, but the value of the normal force was below the sensitivity of the rheometer.

In this research, we developed a new method [122, 121] for direct numerical analysis of three–dimensional deformable particle suspensions, including fiber suspensions

in the dilute, semi–dilute and concentrated regimes. The flow is computed on a fixed regular 'lattice' using the lattice Boltzmann method (LBM), where each solid particle/flexible fiber is mapped onto a Lagrangian frame moving continuously through the domain. A flexible fiber model has been developed to simulate fibers with high aspect ratio, efficiently. The lattice Boltzmann method for analysis of fluid flow problems [29, 67, 88] has been extended to direct simulation of particles suspended in fluid [78, 4, 5, 2]. In these methods, the no–slip boundary condition at the fluid–solid interface is based on the standard "bounce–back" (SBB) rule. The interaction boundary is represented at the mid–points of the links which are cut by the solid particle boundary as shown in figure 1.2(a). A fluid–solid collision function is used to account for the momentum exchange and to apply the interaction force to both fluid and the particle.

The SBB method has been used for simulation of deformable particles with some success. Buxton *et al*. [24] combine the LBM with the lattice–spring model to study the interaction and deformation of an elastic shell with the surrounding fluid. Dupin *et al*. [41] use a two–dimensional (2D) spring mesh to model elastic membranes. MacMeccan *et al*. [85] use a combination of the LBM for the fluid and finite element method for the solid domain to simulate 800 deformable red blood cells at 45% concentration. All of these studies use the SBB boundary conditions, as this is easy to implement in 3D deformable particle simulations. However, with SBB the solid boundary (Red broken line in figure 1.2(a)) will not move continuously and smoothly in space; instead it will jump from one midpoint to another. If we consider a particle at two different time steps, t_1 and t_2, as shown in figure 1.3, the blue solid line is the physical boundary of the particle, and the red broken line is the computational fluid–solid interaction boundary based on SBB. It is obvious that the two computational boundaries are different at times t_1 and t_2. This causes fluctuation of the

8
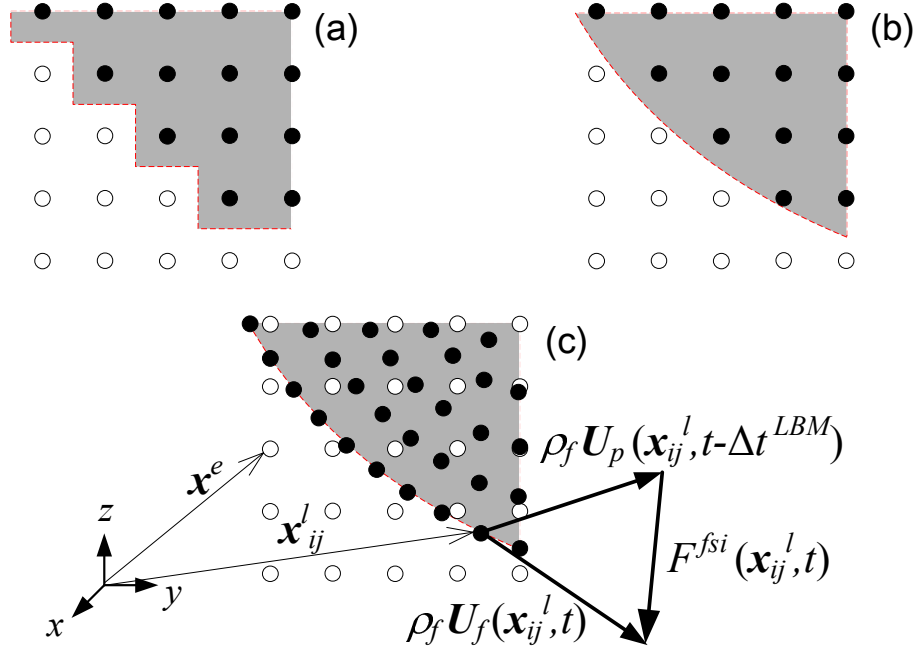
Figure 1.2: (a) Regular Eulerian grid for standard bounce–back (SBB) rule. (b) Regular Eulerian grid for Interpolated bounce–back (IBB) rule. In (a) the filled circles (•) are the fluid nodes covered by the solid, and open circles (∘) are the fluid nodes outside the solid particle. (c) The solid Lagrangian nodes (•) and fluid Eulerian nodes (∘) for external boundary force (EBF) method. The red broken line (⋯) shows the fluid–solid boundary. Note that the solid boundary nodes in the (c) are located exactly on the fluid–solid boundary Γ.

Figure 1.3: Computional fluid–solid boundary of SBB at two different time steps, t_1 and t_2.

fluid–solid interaction force and the particle velocity. It can also cause the simulation to fail at high Reynolds numbers because of the distortion near the fluid–solid boundary. To reduce this fluctuation, one can use a finer lattice grid with more nodes at the boundary which increase the computational time, or one can use a higher order bounce back method based on interpolations. Recently, the bounce–back scheme has been improved by using spatial linear, quadratic, and multi–reflection interpolations [16, 51, 128]. Although the interpolated bounce–back (IBB) methods are more accurate, in addition to being computationally expensive, they require at least two or three fluid nodes between nearby solid surfaces for interpolation. This excludes application to non-dilute suspensions of solid particles with close interaction between the particles or between particles and system boundaries [35, 30].

In this research, A no–slip boundary condition in the LBM for stationary and moving solid particles is implemented. The new method is based on the external boundary force approach developed for the Navier–Stokes equation by Goldstein *et al.* [53]. With the discrete external boundary force (EBF), we consider two overlapping grid systems; a regular Eulerian grid for the fluid domain and a Lagrangian grid for the solid domain. The no–slip boundary condition at the solid surface is applied by adding a force density to the fluid domain to force the difference between the

fluid and solid velocity at the boundary nodes to be zero; the counterforce acting on the solid particles is used to update the position and velocity of the particles based on Newtonian dynamics equations. The lattice Boltzmann equation with the additional boundary force density in the form of a source term is solved to obtain the updated fluid velocity. We show that this approach results in smoother fluid–solid interaction force as compared to standard bounce–back method (SBB), and that it is in general more stable and efficient as compared to the LBM with SBB (with deformable particles). For example, coupling the LBM with the lattice–spring method could cause instabilities when increasing the spring constant or reducing $\Delta x^{LSM}/\Delta x^{LBM}$, the ratio between unit grid size of LSM and LBM [23, 24]. To reduce this instability in LBM with SBB, one has to either increase the size of the particle (the solid grid size) or use a finer fluid grid to increase the number of boundary nodes – both approaches will increase the computational cost. We show that the EBF approach presented here reduces this instability. Also in fiber simulations, to reach a stable and accurate result in existing LBM–SBB methods, the diameter of the fiber, D, must be about 4 to 10 times the unit lattice size, Δx^{LBM} [100, 102]. However in the LBM–EBF method, D is about 0.4 to 1 times Δx^{LBM}. This advantage makes EBF more efficient compared to the SBB method in fiber simulation. For example, to simulate a fiber suspension with aspect ratio $r_p = 20$, in the LBM–SBB method, the fiber length $L = 80$, and in order to eliminate wall effects, the length of the fluid domain has to be at least 5 times the fiber length, that is $400 \times 400 \times 400$. But in the LBM–EBF method, the corresponding fiber length $L = 8$ and the domain size is $40 \times 40 \times 40$.

The presence of an external *body* force in the kinetic–based conservation equations has been discussed in classical kinetic theory [82]. The connection between the source term in the LBE and the resulting *body* force field in the Navier–Stokes equation has also been discussed since the inception of the LBM two decades ago [61, 86, 21, 79,

58]. A method based on an external *boundary* force at the fluid–solid interface of the moving particle [53] to implement the no–slip boundary condition in the LBM for simulation of deformable suspensions with a simple algorithm and no tunable parameters is presented here.

1.2 Objective

The purpose of this research is to develop a particle–level numerical method to study the rheology and microstructure of suspensions, especially with flexible particles. To reach this goal, a method for direct numerical analysis of three–dimensional deformable particles suspended in fluid is developed. Most existing numerical methods for fiber simulations treat the fiber as a rigid rod–like cylinder in Stokes flow. This limits the application of these methods, especially in cases that involve fibers with high aspect ratio or low Young's modulus in high shear rate flow. In this new method, the flow is computed on a fixed regular 'lattice' using the lattice Boltzmann method (LBM), where each solid particle is mapped onto a Lagrangian frame moving continuously through the domain. Instead of the bounce–back method, an external boundary force (EBF) is used to impose the no–slip boundary condition at the fluid–solid interface for stationary or moving boundaries. The external boundary force is added directly to the lattice Boltzmann equation. The motion and orientation of the particles are obtained from Newtonian dynamics equations. Although the EBF method is general, in this application it is used in conjunction with a modified lattice–spring model (LSM) for deformable particles and a flexible fiber model. The methodology is validated by comparison of experimental and theoretical results. The calculations in LBM and LSM are local, it can be easily programmed and runs efficiently on parallel machines.

This research will hope to achieve the following specific aims:

i. To develop and validate the new LBM with external boundary force method for

fluid–solid interaction in flexible particle suspensions.

ii. To determine quantitatively the effects of fiber aspect ratio, volume fraction and fiber stiffness on the rheological properties and microstructure of flexible fiber suspensions.

iii. To demonstrate the flexibility and applicability of the new method by simulating thousands of deformable particles such as red blood cells (RBCs) in blood flow through complex geometries, such as the hinge area of an artificial heart valve.

1.3 Theory and numerical techniques

Theoretical studies of suspensions usually start with modeling the motion of a single particle in a simple flow field using basic hydrodynamic analysis; this is reviewed and discussed in §1.3.1. Next, the effects of fluid–particle and particle–particle interactions on the microstructure of particle suspension are investigated. This part of the study is focused in the dilute regime and is discussed in §1.3.2. In the non–dilute regime, by calculating the orientation distribution of the particles, the contribution of suspending particles to the bulk flow is obtained based on the relation between suspension microstructure and rheological properties. This is discussed in §1.3.3.

1.3.1 Single particle

Almost all theoretical models are based on the theory of Jeffery [69], who derived the governing equations (equation (2)–(5)) and described the motion of a single ellipsoidal particle in a Newtonian fluid. Bretherton [18] expanded Jeffery's solution to any axisymmetric particle and used an effective aspect ratio r_e which is equal to r_p for ellipsoidal particles. The particle rotation period T_p increases with increasing ellipsoid aspect ratio and is given by

$$T_p = 2\pi \left(r_e + 1/r_e \right) / \dot{\gamma}. \tag{14}$$

There have been both theoretical and experimental studies for r_e. For a rigid cylinder of aspect ratio $r_p = L/D$, Burgers [22] used the approximation of $r_e = 0.74 r_p$ for infinitely long cylindrical rods. By measuring the rotation period of a single, rigid, cylindrical fiber, Goldsmith and Mason [52] found that for fibers with r_p between 20 to 115, the ratio of r_e/r_p decreased from 0.7 to 0.53. Cox [32] derived a semi–empirical correlation of $r_e = 1.24 r_p / \sqrt{\ln r_p}$, which agrees well with the experimental results from Mason *et al.*.

In the ideal situation, if Brownian motion is negligible, a rigid cylindrical particle should rotate in a 'tumbling' motion. The orientation and angular velocity depend only on the initial orientation of the particle. This means that the system is reversible, the bulk stress of the suspension should vary periodically and only determined by the initial configuration of the suspension and would never reach a steady state. For a particle whose long dimension is larger than 10μm, the effect of Brownian motion is negligible [80]. But experiments gave a different conclusion. Anczurowski and Mason [7] and Goldsmith and Mason [52] observed that the fiber suspension exhibits a 'fading memory'. The suspending fiber changes its phase angle (ϕ_0 in equation (4)) and orbit constant (C_j in equation (5)) with different time scales. Stover, Koch and Cohen [111] captured the orientations of fibers in a cylindrical Couette device and measured an orbit constant correlation function which shows the rate of memory loss. Zirnsak, Hur and Boger [132] concluded that fiber suspensions quickly forget the initial configuration, possibly due to fiber–fiber interaction, polydispersity of fiber aspect ratio and non–uniform shear rate. Hur [68] summarized all previous studies and proposed that a non–Newtonian suspending fluid and the effect of external forces may also cause 'fading memory'. From the present study, it is found that particle deformability is also an important factor, and flexible fibers forget the initial

14

configuration much faster than rigid fibers that have same aspect ratio. More details and discussion can be found in §3.

1.3.2 Dilute regime

The dilute suspension theories contain the following assumptions:

i. The fiber volume fraction, c_{vf}, is very small, so there is no hydrodynamic interaction between particles, or between particle and wall.

ii. The fiber length is much smaller than any flow dimension, and the fiber aspect ratio r_p is uniform.

iii. The effects of inertia, Brownian motion and external body forces are negligible.

iv. The suspending fluid is uniform, incompressible and Newtonian.

From continuum theory, the rheological properties of dilute suspension should continually oscillate and never reach a steady state. The bulk properties of the suspension depend on fiber volume fraction c_{vf}, aspect ratio r_p and fiber orientation distribution. Many researchers have derived different models; their results are summarized here.

Jeffery [69] quantitatively described the viscosity change due to the suspending particles. It has been shown that the energy dissipation depends on the initial particle orientation. Guth [59] derived a theoretical expression for rigid fibers in dilute suspension. For the case of minimum energy dissipation, with particles oriented in the vorticity direction (z direction as shown in figure 1.1 and $C_j = 0$), the relative shear viscosity was the same as Jeffery's result:

$$\eta = 1 + 2c_{vf}. \tag{15}$$

For the case of maximum energy dissipation, where particles are rotated in the shear plane (xy–plane as shown in figure 1.1 and $C_j = \infty$), it was

$$\eta = 1 + 2c_{vf}\left(1 + \frac{r_p/4}{\ln 2r_p - 1.5}\right). \tag{16}$$

15

Burgers [22] investigated the viscosity for rigid elongated ellipsoids. For suspending particles having random orientation distribution (isotropic), the result obtained was

$$\eta = 1 + 2c_{vf}\frac{r_p/(3\pi)}{\ln 2r_p - 1.8}. \tag{17}$$

For the case of maximum energy dissipation, the viscosity increases and it was given by

$$\eta = 1 + c_{vf}\frac{r_p/3}{\ln 2r_p - 1.8}. \tag{18}$$

Hinch and Leal [63] found that the relative viscosity for the dilute suspension of elongated ellipsoids is a function of the Peclet number Pe. They found that even with weak Brownian mnotion, the suspension will 'forget' the initial configuration and reach a steady state. If Brownian motion is very weak, then

$$\eta = 1 + c_{vf}\frac{0.315r_p}{\ln r_p}. \tag{19}$$

They also found that the first normal stress difference $\sim O(D_r)$ at steady state [64], where D_r is Brownian rotational diffusivity in equation (6) and $D_r \ll 1$. In the following calculation [65], for suspending fibers having aspect ratio of 5, the first normal stress difference was less than 1/3 of the shear stress generated by fibers, the second normal stress difference was negative and the absolute value is one order of magnitude smaller than the first. If the fiber has a very large aspect ratio, $r_p \to \infty$, the first normal stress difference for dilute rigid fiber suspension is given by [63]

$$N_1 = c_{vf}\mu D_r r_p^4/4\ln r_p. \tag{20}$$

A detailed discussion of the motion of rigid, neutrally buoyant, axisymmetric particles in Newtonian fluid was given by Brenner [17]. He found that the dynamics of any rigid, arbitrary axisymmetric particle only depends on five non–dimensional parameters, which are only determined by the shape of the particle. Hinch and Leal [65] obtained similar results, and they named these parameters the 'shape factor'. In

16

their research, they also calculated the value of these non–dimensional parameters for ellipsoids with different aspect ratios. Brenner gave the viscosity of rigid fibers, dilute suspensions for the cases of dominant Brownian motion, intermediate Brownian motion and weak Brownian motion. When the Peclet number is very small, $\text{Pe} \ll 1$, and Brownian motion is dominant, Brenner obtained the same result as Simha [110] and Kuhn and Kuhn [77], the viscosity is given by

$$\eta = 1 + c_{vf} \left[2 - B_2 + 2B_3 - \frac{(B_0 \text{Pe})^2}{1260} (12B_2 + 6B_3 + 35B_n/B_0) \right]. \qquad (21)$$

In the case of intermediate Brownian motion, $1 \ll \text{Pe} \ll r_e$, the viscosity is given by

$$\eta = 1 + c_{vf} \left[2 + \frac{15}{4}(\frac{1}{B_0} - 1)B_2 - \left(0.822B_2 + 5.388(\frac{1}{B_0} - 1)B_3 \right) / \text{Pe}^{1/3} \right]. \qquad (22)$$

And for weak Brownian motion, $r_e \ll \text{Pe}$, the relative viscosity becomes

$$\eta = 1 + c_{vf} \left[2 - \frac{15}{4} \left(B_1(1 - \frac{1.792}{r_e}) - \frac{B_2}{B_0}(1 - \frac{3.0524}{r_e}) - \frac{r_e^2}{B_0 \text{Pe}^2}(3B_2 + 4B_3) \right) \right]. \qquad (23)$$

Here

$$\begin{aligned}
B_0 &= 1 - \frac{3B_k \ln r_p}{4\pi r_p^2}, \\
B_1 &= \tfrac{2}{5} - \frac{6\ln 2 r_p}{5r_p^2}, \\
B_2 &= \frac{2r_p^2}{45 \left(\ln 2 r_p + \ln 2 - (17/6) \right)}, \\
B_3 &= \frac{B_0}{15} \left[\left(\frac{r_p}{\ln r_p} \right)^2 (\ln 2 r_p - 1) - \frac{3B_k}{8\pi} \right], \\
B_n &= \frac{2}{15} \left[\left(\frac{r_p}{\ln r_p} \right)^2 (\ln 2 r_p - 1) - \frac{3B_k}{8\pi} \right],
\end{aligned} \qquad (24)$$

and $B_k = 5.45$ for cylinders having finite length.

Brenner [17] also derived normal stress differences for dilute suspensions of axisymmetric rigid particles. Under the same conditions as Hinch and Leal [63], when Brownian motion is weak and the suspending cylindrical fibers have large aspect ratio,

the first normal stress difference is given by

$$N_1 = \frac{5c_{vf}k_BT}{2V_pB_r}\left[\left(1 - \frac{4.2142}{r_e}\right)\frac{3B_2 + 4B_3}{B_0} - \frac{r_p^2 B_2(1 + B_0)}{8B_0}\right],\tag{25}$$

where V_p is the volume of the suspending particle and B_r is given in equation (8), it is also found that $N_2 \sim -N_1/7$.

Berry and Russel [11] also derived the relative viscosity for dilute suspensions of rigid long rods with Pe $\ll 1$ and $1 \ll r_p$. The equation is

$$\eta = 1 + \eta_{int}c_{vf} + \frac{2}{5}(1 - 0.0142\mathrm{Pe}^2)\eta_{int}^2 c_{vf}^2,\tag{26}$$

where η_{int} is the intrinsic viscosity and is given by

$$\eta_{int} = \frac{8r_p^2}{45\ln 2r_p}(1 - 0.02\mathrm{Pe}^2).\tag{27}$$

1.3.3   Non–dilute suspension

In this regime, fiber–fiber contact exists and fibers are not free to rotate. There are three critical concentrations for non–dilute suspensions of large aspect ratio fibers ($r_p >> 1$). Mason [87] proposed that fibers can not rotate freely when $nL^3 > 6/\pi$, The fiber–fiber interaction can cause the shear viscosity to increase significantly. Doi [37] found that suspending fibers have to be aligned in a common direction when $nL^3 > r_p$, and can not have random orientation distribution. Meyer and Wahren [91] mentioned that for fiber suspensions, when $nL^3 > 432$, every suspending fiber has at least three contact points with other fibers and forms a transient network structure. The average size of the fiber cluster depends on the fiber concentration, aspect ratio and shear rate. This means that fiber suspension in this regime may have shear thinning behavior. In the current research, we are focused on fiber suspensions that have concentrations much smaller than the third critical concentration. From the results that we obtained in the preliminary simulations, we did not observe shear thinning behavior for dilute/non–dilute suspensions that have particle Reynolds number, Re = $\dot{\gamma}L^2/\nu$, from 0.001 to 0.1.

Blakeney [14] measured the viscosity of Nylon fiber suspensions and gave the relation as

$$\eta = 1 + B_4 c_{vf} + B_5 (B_4 c_{vf})^2, \qquad (28)$$

where B_4 is a non–dimensional parameter determined by the length, aspect ratio and orientation of the suspending fiber. Based on Burgers [22] theory,

$$B_4 = \frac{2r_p}{3\pi(\ln 2r_p - 1.8)}. \qquad (29)$$

The second order term in equation (28) accounts for fiber–fiber interaction, it is only considered when the volume concentration is higher than the 'critical concentration' and Blakeney observed $B_5 = 0.73$ for purely hydrodynamic fiber interactions.

Based on experiments, Carter [25] claimed that in semi–dilute rigid fiber suspensions with large fiber aspect ratio, the first normal stress difference N_1 should be proportional to the shear rate $\dot\gamma$ and the suspending fluid's viscosity μ. Equation (30) is derived based on Jeffery's maximum energy dissipation, $C_j = \infty$ [69] and assumes that fiber–fiber collisions are the major reason for non–zero normal stress differences in simple shear flow. The first normal stress difference is given by

$$N_1 = K_c \mu \dot\gamma \frac{c_{vf} r_p^{3/2}}{\ln(2r_p) - 1.8}, \qquad (30)$$

where K_c is a constant and must be determined experimentally. Different researchers applied Carter's model to their normal stress measurements [25, 73, 54, 132, 98, 106, 71]. These experimental data fell within a band for K_c that ranged from 0.04 to 0.32, although no clear relation between K_c with variables such as fiber volume fraction and aspect ratio has been discovered.

Doi and Edwards [38, 39] investigated the effect of Brownian motion for semi–dilute suspensions of rigid rods. They used average bulk suspension properties to model the effect of fiber–fiber interaction. The rotary diffusivity is averaged over all fiber orientations. It was found that in a non–dilute suspension, the rotational

19

diffusivity D_{rDE} is smaller than the diffusivity in the dilute suspension by a factor of $(nL^3)^2$. When Pe < 1, the relative zero–shear viscosity, $\eta_{DE0} = \lim\limits_{\dot{\gamma} \to 0} \eta$, was given by

$$\eta_{DE0} = \frac{nk_BT}{10\mu D_{rDE}}, \tag{31}$$

where

$$D_{rDE} = \beta_{DE}D_{r0}(nL^3)^{-2}, \tag{32}$$

where β_{DE} is a constant and

$$D_{r0} = \frac{k_BT\ln r_p}{3\pi\mu L^3}. \tag{33}$$

The normal stress differences were also given as

$$N_{1\_DE0} = \frac{nk_BT}{30D_{rDE}^2}, \tag{34}$$

$$N_{2\_DE0} = \frac{-nk_BT}{105D_{rDE}^2}. \tag{35}$$

Doi [37] also found that the relative zero–shear viscosity increases with fiber concentration up to $nL^3 = r_p$, and then decreases.

Dinh and Armstrong [36] developed a constitutive equation for semi–dilute fiber suspensions in Newtonian fluids. The effect of the suspending fiber is modeled based on Batchelor's slender body theory [10]. It was found that the transient shear viscosity is a constant at fixed strains and converge to the steady state relative shear viscosity. It was shown that in steady simple shear flow, the suspending fibers align with the flow and the particles have no effect on the bulk flow if the thickness of the fiber is neglected. Bibbo, Dinh and Armstrong [13] predicted the relative shear viscosity for rigid, semi–dilute fiber suspensions. It is given by

$$\eta = \frac{1}{1 - (4c_{vf}/\pi)^{1/2}}, \tag{36}$$

Folgar and Tucker [45] studied the fiber orientation distribution in concentrated suspensions in Newtonian fluid. They used a dispersion term (like a Brownian motion

force) to approximate fiber–fiber interaction in Jeffery's [69] equation of motion. It is found that the interaction is governed by the interaction parameter, C_I, which can be obtained by fitting the model with experimental data. The interaction eliminates the reversibility of fiber orientation distribution in the shear direction, which is described in Dinh and Armstrong's [36] model.

Batchelor [9] presented the landmark paper in the rheology of non–Brownian suspensions. He derived the general equation for the bulk stress in a suspension of force–free particles with any geometry at any concentration in a Newtonian fluid. Batchelor [10] then applied this theory to the long, slender body suspensions and the stress is given in equation (11). For dilute limit, μ_{fiber} is given by Batchelor [10]:

$$\mu_{fiber} = \frac{\pi n L^3 \mu}{6 \ln (2 r_p)} f_\mu (\epsilon),$$ (37)

where $\epsilon = 1/\ln (2 r_p)$. $f_\mu (\epsilon) = 1$ for infinitely long fibers and for the fiber with finite aspect ratio, the correction is given by [10]

$$f_\mu (\epsilon) = \frac{1 + 0.64 \epsilon}{1 - 1.5 \epsilon} + 1.659 \epsilon^2.$$ (38)

In general, it is very difficult to implement this model in non–dilute suspensions, since the motion and orientation of each particle must be obtained explicitly. In dilute suspensions, this information can be calculated based on Jeffery's [69] theory. In non–dilute suspensions, the instantaneous orientation of each particle is in general unknown. However, for a non–dilute suspension under simple shear flow, most of the particles will be aligned in the flow direction. Koch and Shaqfeh and coworkers [107, 75, 84] counted the inter–fiber hydrodynamic interactions in the semi–dilute regime and μ_{fiber} in this regime is given by

$$\mu_{fiber} = \frac{\pi n L^3 \mu}{3 \left[\ln (1/c_{vf}) + \ln (\ln (1/c_{vf})) + B_6 \right]},$$ (39)

where $B_6 = -0.66$ for suspending fibers when randomly oriented and $B_6 = 0.16$ when all particles are aligned in a common direction. Stover, Koch and Cohen [111]

measured the fiber orientation distribution in semi–dilute regime and suggested that the correction function $f_\mu(\epsilon)$ could also be used in equation (39). They found, as did Carter [25], that the first normal stress difference N_1 should be proportional to the shear rate $\dot{\gamma}$. Sundararajakumar and Koch [112] pointed out that hydrodynamic interaction can not cause non–zero normal stress differences because of symmetry of the flow, linearity and reversibility of Stokes flow. The reasons for non–zero normal stress differences could be mechanical contacts between fibers, fiber inertia and a non–Newtonian suspending fluid. In the present study, it is found that fiber deformation can also affect the normal stress differences. More results and discussion can be found in § 3.

Theoretical predictions of relative viscosity in simple shear flow are summarized in table 2.

While constitutive equations and theoretical models can provide the rheological properties in a form that is easy to comprehend, direct numerical simulations are more favorable in some situations, especially for investigating non–dilute or flexible fiber suspensions. Particle level numerical simulations can discover specific questions and variables, and have become more and more popular since the 1990's. Numerous methods have been developed in this area.

Claeys and Brady [31] have done extensive numerical calculations for elongated particles in an unbounded fluid with hydrodynamic interactions using Stokesian dynamics. This method includes long–range fiber–fiber hydrodynamic interactions as well as short–range hydrodynamic interactions (lubrication force). Yamane[127] assumed that the lubrication force is dominant when the particles are close to each other and ignored the long–range hydrodynamic interactions. Sundararajakumar and Koch [112] simulated dilute to semi–concentrated suspensions, and they included both long–range and short–range hydrodynamic forces. It was found that for spherical particles, the lubrication force is not strong enough to prevent solid–body contacts. In the case

Table 2: Summary of the theories for the relative viscosity of rigid particle suspensions

Author	Year	Shape	c_{vf}	Pe	Comment
Jeffery [69]	1922	Ellipsoids	Dilute	∞	$r_p \to \infty$
Guth [59]	1938	Ellipsoids	Dilute	∞	$C_j = 0$ or ∞
Burgers [22]	1938	Rods	Dilute	∞	Isotropic $C_j = \infty$
Simha [110]	1940	Ellipsoids Rods	Dilute	0	$r_p \gg 1$
Kuhn and Kuhn [77]	1945	Ellipsoids	Dilute	0	$r_p \gg 1$
Blakeney [14]	1966	Rods	Dilute Semi–dilute	All	
Batchelor [10]	1971	Ellipsoids Rods	Dilute	All	
Hinch and Leal [63]	1972	Ellipsoids	Dilute	All	$r_p \to \infty$
Brenner [17]	1974	Ellipsoids Rods	Dilute	All	
Doi and Edwards [38, 39]	1978	Rods	Semi–dilute	All	
Bibbo, Dinh and Armstrong [36, 13]	1985	Rods	Semi–dilute	All	
Berry and Russel [11]	1987	Rods	Dilute	Pe $\ll 1$	$r_p \gg 1$
Koch, Shaqfeh and coworkers [107, 75, 111, 84]	1990 to 1996	Ellipsoids Rods	Semi-Dilute	All	

of rigid fibers, it is also not enough to prevent actual physical contact between fibers. They also have shown that the relative viscosity increases with concentration much more rapidly than predicted by purely hydrodynamic interactions. They concluded that, in non–dilute regime, actual physical contact must occur, and mechanical contacts have strong impact on the suspension microstructure and rheology.

In all the above mentioned works, the fiber is considered as a rigid rod–like cylinder in Stokes flow where inertia of fluid and fiber are ignored. These assumptions allow one to develop theories about the fiber suspension without the complication of fiber deformation. But it is well known that the fiber shape has an important effect on suspension microstructure and rheology. Experimental studies [46, 14, 54] have shown that slight fiber curvature would change the period of fiber rotation, the drag on the fiber and the shear viscosity of the suspension. Yamamoto and Matsuoka [126] modeled a flexible fiber as a chain of spring linked spheres. The fiber can stretch, bend and twist by changing the spring length, bending angle and twisting angle, respectively. The constraints for springs are implemented in the equation of motion. The relative viscosities obtained agreed well with experimental results of Forgacs and Mason [46] but the first normal stress difference is much smaller than was found in the experiments. Joung, Phan-Thien and Fan [70] followed a similar idea and used "spring linked spheres" to model long flexible fibers. The relative viscosities for fibers having different flexibility were calculated and compared with experimental results from Bibbo [12]. A curve fitted relation between relative viscosity and non–dimensional flexible fiber stiffness was obtained.

Ross and Klingenberg [103] treated a flexible fiber as a chain of rigid prolate spheroids connected by ball and socket joins. Compared to Yamamoto and Matsuoka's model, there is no need to solve the iterative constraints for connected springs, and the model can extend to high aspect ratio fibers. Schmid, Switzer III and Klingenberg [104] followed this idea and modeled flexible fibers as chains of rigid rods.

Their research focused on fiber flocculation, and they concluded that the flocculation are strongly affected by interparticle forces and fiber deformations. However, they did not consider the hydrodynamic interactions between fibers, nor the two–way coupling between fibers and the suspending fluid. Switzer III and Klingenberg [113] and Lindstrom and Uesaka [83] did similar investigations by using the same "chain of rods" model to simulate a flexible fiber with high aspect ratio under simple shear flow in Newtonian fluid. These researchers demonstrated that fiber concentration, aspect ratio, equilibrium geometry, fiber flexibility and fiber–fiber interactions are important factors in determining the suspension microstructure and rheology. Qi [100] successfully reproduced single flexible fiber motions by using the same flexible fiber, and he solved the fluid flow by using the lattice–Boltzmann method.

1.4 Experimental techniques

Many researchers have studied the experimental stress growth behavior of fiber suspensions. Good summaries and reviews can be found in publications by Ganani and Powell [48], Bibbo [12] and Zirnsak, Hur and Boger [132]. From these experimental works, it can be found that in general, the relative shear viscosity and first normal stress difference increase with increasing fiber volume fraction and aspect ratio. Some experiments [46, 14, 54] have also shown that fiber flexibility has strong impact on suspension rheology. However, discrepancies between these experiments exist. Nawab and Mason [95], Carter [25], Kitano and Kataoka [73] and Goto *et al.* [54, 55] observed shear thinning in their fiber suspension experiments. But Bibbo [12], Bibbo, Dinh and Armstrong [13], Ganani and Powell [49] and Milliken *et al.* [92] did not. Ganani and Powell [48] found that shear thinning appeared to be observed more in suspensions with large aspect fibers and high fiber volume concentration. This can be explained by anisotropic fiber orientation distribution in the flow direction at higher shear rates.

Blakeney [14] used a concentric–cylinder viscometer to measure the bulk shear flow properties of nylon fiber suspension. It was found that relative shear viscosity will increase rapidly beyond the dilute limit. This behavior can be explained by the contribution of fiber–fiber interactions and was confirmed in later experiments by other researchers.

Carter [25], Carter and Goddard [26] investigated the rheological properties of non–dilute glass fibers in a Newtonian polybutene oil. They found the non–zero first normal stress difference fitted well with equation (30), and the magnitude was of the order of a quarter of the shear stress. The phase lag in oscillatory flow was measured in both pure oil and in fiber–oil suspensions. It was found that phase lag did not change and the observed normal stress was caused by the fiber–fiber interactions, due to anisotropy in fiber orientation and shape.

Kitano and Kataoka [73] employed a cone and plate geometry viscometer to measure the relative viscosity and first normal stress difference in semi–concentrated and concentrated suspensions of Vinylon fibers in silicon oil. It was found that both properties are depend on the fiber aspect ratio, volume fraction and shear rate (shear thinning).

Goto *et al*. [54, 55] measured the rheological properties of nylon fiber suspensions and observed a non–zero first normal stress difference for suspending fibers having aspect ratio larger than 100. The log–log plots of N_1 versus $\dot{\gamma}$ were straight lines and could be fitted to the model developed by Carter [25], equation (30). It was found that suspending fibers with higher aspect ratio have smaller slope on the log–log plot. The first normal stress difference increases with increasing fiber aspect ratio, volume concentration and fiber flexibility.

Bibbo [12] used a parallel plate rheometer to measure the rheological properties of semi–concentrated suspensions with Newtonian and non–Newtonian suspending fluids. Bulk flow behaviour was observed in steady shear flow, start–up flow and small

amplitude, oscillated flow. It was found that in Newtonian suspending fluids, the relative viscosity of the suspension is only a function of the fiber volume concentration and is independent of fiber aspect ratio and shear rate (no shear thinning). Bibbo [12] also investigated the wall effects of semi–dilute randomly oriented fiber suspensions in the shear flow between two parallel plates, both theoretically and experimentally. It was found that small gap width (approximately around suspending fiber length) has strong impact on the rheological properties of randomly oriented suspensions.

Ganani and Powell [49] investigated suspensions of glass fibers with mean aspect ratio of 7.63 and 24.3 in Newtonian fluid. The suspensions showed no elastic effects in oscillatory shearing tests, no shear thinning behaviour and for small strains, showed no strain dependence. These conclusions agreed with Dinh and Armstrong's [36] model. They argued that the shear thinning behaviour in many other researchers' experiments did not accurately reflect the real macroscopic rheological behaviour of the suspensions and that artificial errors might have been present.

Milliken *et al.* [92] utilized falling ball rheometry to measure the relative viscosity of fiber suspension. The advantage of this rheometry compared to conventional rheometers is that, it can minimize disturbances to the initial fiber orientation distribution. It was found that randomly oriented fiber suspensions have higher viscosity compared to aligned fiber suspensions with same fiber volume concentration and fiber aspect ratio.

Koch and co-workers [111, 98] used laser Doppler velocimetry (LDV) to measure fiber orientation distribution. The rheological properties are measured by a concentric–cylinder viscometer, and a suspending fluid with high viscosity was used to improve accuracy. The relative viscosity and first normal stress difference agreed well with Bibbo's [12] experiments. The measured microstructure also agreed with their theoretical models [107, 75, 84], which are based on Batchelor's [9, 10] theory.

CHAPTER II

METHODOLOGY

In this chapter, the numerical methods used to simulate and validate the flexible particle suspensions are described. The chapter is divided into two main sections. The numerical methodology employed to simulate the suspensions is presented first, and it is followed by a description of the validations performed.

First, the novel coupling method, the external boundary force method for fluid–solid interaction, is presented in § 2.1. The numerical flow solver is an extension of the LBM developed by Aidun and co–workers [4, 5, 3, 2, 34, 35]; the details of this solver are described in § 2.2. The deformable particle model and flexible fiber model are then presented in § 2.3 and § 2.4, respectively. The chapter ends with validation examples in § 2.5, and the simulation results are in good agreement with theoretical and experimental results.

2.1   *Fluid–solid interaction*

Fluid flow over a solid particle results in normal and shear forces exerted by the fluid on the particle and, conversely, by the particle on the fluid; this is referred to as the fluid–solid interaction force. This forces the fluid adjacent to the solid surface to move with the surface velocity (no–slip). If an external boundary force identical to the fluid–solid interaction force is exerted on the fluid, the fluid will move with the same velocity. In other words, the effect of the particle motion on the fluid motion could be identically replaced by an external boundary force [53]. Let Π_s and Π_f represent the continuum solid and fluid domains, separated by the fluid–solid boundary, Γ. Here the subscripts s and f serve to symbolically distinguish the solid and fluid domains, respectively. The sets of position vectors of the solid and fluid nodes are represented

by Π_s^N and Π_f^M, where the superscripts N and M denote the solid nodes and fluid nodes, respectively. The subsets for solid and fluid boundary nodes are represented by Γ_s and Γ_f, respectively. Note that because with this method, the solid boundary nodes are exactly on the solid boundary, one can consider Γ_s as a subset of Γ. We use $\boldsymbol{x}$ with components (x, y, z) as the position vector in the fixed Cartesian coordinate system. As shown in figure 1.2(c), the position vector for the jth node on ith particle is given by $\boldsymbol{x}_{ij}^l \in \Pi_s^N$, the position vector for the fluid nodes is represented by $\boldsymbol{x}^e \in \Pi_f^M$, where superscripts l and e serve to symbolically distinguish the position vector for solid nodes and fluid nodes, respectively. Let $\boldsymbol{F}^{fsi}(\boldsymbol{x}, t)$ and $\boldsymbol{g}(\boldsymbol{x}, t)$ represent the force per unit volume acting respectively on the solid and the fluid points $\boldsymbol{x}$ on Γ at time, t. Therefore $\boldsymbol{F}^{fsi}(\boldsymbol{x}, t) = -\boldsymbol{g}(\boldsymbol{x}, t)$ for $\boldsymbol{x} \in \Gamma$. However, the force on the fluid boundary node $\boldsymbol{x}^e$ is given by $\boldsymbol{g}(\boldsymbol{x}^e, t)$ which is not equal to $\boldsymbol{F}^{fsi}(\boldsymbol{x}, t)$ when $\boldsymbol{x} \in \Gamma$. The Navier–Stokes and continuity equations with the external boundary force can be written as

$$\left. \begin{array}{l} \rho \left(\dfrac{\partial \boldsymbol{u}}{\partial t} + \boldsymbol{u} \cdot \boldsymbol{\nabla} \boldsymbol{u} \right) = -\boldsymbol{\nabla} p + \mu \nabla^2 \boldsymbol{u} + \boldsymbol{g}(\boldsymbol{x}, t) \\[2mm] \boldsymbol{\nabla} \cdot \boldsymbol{u} = 0 \end{array} \right\}, \tag{40}$$

where $\boldsymbol{x} \in \Pi_f$, and in this equation, $\boldsymbol{g}(\boldsymbol{x}, t) = 0$ when $\boldsymbol{x} \notin \Gamma$. In the discretized formulation, the external boundary force, $\boldsymbol{g}$, is evaluated on the fluid boundary node by interpolation to find $\boldsymbol{g}(\boldsymbol{x}^e, t)$, as shown below (see equation(45)).

In most situations, the boundary nodes will not coincide with the fluid nodes, so the fluid velocity defined by $\boldsymbol{U}_f(\boldsymbol{x}_{ij}^l, t)$ at solid boundary node $\boldsymbol{x}_{ij}^l$ and at time t should be interpolated by

$$\boldsymbol{U}_f(\boldsymbol{x}_{ij}^l, t) = \int_{\Pi_f^M} \boldsymbol{u}(\boldsymbol{x}^e, t) D(\boldsymbol{x}^e - \boldsymbol{x}_{ij}^l) \, \mathrm{d}\boldsymbol{x}^e, \qquad \boldsymbol{x}_{ij}^l \in \Gamma_s, \tag{41}$$

29

where $D(\boldsymbol{x}^e - \boldsymbol{x}^l_{ij})$ is a discrete Dirac delta function in three–dimensional domain [97],

$$D(\boldsymbol{x}) \equiv \begin{cases} \frac{1}{64h^3} \left(1 + cos\left(\frac{\pi x}{2h}\right)\right)\left(1 + cos\left(\frac{\pi y}{2h}\right)\right)\left(1 + cos\left(\frac{\pi z}{2h}\right)\right), & \text{if } |\boldsymbol{x}| \leqslant 2h, \\ \\ 0, & \text{otherwise}, \end{cases}$$

(42)

where $h \equiv \Delta x^{LBM}$ is the unit lattice length in the LBM calculation. For linear velocity distributions, the interpolation (42) can give an exact solution. For smooth velocity distributions (continuous first order derivative), the interpolation has second–order accuracy. However, the velocity profile at the boundary is usually not smooth and subsequently, relation (41) is only first–order accurate at the boundary. Further improvement to achieve higher order accuracy is under investigation.

The initial velocity in the fluid domain and the particle position and velocity are known. The fluid velocity at the particle boundary is equal to the particle velocity due to the no-slip condition, therefore,

$$\boldsymbol{U}_f(\boldsymbol{x}^l_{ij}, t - \Delta t^{LBM}) = \boldsymbol{U}_p(\boldsymbol{x}^l_{ij}, t - \Delta t^{LBM}),$$

(43)

where the LBM time step $\Delta t^{LBM} = 1$, the term $\boldsymbol{U}_p(\boldsymbol{x}^l_{ij}, t - \Delta t^{LBM})$ is the particle velocity at solid boundary node $\boldsymbol{x}^l_{ij}$ at the previous time step. The fluid–solid interaction force $\boldsymbol{F}^{fsi}(\boldsymbol{x}^l_{ij}, t)$ acting on the solid particle boundary node is given by

$$\boldsymbol{F}^{fsi}(\boldsymbol{x}^l_{ij}, t) = \rho_f \left(\boldsymbol{U}_f(\boldsymbol{x}^l_{ij}, t) - \boldsymbol{U}_p(\boldsymbol{x}^l_{ij}, t - \Delta t^{LBM})\right)/\Delta t^{LBM}, \qquad \boldsymbol{x}^l_{ij} \in \Gamma_s, \quad (44)$$

where ρ_f is the density of the fluid. The resulting force acting on the fluid boundary nodes is given by

$$\boldsymbol{g}(\boldsymbol{x}^e, t) = - \int_{\Gamma_s} \boldsymbol{F}^{fsi}(\boldsymbol{x}^l_{ij}, t) D(\boldsymbol{x}^e - \boldsymbol{x}^l_{ij})\, \mathrm{d}\boldsymbol{x}^l_{ij}, \qquad \boldsymbol{x}^e \in \Gamma_f, \quad (45)$$

where $\boldsymbol{g}$ will be used as an external boundary force term in the LB equation as will be discussed in § 2.2.

$\boldsymbol{F}(\boldsymbol{x}_{ij}^l, t)$ is the combination of the fluid–solid interaction force $\boldsymbol{F}^{fsi}(\boldsymbol{x}_{ij}^l, t)$ and the external force $\boldsymbol{F}^{ext}(\boldsymbol{x}_{ij}^l, t)$ which could include the gravitational force, interparticle (electrical or lubrication) forces; therefore,

$$\boldsymbol{F}(\boldsymbol{x}_{ij}^l, t) = \boldsymbol{F}^{fsi}(\boldsymbol{x}_{ij}^l, t) + \boldsymbol{F}^{ext}(\boldsymbol{x}_{ij}^l, t), \qquad \boldsymbol{x}_{ij}^l \in \Gamma_s. \tag{46}$$

So for the ith particle with N boundary nodes, if we assume the center of gravity of the particle is $\boldsymbol{x}_i^{lc}$, then the total force $\boldsymbol{F}_i$ and the torque $\boldsymbol{T}_i$ on this particle are given by

$$\boldsymbol{F}_i(t) = \sum_{j=1}^{N} \boldsymbol{F}(\boldsymbol{x}_{ij}^l, t), \tag{47}$$

and

$$\boldsymbol{T}_i(t) = \sum_{j=1}^{N} (\boldsymbol{x}_{ij}^l - \boldsymbol{x}_i^{lc}) \times \boldsymbol{F}(\boldsymbol{x}_{ij}^l, t), \tag{48}$$

respectively.

The Newtonian dynamics equations for the ith particle are given by

$$\left. \begin{aligned} M_i \frac{\mathrm{d}\boldsymbol{U}_i}{\mathrm{d}t} &= \boldsymbol{F}_i \\ \boldsymbol{I}_i \frac{\mathrm{d}\boldsymbol{\Omega}_i}{\mathrm{d}t} + \boldsymbol{\Omega}_i \times (\boldsymbol{I}_i \cdot \boldsymbol{\Omega}_i) &= \boldsymbol{T}_i \end{aligned} \right\}, \tag{49}$$

where M_i and $\boldsymbol{I}_i$ are the mass and the inertial tensor of the ith particle; and the velocity, $\boldsymbol{U}_i$, and angular velocity, $\boldsymbol{\Omega}_i$, can be computed by numerical solution of equation (49). Note that in equation (49), the term $\mathrm{d}\boldsymbol{\Omega}_i/\mathrm{d}t$ is dependent on $\boldsymbol{\Omega}_i$, so a simple Euler integration may not give accurate results. A fourth–order accurate Runge–Kutta integration procedure is being used in this study.

2.2 Lattice Boltzmann method with external boundary force

The LBM uses a regular Eulerian grid in the fluid domain. The fluid is modeled as a group of fluid particles moving with discrete velocity. The state of the fluid at node $\boldsymbol{x}^e$ at time t is described by the distribution function, $f_k(\boldsymbol{x}^e, t)$, which is calculated by the lattice Boltzmann equation [5, 29, 67, 88]

$$f_k(\boldsymbol{x}^e + \boldsymbol{e}_k, t+1) = f_k(\boldsymbol{x}^e, t) + \frac{1}{\tau}[f_k^{eq}(\boldsymbol{x}^e, t) - f_k(\boldsymbol{x}^e, t)]. \tag{50}$$

Here $f_k^{eq}(\boldsymbol{x}^e, t)$ is the equilibrium distribution function at $(\boldsymbol{x}^e, t)$, τ is the single relaxation time constant and $\boldsymbol{e}_k$ is the discrete velocity vector. The fluid density ρ and the macroscopic fluid velocity $\boldsymbol{u}(\boldsymbol{x}^e, t)$ are obtained from the first two moments, given by

$$\rho(\boldsymbol{x}^e, t) = \sum_k f_k(\boldsymbol{x}^e, t) \quad \text{and} \quad \rho(\boldsymbol{x}^e, t)\boldsymbol{u}(\boldsymbol{x}^e, t) = \sum_k f_k(\boldsymbol{x}^e, t)\boldsymbol{e}_k. \qquad (51)$$

The most common lattice model for the two–dimensional case is the D2Q9 model, which uses nine discrete velocity directions, while the model for three–dimensional case is D3Q19, which uses a cubic lattice with nineteen discrete velocity directions [5] for the fluid particles moving along the horizontal, vertical and diagonal links. The equilibrium distribution function is defined as

$$f_k^{eq} = w_k \rho \left[1 + 3\boldsymbol{e}_k \cdot \boldsymbol{u} + \frac{9}{2}(\boldsymbol{e}_k \cdot \boldsymbol{u})^2 - \frac{3}{2}\boldsymbol{u}^2 \right], \qquad (52)$$

with $w_0 = 4/9$ for fluid particles at rest, $w_{1-4} = 1/9$ for fluid particles moving in non-diagonal directions, and $w_{5-8} = 1/36$ for diagonal directions in two-dimensional D2Q9 model; and $w_0 = 1/3$, $w_{1-6} = 1/18$ (non-diagonal directions), and $w_{7-18} = 1/36$ (diagonal directions) in the three-dimensional D3Q19 model. For the present model, the pseudo speed of sound is $c_s = \sqrt{1/3}$ and the kinematic viscosity is $\nu = (2\tau - 1)/6$. In the longer time scale, the LBM is effectively solving the Navier–Stokes equations [28, 42, 56].

The lattice Boltzmann operators must be modified at the boundary to fit the wall boundary conditions. In this paper, three different wall boundary conditions are applied. These are the periodic, the no–slip wall and the stress–free conditions. Details about these boundary conditions can be found in the earlier publications [5, 35].

To simulate the interactions between the fluid and the solid particles, the LBM with bounce–back must incorporate the boundary conditions imposed on the fluid by the solid particles. In the conventional LBM, fluid and solid domains share one

regular Eulerian grid (figure 1.2(a),(b)). The nodes are scanned at each time step to mark the fluid nodes outside the solid and the fluid nodes inside the solid boundary. The interaction is calculated by the lattice links that connect the inside and outside fluid nodes. This operation is relatively computationally expensive.

The external boundary force method presented here involves two independent but overlapping grid systems. The Eulerian grid represents the fluid domain where each particle is modeled with a Lagrangian grid. The suspended particles move continuously in space while the no–slip boundary condition on the surface of the particle is satisfied by the requirement that the fluid velocity at the solid boundary node equal the solid velocity at that point. We have to emphasize here that the solid boundary in LBM with SBB and the LBM with EBF is different – in SBB it is halfway between fluid and solid nodes, where in EBF, the solid boundary represented by the Lagrangian grid nodes is the actual and precise boundary of the particle moving continuously through the fluid domain, as shown in figure 1.2(c).

The lattice Boltzmann equation should be modified to include the fluid–solid interaction force $\boldsymbol{g}$ from equation (45) by adding an additional term to the collision function. This changes the lattice Boltzmann equation to

$$f_k(\boldsymbol{x}^e + \boldsymbol{e}_k, t+1) = f_k(\boldsymbol{x}^e, t) + \frac{1}{\tau}[f_k^{eq}(\boldsymbol{x}^e, t) - f_k(\boldsymbol{x}^e, t)] + \frac{3}{2}w_k\boldsymbol{g} \cdot \boldsymbol{e}_k. \qquad (53)$$

Although a similar term is also used in the IBM by Feng and Michaelides [44], the method for calculating the fluid–solid interaction force is very different. With the EBF method, $\boldsymbol{g}$ is computed from (45) by the velocity difference between fluid and solid at the boundary nodes; where in IBM, the interaction force is the internal spring force generated by the small deformation of the solid boundary, with high solid stiffness. Also the way to calculate the dynamics of the solid particle is different. We integrate equation (49) to capture the motion of the solid particle, where in IBM, the solid nodes move with the local fluid velocity.

2.3 Extension to Deformable Particles

Various numerical schemes can be applied for computation of the particle deformation. For example, the finite element method has been coupled to the LB equations to simulate suspension of deformable particles [85]. Here, we simulate the particle deformation using the lattice–spring model. This method consists of a set of Hookean lattice–spring links connecting regularly spaced mass nodes. It has been shown that the large scale behavior of the LSM system can be mapped onto continuum elasticity theory [23]. In this method, the elastic links which generate the stretching energy act as Hooke's Law springs. For small deformations, the elastic energy associated with the ith node, E_i, is given by

$$E_i = \frac{k}{2} \sum_{j=1}^{n} (|\boldsymbol{r}_{ij}| - |\boldsymbol{r}_{ij}^{eq}|)^2. \tag{54}$$

Here k is the spring constant, n is the total number of nodes that connect with node i, $|\boldsymbol{r}_{ij}|$ is the length between node i and j, $|\boldsymbol{r}_{ij}^{eq}|$ is the force free equilibrium spring length between i and j. The elastic force $\boldsymbol{F}_{ij}^{s}$ acting on the lattice node i due to node j is calculated from the derivative of the energy function

$$\boldsymbol{F}_{ij}^{s} = -\frac{\partial E_i}{\partial \boldsymbol{r}_{ij}} = -k \left(\frac{|\boldsymbol{r}_{ij}| - |\boldsymbol{r}_{ij}^{eq}|}{|\boldsymbol{r}_{ij}|} \right) \boldsymbol{r}_{ij}. \tag{55}$$

So the total spring force acting on node i is

$$\boldsymbol{F}_{i}^{sT} = \sum_{j=1}^{n} \boldsymbol{F}_{ij}^{s}. \tag{56}$$

This internal solid force is generated by the extension or contraction of the spring links. For small deformations, this simple model is shown to follow the linear elasticity theory with Young's modulus $E_Y = 5k/2\Delta x^{LSM}$, Poisson's ratio $\nu = 1/4$ and the speed of sound $c_s = \Delta x^{LSM}\sqrt{3k/m_i}$ [23]. Here Δx^{LSM} is the unit link length of the lattice spring and m_i is the mass assigned to each node. One can change Poisson's

ratio by introducing the harmonic potential, rotational potential or additional multi-body interaction terms in the energy function and elastic force function of LSM [8, 105].

There are two basic approaches to calculate the deformation of the solid by using LSM as outlined below. One way is to use an explicit scheme where mass is assigned on each node based on the solid density, and the total force acting on the i th node is given by

$$\boldsymbol{F}_i^{tot} = \boldsymbol{F}_i^{sT} + \boldsymbol{F}_i^{fsi} + \boldsymbol{F}_i^{ext}. \tag{57}$$

Here, $\boldsymbol{F}_i^{sT}$ is the spring force, $\boldsymbol{F}_i^{fsi}$ is the fluid–solid interaction force and $\boldsymbol{F}_i^{ext}$ is the external force. Then we integrate Newton's equation of motion, $\boldsymbol{F}_i^{tot} = m_i(\partial^2\boldsymbol{r}_i/\partial t^2)$, with an explicit method to update the acceleration, velocity and the position for every LS node. This method is straight forward and easy to implement, but it has to meet certain stability requirements [6]. The Courant number $C_r = c_s\Delta t/\Delta x^{LSM}$ needs to be smaller than one to reduce the fluctuations in the fluid–solid interaction force, and $\Delta x^{LSM} \geqslant \Delta x^{LBM}$. These conditions impose a severe limitation on the applicability of this method. In three–dimensional calculations, in order to reduce the computation cost, it is usually preferred to have $\Delta x^{LSM} < \Delta x^{LBM}$.

The second approach is to use an implicit scheme where at each time step, the particle will first move without deformation due to $\boldsymbol{F}_i^{fsi} + \boldsymbol{F}_i^{ext}$, then under the same force, the particle will deform. Each lattice–spring node will instantly relax to its equilibrium state, the spring force $\boldsymbol{F}_i^{sT}$ at each solid node is given by $\boldsymbol{F}_i^s = -(\boldsymbol{F}_i^{fsi} + \boldsymbol{F}_i^{ext})$, and based on equation (55), we can write

$$\boldsymbol{r}_i = \frac{1}{n}\left[\frac{\boldsymbol{F}_i^{fsi} + \boldsymbol{F}_i^{ext}}{k} + \sum_{j=1, j\neq i}^n (\frac{|\boldsymbol{r}_{ij}^{eq}|}{|\boldsymbol{r}_{ij}|}\boldsymbol{r}_{ij} + \boldsymbol{r}_j)\right]. \tag{58}$$

The implicit method is more stable than the explicit method, although it may require additional computational time in the deformation calculations. However, considering that the lattice–spring deformation calculations are a small part of the

35

whole simulation, especially in the simulations that have large number of deformable particles with particle–particle interaction, the implicit scheme seems to be a better choice.

The computational algorithm that has been used in the external boundary force LBM–LSM method can be summarized as follows:

i. At $t = t_0$, the initial fluid velocity in the fluid domain and the particle velocity/position are known.

ii. The fluid velocity $\boldsymbol{U}_f$ on the boundary node is obtained by equation (41), the fluid–solid interaction force $\boldsymbol{F}^{fsi}$ from equation (44) is applied on the solid boundary nodes.

iii. The interaction force and the external force are applied to all solid boundary nodes, the total force and torque acting on the particle are calculated according to equation (47) and (48), the particle velocity and position are updated by numerical integration, and the particle deformation is calculated by LSM.

iv. The interaction force also acting back on the fluid lattice nodes is computed by equation (45), and the fluid field is solved by the modified LBM equation (53). The computations loop back to step (ii).

2.4   Flexible fiber model

The flexible fiber is modeled as a chain of N rods and $N + 1$ hinges, as shown in figure 2.1. Each rod has an equilibrium length of l and diameter D. The fiber length is $L = Nl$, and fiber aspect ratio $r_p = L/D$. We use 4 boundary nodes on the circumference of each hinge to calculate the fluid–solid interaction force, as shown in figure 2.2. Rods bend, twist about the hinges and change length due to the forces that are applied on the fiber boundary nodes. This model is used to calculate the
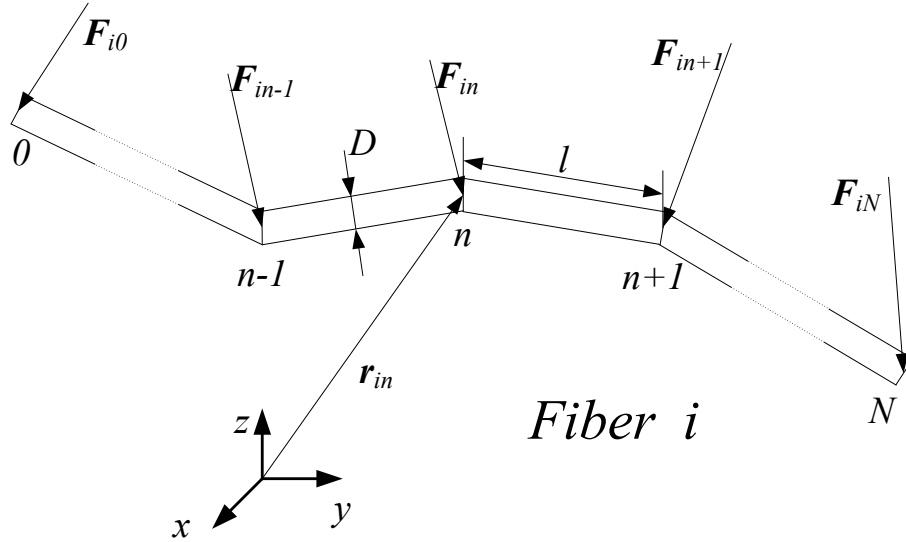
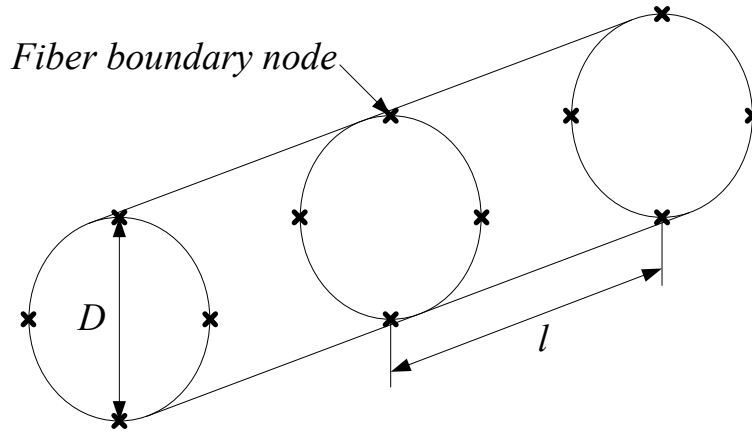**Figure 2.1:** The flexible fiber is modeled as a chain of rods.

Figure 2.2: The boundary nodes on the circumference of each hinge.

fiber deformation by the real material properties such as Young's modulus and shear modulus.

The assumptions are:

i. The suspending fluid is an incompressible Newtonian fluid and the bulk flow is assumed to be homogeneous, $\boldsymbol{U}^{\infty}(y) = \dot{\gamma}y$.

ii. The fiber diameter and length are large enough so that the Brownian motion may be negligible.

The force densities applied on the fiber boundary nodes are the fluid–solid interaction force $\boldsymbol{F}^{fsi}$, the external force which could include the gravitational force $\boldsymbol{F}^{gra}$ and interparticle (electrical $\boldsymbol{F}^{ele}$, contact $\boldsymbol{F}^{con}$ or lubrication $\boldsymbol{F}^{lub}$ forces. The effective volume for each hinge is $dQ \equiv L\pi D^2/(4(N+1))$.

In this simulation, the densities of fluid and fiber are very close, the gravitational force is balanced by the buoyancy force and we only consider the lubrication force. A similar lubrication force used by Yamane $et\ al.$ [127] and Joung $et\ al.$ [70] is also used here with an additional limitation for the case when actual contact of hinges occurs. Let $\boldsymbol{V}_{in}$ and $\boldsymbol{V}_{jm}$ be the velocity of hinge n in fiber i and hinge m in fiber j, respectively (Note, i could be equal to j), $\boldsymbol{r}_{in-jm} \equiv \boldsymbol{r}_{in} - \boldsymbol{r}_{jm}$ is the position vector from hinge m to hinge n, and $|\boldsymbol{r}_{in-jm}|$ is the length of the vector. The relative velocity component $\boldsymbol{V}^{lub}_{in-jm}$ between these hinges is

$$\boldsymbol{V}^{lub}_{in-jm} = \frac{\boldsymbol{r}_{in-jm}}{|\boldsymbol{r}_{in-jm}|}\left[\frac{\boldsymbol{r}_{in-jm}}{|\boldsymbol{r}_{in-jm}|}\cdot(\boldsymbol{V}_{in}-\boldsymbol{V}_{jm})\right]. \tag{59}$$

The lubrication force density between hinges in and jm is given by

$$\boldsymbol{F}^{lub}_{in-jm} = -\frac{9\mu\boldsymbol{V}^{lub}_{in-jm}}{2D\left(|\boldsymbol{r}_{in-jm}| - D\right)}. \tag{60}$$

Then the lubrication force density applied on hinge in is

$$\boldsymbol{F}^{lub}_{in} = \sum_{jm}\boldsymbol{F}^{lub}_{in-jm}. \tag{61}$$

To avoid having fibers cross each other and to remove singularities when overlapping of hinges occurs ($|\boldsymbol{r}_{in-jm}| - D = 0$), the use of equation (60) is restricted in the range of $D + \epsilon \leqslant |\boldsymbol{r}_{in-jm}| \leqslant 1.25D$, where ϵ is a very small positive number to ensure a stable numerical simulation. If the gap is smaller than ϵ, the translation and rotation velocities are reset to make sure the relative velocity component along the direction with minimum distance between the surfaces is equal to zero.

The fluid–solid interaction force $\boldsymbol{F}_{in}^{fsi}$ is given by equation (44), the total force density imposed on hinge in is

$$\boldsymbol{F}_{in} = \boldsymbol{F}_{in}^{fsi} + \boldsymbol{F}_{in}^{lub}, \tag{62}$$

and the total force density applied on fiber i is $\boldsymbol{F}_i = \sum_{n=0}^{N} \boldsymbol{F}_{in}$.

The total force density on each hinge can be split into two parts; $\boldsymbol{F}_{in}^{mov}$ causes acceleration and $\boldsymbol{F}_{in}^{def}$ causes fiber bending, twisting and rotation. From this definition,

$$\boldsymbol{F}_{in}^{mov} = \boldsymbol{F}_i / (N+1) \qquad \text{and} \qquad \boldsymbol{F}_{in}^{def} = \boldsymbol{F}_{in} - \boldsymbol{F}_{in}^{mov}. \tag{63}$$

It is clear that $\sum_n \boldsymbol{F}_{in}^{mov} = \boldsymbol{F}_i$ and $\sum_n \boldsymbol{F}_{in}^{def} = 0$. The change of the length of rod in (the rod between hinge $in-1$ and in), dl_{in} is

$$dl_{in} = \frac{l}{E_Y \left(\pi D^2/4 \right)} \left[\boldsymbol{p}_{in} \cdot \left(\boldsymbol{F}_{in}^{def} - \boldsymbol{F}_{in-1}^{def} \right) \right] dQ. \tag{64}$$

Here E_Y is the Young's modulus of the fiber, $\boldsymbol{p}_{in}$ is the unit vector parallel to the axis of symmetry of rod in and

$$\boldsymbol{p}_{in} = \frac{\boldsymbol{r}_{in} - \boldsymbol{r}_{in-1}}{|\boldsymbol{r}_{in} - \boldsymbol{r}_{in-1}|}. \tag{65}$$

For flexible fiber i, the unit orientation vector is calculated by averaging the p_{in} of all element rods

$$\boldsymbol{p}_i = \frac{1}{N} \sum_{in} \boldsymbol{p}_{in}. \tag{66}$$

Once the forces are known, the moments acting at each hinge can be calculated. For hinge n in fiber i, the moment that causing flexure is

$$\boldsymbol{Y}_{in} = \sum_{m=n+1}^{N} (\boldsymbol{r}_{im} - \boldsymbol{r}_{in}) \times \boldsymbol{F}_{im}^{def} dQ - \sum_{m=0}^{n-1} (\boldsymbol{r}_{im} - \boldsymbol{r}_{in}) \times \boldsymbol{F}_{im}^{def} dQ. \tag{67}$$

This moment can be decomposed into bending and twisting vector components, $\boldsymbol{Y}_{in}^b$ and $\boldsymbol{Y}_{in}^t$ respectively. The twisting moment is given by

$$\boldsymbol{Y}^t_{in} = \boldsymbol{p}_{in}\left(\boldsymbol{p}_{in} \cdot \boldsymbol{Y}_{in}\right), \tag{68}$$

and the bending moment

$$\boldsymbol{Y}^b_{in} = \boldsymbol{Y}_{in} - \boldsymbol{Y}^t_{in}. \tag{69}$$

The bending and twisting angles (β_{in} and α_{in}) can be calculated as

$$\left|\boldsymbol{Y}^b_{in}\right| = -\left(\beta_{in} - \beta^{eq}_{in}\right) E_Y I/l,$$

$$\tag{70}$$

$$\left|\boldsymbol{Y}^t_{in}\right| = -\left(\alpha_{in} - \alpha^{eq}_{in}\right) E_G J/l.$$

Here E_G is the shear modulus of the fiber material, I and J are the appropriate area moments of inertia. For a circular cylinder with diameter D, $I = \pi D^4/64$ and $J = \pi D^4/32$. The angles β^{eq}_{in} and α^{eq}_{in} are specified to mimic different equilibrium fiber shapes. For an intrinsically straight fiber, $\beta^{eq}_{in} = 0$ and $\alpha^{eq}_{in} = 0$.

2.5 Validation

The new numerical method was created with two levels of objectives. First, to validate and confirm the existing results of rigid and flexible fiber suspensions. Second, to improve the accuracy of rheological quantities predicted. The validation of the lattice–Boltzmann method with a discrete external force field will consist of a number of simplified validation cases. Single particle simulations will verify the fluid–solid interaction and the elastic solid model. Many–particles simulations also have been performed to validate the solid–solid interactions and the coupling of hydrodynamics through the lattice–Boltzmann fluid. Several validations, as outlined in table 3, have been simulated and the results are presented in this section.

To improve the computational efficiency and remove wall effects, an unbounded shear–periodic domain is implemented in the LBM code through a Lees–Edwards boundary condition (LEBC) [81] as described by Wagner and Pagonabarraga [117].

Table 3: Validation of LBM–EBF simulation technique

| Simulation	Aera Validated	Particle(s)	Validation
(1) A circular cylinder in shear flow	Fluid–solid interaction	1 rigid cylinder	Experiments: Poe & Acrivos [99], Zettner & Yoda [129] Numeric solutions
(2) A ellipsoid in shear flow	Fluid–solid interaction	1 rigid ellipsoid	Analytic solution: Jeffery[69]
(3) Settling sphere in channel	Fluid–solid interaction	1 rigid sphere	Experiments: Miyamura *et al.* [93]
(4) RBC in capillary flow	Fluid–solid interaction Elastic deformation	1 RBC	Experiments: Tsukada *et al.* [116]
(5) Bulk viscosity of blood	Fluid–solid interaction Elastic deformation	120+ RBCs	Experiments: Fung [47], Merrill *et al.* [90]
(6) Rotation period of a rigid fiber	Fluid–solid interaction	1 rigid fibers	Experiments: Trevelyan & Mason [115], Cox [32]
(7) Deformation of a rigid fiber	Flexible fiber model	1 flexible fibers	Experiments: Forgacs & Mason [46]
(8) Bulk viscosity of rigid fiber suspension	Fluid–solid interaction	1000+ rigid fibers	Experiments: Blakeney [14]
(9) Bulk viscosity of flexible fiber suspension	Fluid–solid interaction Flexible fiber model	1000+ flexible fibers	Experiments: Bibbo [12]
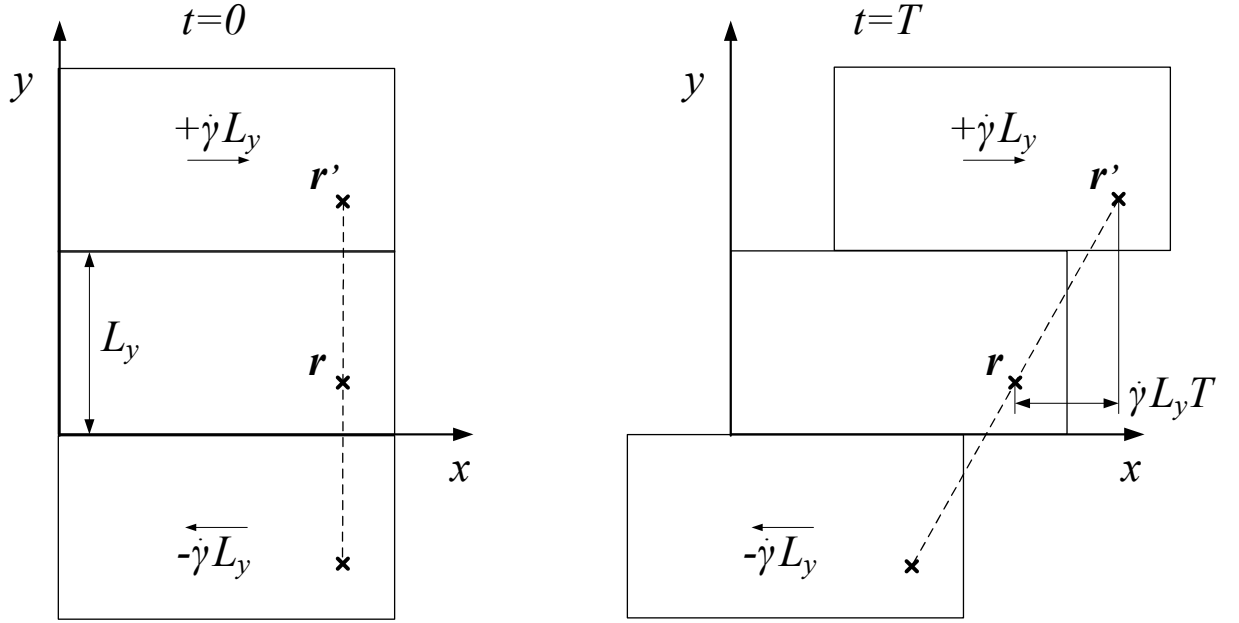
Figure 2.3: Illustrations of unbounded shear domain with Lees–Edwards boundary condition.

Using LEBC, a uniform shear flow has been reached without the moving solid walls, the spatial inhomogeneities that are introduced by the wall effects are eliminated and the bulk rheological properties can be recovered in a smaller fluid domain with fewer particles. The periodic boundary condition is still applied on the flow and vorticity directions (x and z directions, respectively), with the particle image recurring at regular intervals according to L_x and L_z (L_x and L_z are the domain length in x and z directions, respectively). In the shear direction (y direction), the periodic particle images which are offset by L_y will have a corresponding offset of $\dot{\gamma}L_y t$ in the flow direction (x direction), and the velocity of the image in the flow direction is altered by the domain speed, $\dot{\gamma}L_y$, where $\dot{\gamma}$ is the velocity gradient in y direction, as shown in figure 2.3 and equation (71).

$$
r_x' = \begin{cases} (r_x + \dot{\gamma} L_y t) \bmod L_x & r_y > L_y \\ r_x \bmod L_x & 0 \leqslant r_y \leqslant L_y \\ (r_x - \dot{\gamma} L_y t) \bmod L_x & r_y < 0 \end{cases}
$$

$$
r_y' = r_y \bmod L_y
$$

$$
r_z' = r_z \bmod L_z
$$

$$(71)$$

$$
v_x' = \begin{cases} v_x + \dot{\gamma} L_y & r_y > L_y \\ v_x & 0 \leqslant r_y \leqslant L_y \\ v_x - \dot{\gamma} L_y & r_y > L_y \end{cases}
$$

$$
v_y' = v_y
$$

$$
v_z' = v_z
$$

Here $\boldsymbol{r'} = r_x' \boldsymbol{e_x} + r_y' \boldsymbol{e_y} + r_z' \boldsymbol{e_z}$ and $\boldsymbol{v'} = v_x' \boldsymbol{e_x} + v_y' \boldsymbol{e_y} + v_z' \boldsymbol{e_z}$ are the new position vector and velocity of the particle image respectively.

2.5.1 A circular cylinder in simple shear flow

The motion of a neutrally buoyant circular cylinder in simple shear flow has been studied over a wide range of Reynolds number. The cylinder is free to rotate with center axis on the centerline of the fluid field. Due to the wall effect, the non–dimensional rotation speed $\dot{\phi}/\dot{\gamma}$ depends on the Reynolds number, $\mathrm{Re} = \dot{\gamma} a^2 / \nu$, and the flow confinement ratio $\kappa = H/a$, where $\dot{\gamma}$ is the shear rate, a is the diameter of the cylinder and H is the channel height. The LBM method uses a computational domain with 1200×200 lattice nodes. The results are compared at two confinement aspect ratios with the experimental data. The non–dimensional angular rate of rotation with different Reynolds number and confinement ratio are compared with the experimental data by Poe and Acrivos [99] at $H/a = 11.24$ and Zettner and Yoda [129] with $H/a = 4$. The non–dimensional rotation rate will decrease more rapidly with the Reynolds number by using a larger confinement ratio, as shown in figure 2.4.
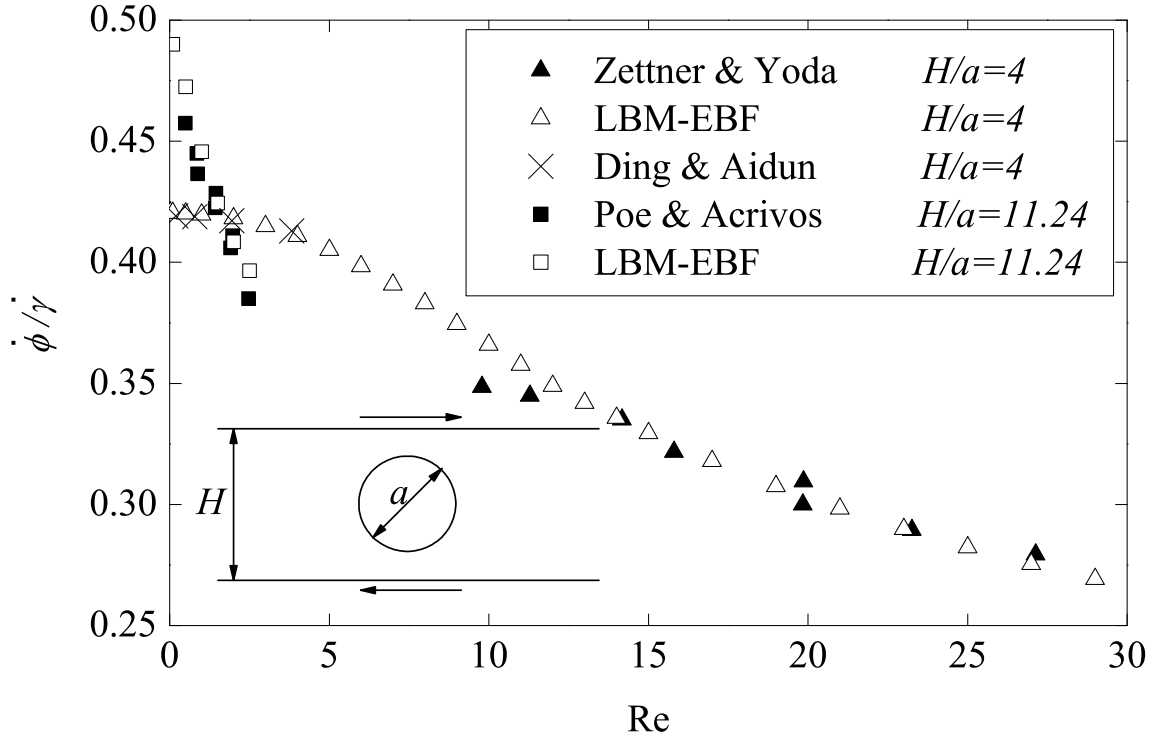
Figure 2.4: Non–dimensional angular rate of rotation of a torque–free cylinder in simple shear flow. The solid squares (■) and triangles (▲) are the experimental data of Poe & Acrivos [99] and Zettner & Yoda [129], the open squares (□) and open triangles (△) are the results from present LBM with EBF, the crosses (×) are results from Ding & Aidun [34] with SBB at Re < 5.
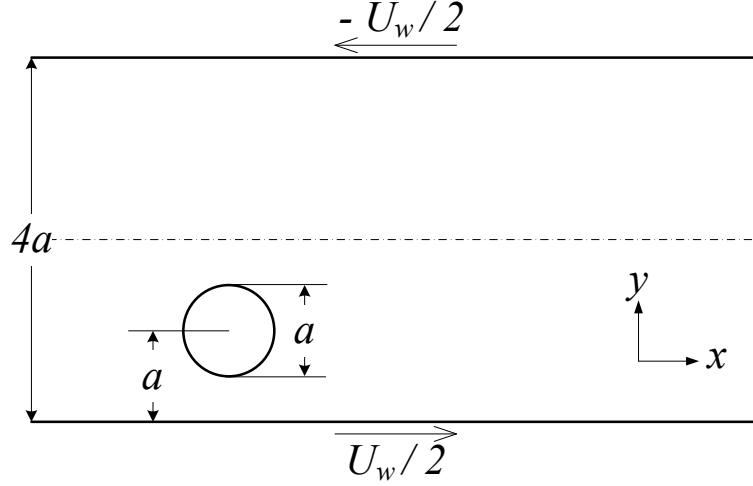
Figure 2.5: A neutrally buoyant cylinder in simple shear flow, off–center initial position.

When $H/a \gg 1$, one can shown from Jeffery's [69] solution (set $a = b$ in equation (74)) that in the limit Re $\rightarrow$ 0, the rate of angular rotation, $\dot{\phi} = \dot{\gamma}/2$. For the case $H/a = 11.4$, the influence of the boundary walls on the circular cylinder is small, therefore $\dot{\phi}/\dot{\gamma}$ approaches ~ 0.5 as Re $\rightarrow$ 0. For the small confinement ratio, $H/a = 4$, however, the effect of the viscous shear stress on the cylinder due to the presence of the boundary walls becomes significant. The cylinder rotates at a lower angular velocity due to the viscous stress. In the limit of Re $\rightarrow$ 0, the rotation rate $\dot{\phi}/\dot{\gamma} \rightarrow 0.42$ for $H/a = 4$, as shown in previous studies [34, 33].

An advantage of the EBF method over SBB is the elimination of small fluctuations which can be detrimental in simulation of deformable particles. To demonstrate, consider a cylinder with diameter a positioned at rest half way from the bottom wall to the center between two parallel plates. The plates are $4a$ apart moving in opposite directions with velocity, $U_w/2$, as shown in figure 2.5. The computational domain has 2000×80 lattice nodes. The trajectory of the particle towards the centerline computed with LBM with SBB and EBF agree well, as shown in figure 2.6. However, the upward velocity, v, shows fluctuation with SBB as compared to no fluctuation with EBF, as shown in figure 2.7. Although the amplitude of the fluctuation in v
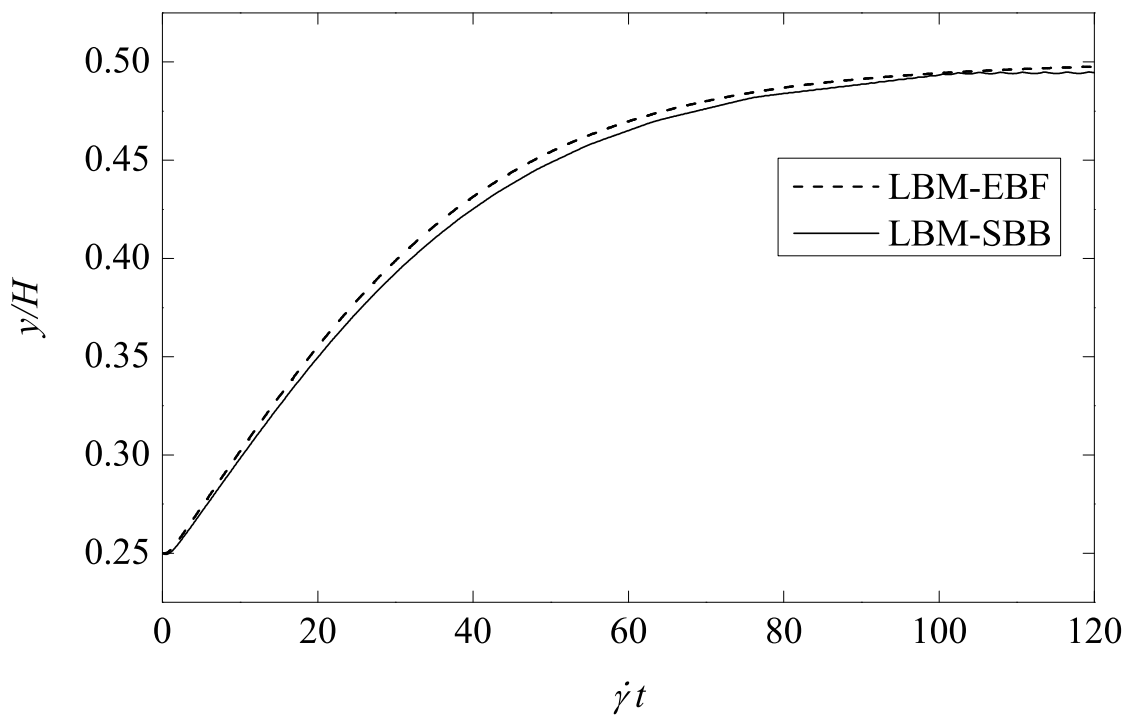
Figure 2.6: Non-dimensional y position *vs.* non-dimensional time $\dot{\gamma}t$. The solid line is from LBM with SBB and the dash line is from LBM with EBF.
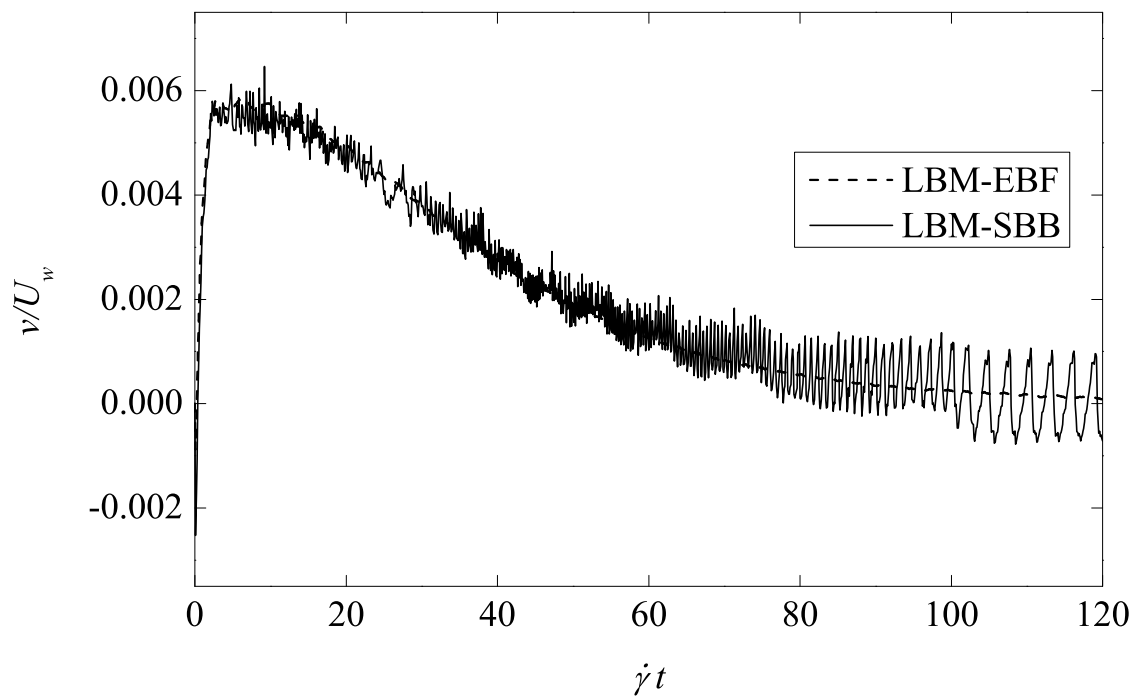
Figure 2.7: Non-dimensional y direction velocity $vs.$ non–dimensional time $\dot{\gamma}t$. The solid line is from LBM with SBB and the dash line is from LBM with EBF.
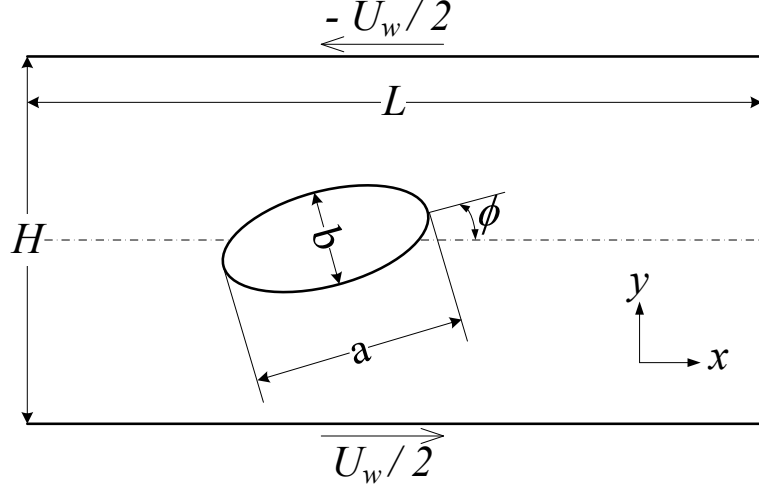
Figure 2.8: A solid ellipsoid immersed in simple shear flow.

is small ($\sim 0.2\%$ of U_w), this may result in numerical instability when it is applied to deformable particles. There is no fluctuation with EBF because the fluid–solid boundary moves continuously across the domain.

2.5.2 An ellipsoid in simple shear flow

The motion of a solid ellipsoid in a simple shear flow is analyzed in this section. The boundary of this particle is given by

$$\frac{x^2}{a^2} + \frac{y^2}{b^2} + \frac{z^2}{c^2} = 1. \tag{72}$$

When one of the principal axes of the ellipsoid is kept parallel to the vorticity vector, as shown in figure 2.8, the rotation angle, ϕ, and the angular rate of rotation, $\dot{\phi}$, are given by [69]

$$\phi = \tan^{-1}\left(\frac{b}{a}\tan\frac{ab\dot{\gamma}t}{a^2+b^2}\right), \tag{73}$$

$$\dot{\phi} = \frac{\dot{\gamma}}{a^2+b^2}\left(b^2\cos^2\phi + a^2\sin^2\phi\right), \tag{74}$$

where $\dot{\gamma}$ is the shear rate and t is time. In our simulation, the computational domain is $120 \times 120 \times 60$ lattice nodes. The Reynolds number $Re = \dot{\gamma}d^2/\nu$, where $d = 2a$. For a different aspect ratio b/a, the computational results agree very well with
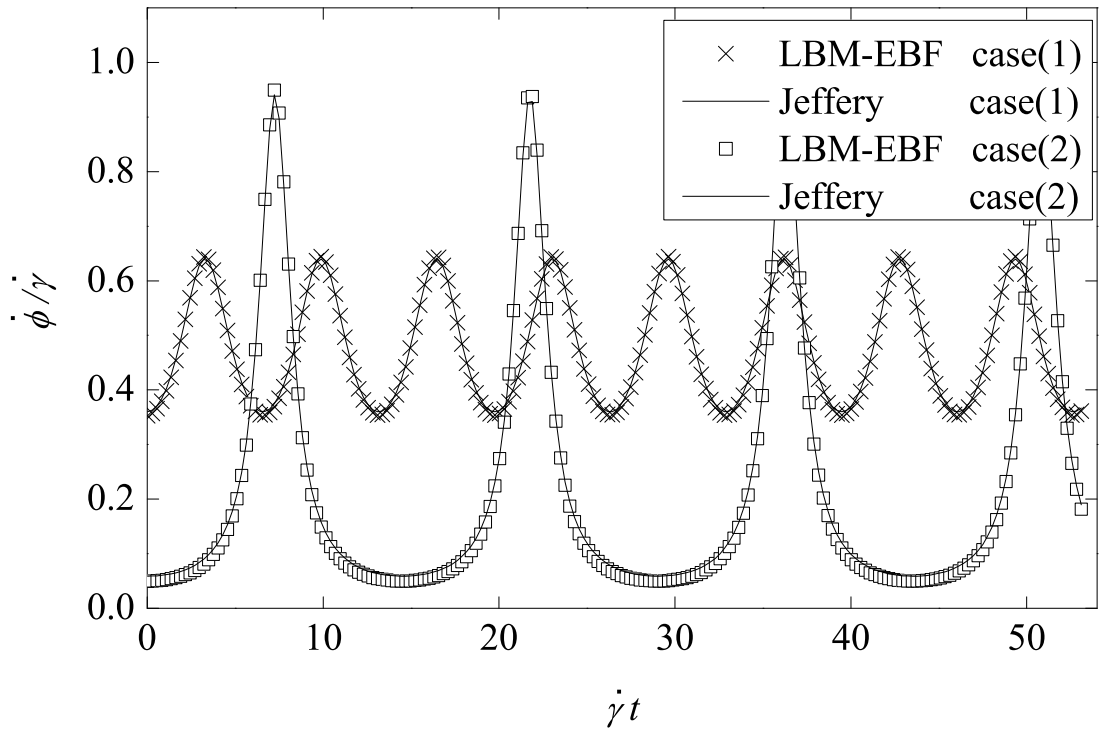
48

Figure 2.9: $\dot{\gamma} = 1/6000$, $a = 12$, $\nu = 1.5$, $Re = 0.064$, Case(1) $b = c = 9$, the solid line is Jeffery's solution and the crosses ($\times$) are the simulation result, Case(2) $b = c = 3$ the dash line is Jeffery's solution and the open squares ($\square$) are the simulation result.

Jeffery's analytical solution, as shown in figure 2.9. This demonstrates that the no–slip boundary condition on the ellipsoid surface is well satisfied.

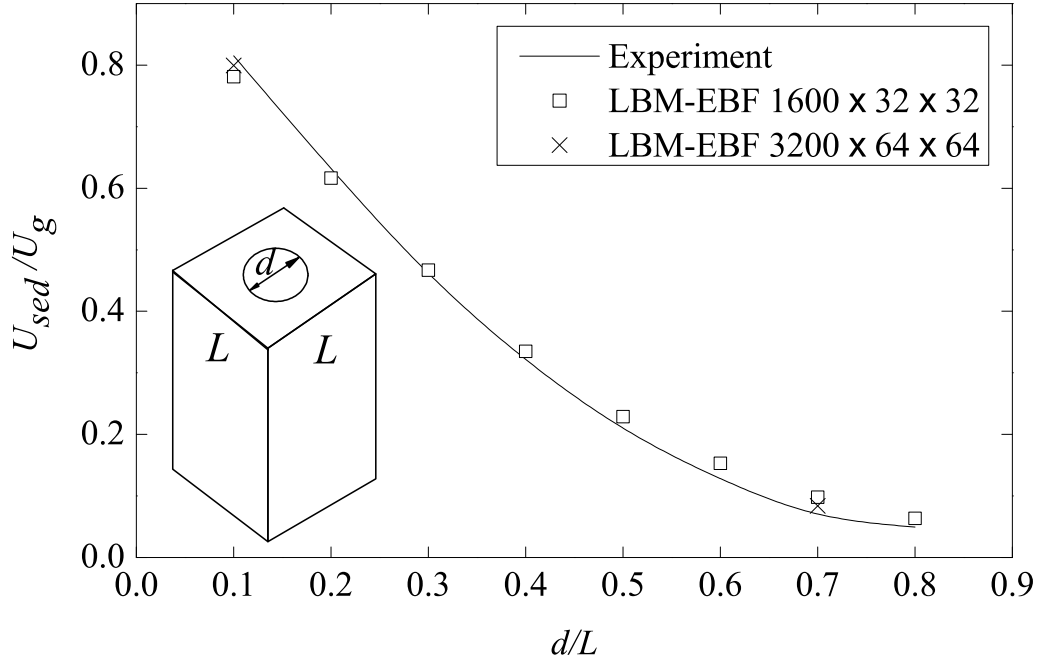### 2.5.3 Sedimentation of a sphere in a square cylinder

Figure 2.10: Sedimentation of a sphere in a square cylinder. The curve is the best fit to the experimental data of Miyamura *et al.* [93]. The open squares (□) and crosses (×) are the results from LBM–EBF with different grid resolution.

A sphere with diameter d is released in a vertical square cylinder of width L settling under gravity force $\boldsymbol{G}_f$, as shown in figure 2.10. The sphere is initially released at the center of the cross–section of the channel with zero velocity, and it settles along the axis of the channel reaching a constant velocity. The steady state settling velocity U_{sed} is normalized with the free settling velocity $U_g = \boldsymbol{G}_f/(3\pi\mu d)$ from Stokes equation.

The simulation results are compared with the experiments of Miyamura *et al.* [93]. In the present analysis, the channel is divided into $1600 \times 32 \times 32$ lattice units. A zero velocity profile is applied at the inlet and the normal derivative of velocity is
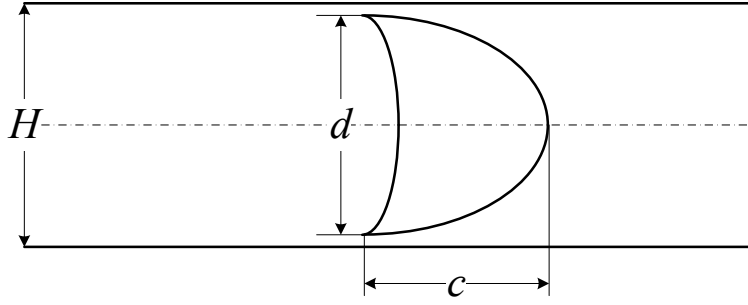
Figure 2.11: Axisymmetrically deformed RBC in a "parachute configuration".

set to zero at the downstream boundary. The curve is the best fit to the experimental data. Results from a finer grid $3200 \times 64 \times 64$, are also included at $d/L = 0.1$ and 0.7 for evaluating the effect of grid resolution. Figure 2.10 shows the comparison between the experimental values and our computational results.

2.5.4 RBC in capillary pressure driven flow

In the next two sub–sections, several problems are presented to demonstrate the effects of the external boundary force method. We combine the lattice Boltzmann method and the lattice–spring model to simulate the deformable particles in suspension. Deformable particles in the shape of red blood cells are used as an example. It is well known that red blood cell (RBC) deformation is one of the most important aspects of blood rheology. Changes in RBC deformation are known to alter blood flow viscosity [72, 108] and diffusivity [27]. The LBM with EBF presented here is capable of simulating suspensions of RBC at the physiological volume fraction of 47%.

In this paper, a capsule with deformable membrane that has the same geometry and the material properties of real RBC is used. RBC has complicated membrane structure with a cytoskeleton and phospholipid membrane encapsulating a fluid solution of haemoglobin. Under normal static conditions, it has a three dimensional biconcave elastic membrane with elastic shear modulus of 6.6×10^3 dynes/cm [118]. The plasma surrounding the RBC has a viscosity of 1.2 cP at 37°C. The RBC has a major diameter of $7.8\,\mu$m and thickness of $2.2\,\mu$m at the flank and $0.9\,\mu$m at the

dimple. These values are used in the following simulation.

It is well known from past experiments that a RBC's shape changes into a parachute shape in capillary pressure driven flow, as shown in figure 2.11. The RBCs retain their shape through the capillary tube, and then recover their original shape in the post capillary region. This unique deformation of the RBC is necessary in nature for high fluidity in micro vessels and for high efficiency of oxygen diffusion to tissue, as it increases the surface area and interaction with the endothelial cells.

Several investigators have used this phenomenon to measure the RBC's deformability. In the recent experimental setup of Tsukada et $al.$ [116], they use a set of transparent crystal micro channels and a high speed video camera to capture high–resolution pictures and obtain quantitative data. Dilute suspensions of RBCs passing through a glass capillary tube with diameter of $9.3\,\mu$m were imaged and analyzed. The velocity and the deformation index DI_P of RBC are dependent on the pressure gradient in the channel. In this experiment [116], DI_P is given by

$$DI_P = \frac{c}{d}. \tag{75}$$

Here d is the diameter of the deformed RBC in the parachute configuration, and c is the length of the RBC along the axial direction as shown in figure 2.11. The simulation results are compared with the experimental results [116]. The Capillary number Ca_P in figure 2.12 is defined as

$$Ca_P = \frac{\mu U_x}{E_S}, \tag{76}$$

where μ is the viscosity of the suspending fluid, U_x is the RBC velocity and E_S is the membrane shear modulus.

The RBC deformation index DI_P is shown in figure 2.12 as a function of Capillary number Ca_P. The simulations agree well with experiments up to $Ca_P \approx 0.35$ where we see a deviation between the results.
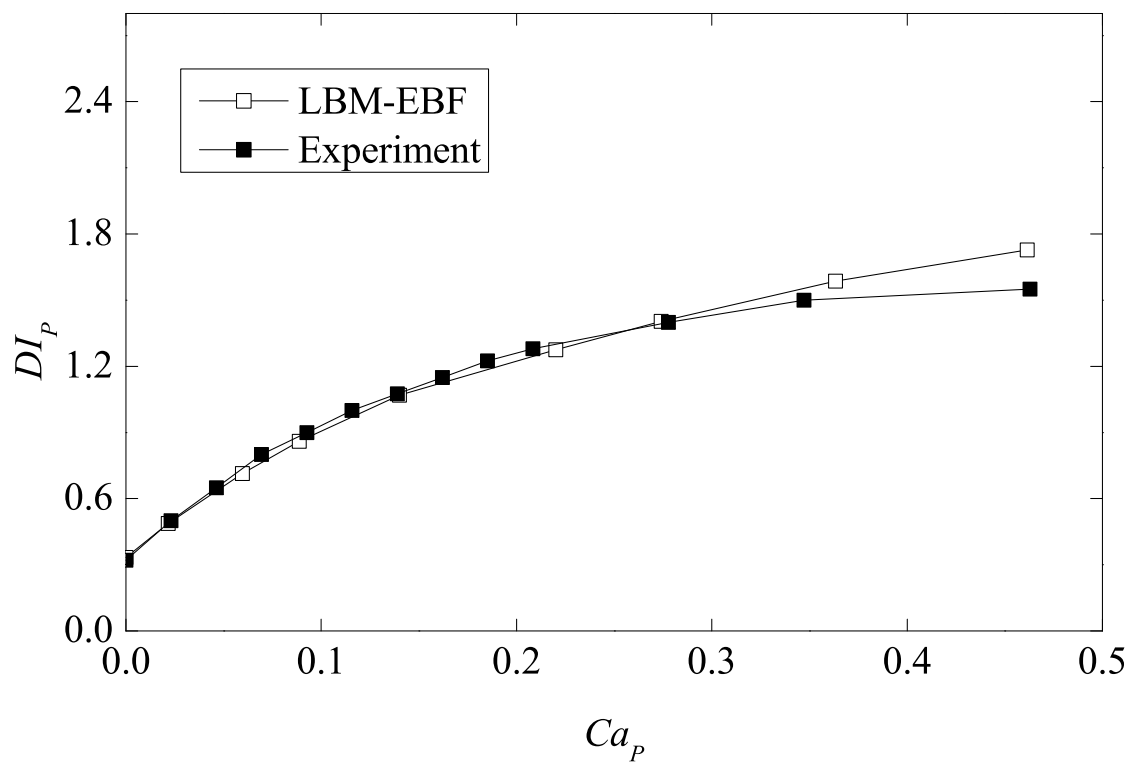
Figure 2.12: Deformation index DI_P *vs.* the Capillary number Ca_P, the solid squares (■) are the experiment data from Tsukada *et al.* [116] and the open squares (□) are LBM–EBF simulation results.

2.5.5 Bulk viscosity of blood

The non–Newtonian shear–thinning viscosity of blood is well documented [19, 90] with RBC deformation recognized as one of the most important factors in suspension viscosity [72, 108].

At high volume fraction, blood is often described by Casson's model, given by

$$\sqrt{\tau_{eff}} = \sqrt{\tau_{yield}} + C_{blood}\sqrt{\dot{\gamma}}, \tag{77}$$

where τ_{eff} is the effective suspension shear stress, τ_{yield} is the yield stress of the suspension in shear, C_{blood} is a constant and $\dot{\gamma}$ is the shear rate. The reduced viscosity of blood is defined as

$$\mu_r = \frac{\mu_{eff}}{\mu}, \tag{78}$$

where $\mu_{eff} = \tau_{eff}/\dot{\gamma}$ is the effective suspension viscosity, μ is the viscosity of the suspending fluid. A Casson fluid exhibits non–Newtonian and shear–thinning behavior. The reduced viscosity μ_r is a function of shear Capillary number Ca_S which is defined as

$$Ca_S = \frac{\mu\dot{\gamma}R}{E_S}, \tag{79}$$

where $\dot{\gamma}$ is the shear rate and R is the average undeformed RBC cross–section radius when viewed from the side. Here the shear rate $\dot{\gamma} = U_w/H$, where U_w is the velocity difference between the top and bottom walls, and H is the channel height.

The reduced viscosity can be successfully simulated with $O(10^2)$ particles [85, 109]. To study blood rheology at continuum–level scales, 120 RBCs are simulated at 47% volume fraction with $0.0149 < Ca_S < 0.1342$, corresponding to shear rate ranging between 16 s^{-1} to 144 s^{-1}, respectively. The plasma has viscosity of 1.58 cP with density of 1030 kg/m^3 at 25°C [60, 118]. Simulations of 80, 120, and 160 RBCs produce the same result in bulk viscosity. The cases with $Ca_S < 0.01$ are not compared here due to the influence of non-hydrodynamic particle interactions that lead to RBC aggregates known as rouleaux [47]. It is shown in figure 2.13 that the
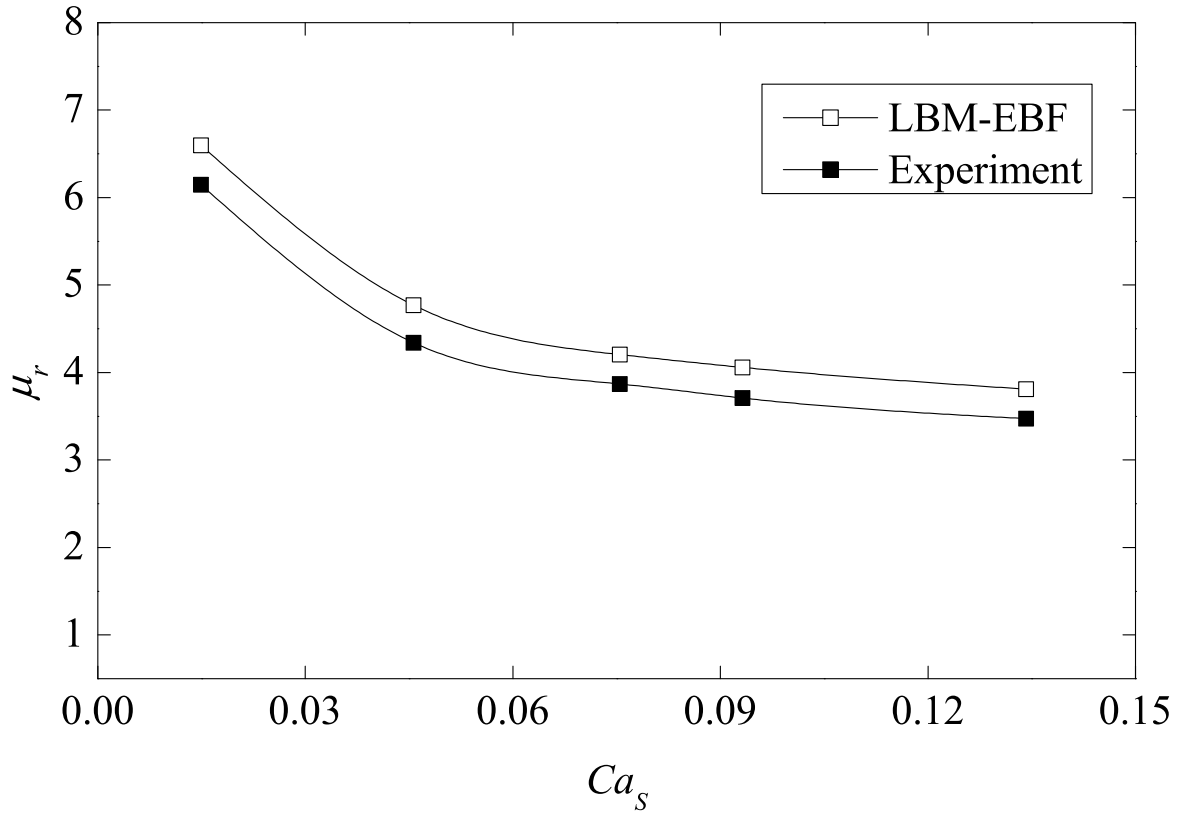
Figure 2.13: The open squares (□) are reduced suspension viscosity of simulations of 120 RBCs at 47% volume fraction as a function of Ca_S. The solid squares (■) are the experimental data reported by Brooks *et al.* [19] at 25°C with 47.6% volume fraction

55

simulation results have a profile similar to that of the experimental data reported by Brooks *et al.* [19].

2.5.6 Single rigid fiber

In the next four sections, we provide some example problems to validate the LBM–EBF method for fiber simulation. In this subsection § 2.5.6, we examine the accuracy of computing the shear stress on the surface of a rotating cylinder at different aspect ratios r_p. In § 2.5.7, we simulate the flexible fiber with different stiffness in simple shear flow where the orbits of bent fibers are compared with experimental data from Forgacs and Mason [46]. Comparison of computational results for rigid fiber suspensions with experiments is presented in § 2.5.8. Computational simulations of flexible fiber suspensions and the effect of fiber stiffness on relative viscosity are discussed in § 2.5.9.

To improve the computational efficiency and remove wall effects, an unbounded shear domain is implemented based on the Lees–Edwards boundary condition (LEBC) [81]. The uniform shear flow has been reached without the moving solid walls, the spatial inhomogeneities that are introduced by the wall effects are eliminated and the bulk rheological properties can be recovered using smaller fluid domain with fewer particles. Periodic boundary conditions are applied in the flow and vorticity directions (x and z directions in figure 1.1, respectively).

Bretherton [18] expanded Jeffery's solution [69] to any axisymmetric particle and used an effective aspect ratio r_e equal to r_p for an ellipsoidal particle. For a single ellipsoidal particle in Stokes shear flow, the governing equations are equations (2) and (3). Integrating these two equations yields equations (4) and (5).

The particle rotation period T_p increases with increasing ellipsoid aspect ratio, $\dot{\gamma} T_p = 2\pi \left(r_e + 1/r_e \right)$. For a rigid cylinder of aspect ratio $r_p = L/D$, the equivalent aspect ratio has been measured by Trevelyan and Mason [115]. The computational results presented in figure 2.14 show agreement with Cox's solution [32],
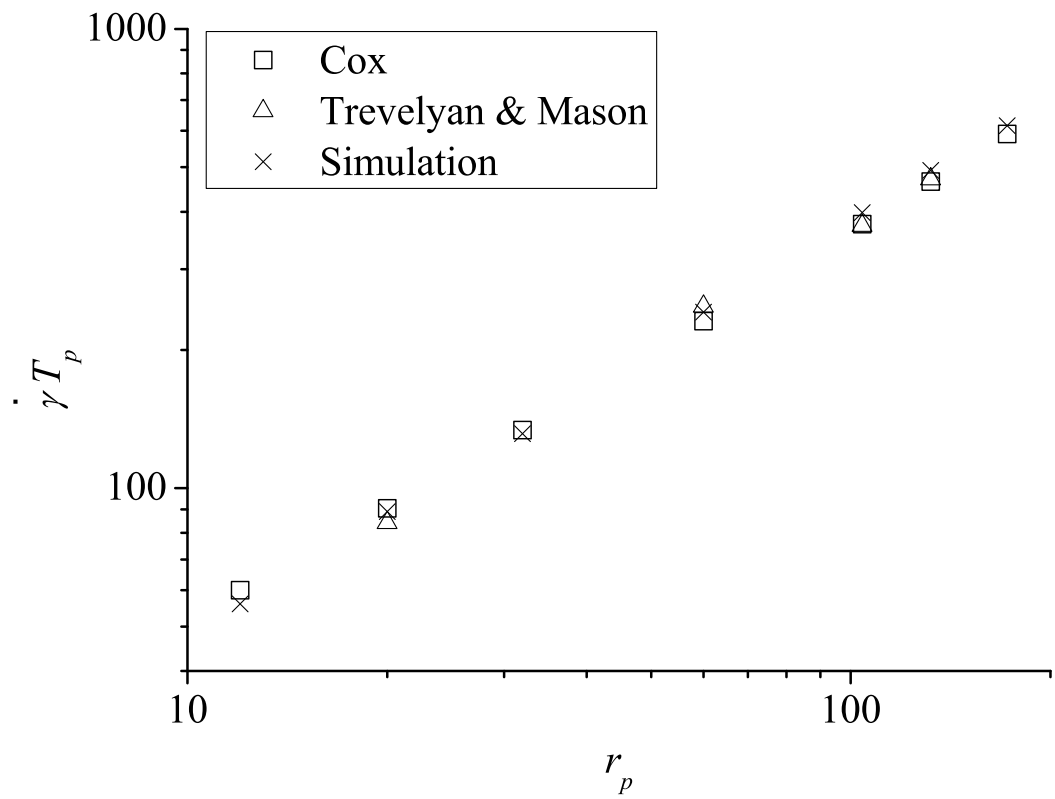
56

Figure 2.14: Non–dimensional rotation period $\dot\gamma T_p$ *vs.* fiber aspect ratio r_p in a x, y simple shear flow.
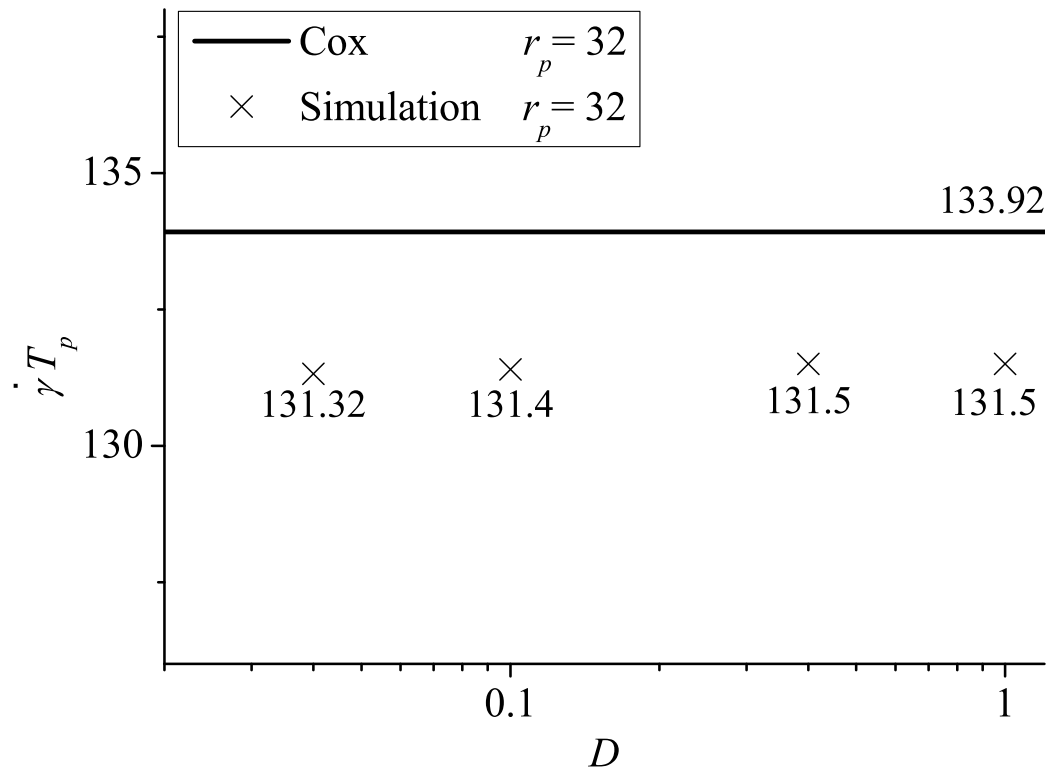
Figure 2.15: Non–dimensional rotation period $\dot{\gamma}T_p$ *vs.* fiber diameter D.

$r_e = 1.24 r_p / \sqrt{\ln r_p}$, and with the experimental data of Trevelyan and Mason [115]. In our simulation, the computational domain is $100 \times 100 \times 10$ lattice nodes, and the suspending fibers have diameter of $D = 0.2$ LBM unit lattice size. This demonstrates that the no–slip boundary condition on the ellipsoid surface is satisfied.

To show the accuracy of the interpolation in the EBF method, especially for fibers that have sub–grid diameters, several simulations were performed for fibers with diameter $D = 1$, 0.4, 0.1 and 0.04 lattice units with fixed aspect ratio, $r_p = 32$. In these simulations, only the size of the LBM lattice unit is changed, while all other parameters remain the same. For example, the size of the LBM lattice unit for $D = 0.1$ is ten times larger than is the case for $D = 1$. As shown in figure 2.15, results show very small deviation between each other and show good agreement with Cox's model with less than 2% difference.

2.5.7   Single flexible fiber

To quantitatively measure the bending deformation of a single flexible fiber, Forgacs and Mason [46] took photographs at short time intervals during the rotation of a long Nylon filament ($r_p = 170$). The result presented in figure 2.16 clearly shows the increase in deformation with shear rate, $\dot{\gamma}$. It also shows the asymmetry of the loci about the y axis due to the compression and the extension forces. To reproduce the existing experimental results, the fiber and the suspending fluid have the same physical properties as Forgacs and Mason used in the experiment; the suspending fibers have diameter of $D = 0.0122$mm, aspect ratio $r_p = 170$ and Young's modulus $E_Y = 6.3$ GPa. The dynamic viscosity of the suspending fluid is $\mu = 9.12$Pa·s. In our simulation, the computational domain is $100 \times 100 \times 10$ lattice nodes and the suspending fibers have diameter of $D = 0.2$ LBM unit lattice size. The simulation result is in fairly good agreement with the experimental result in figure 2.16.
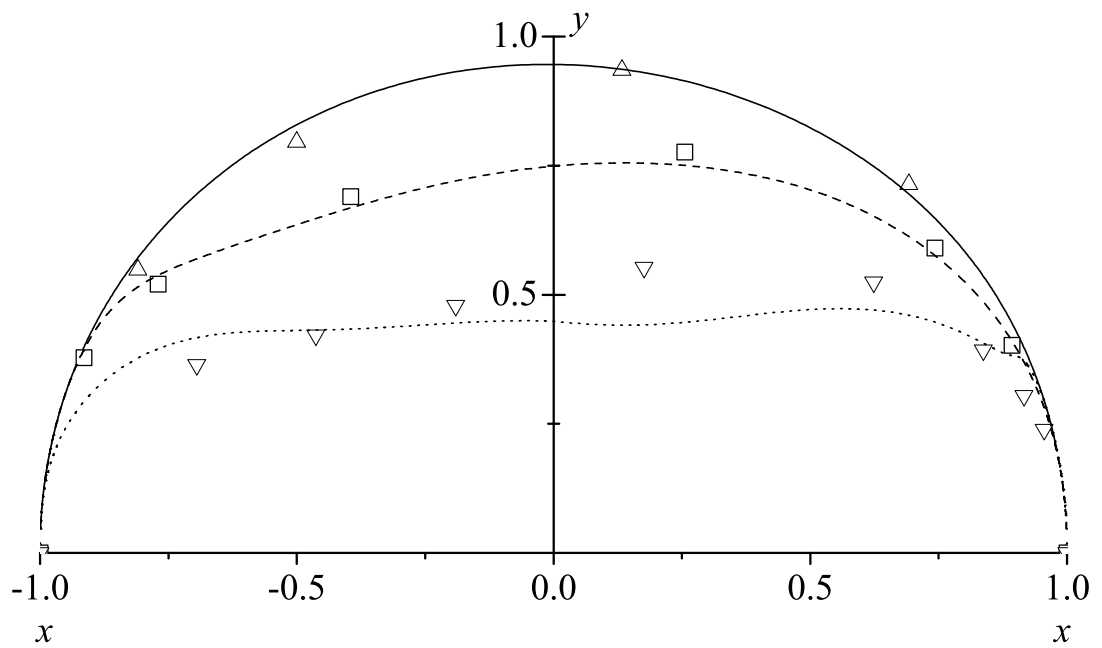
Figure 2.16: Polar plot of the loci of the end of a Nylon filament ($r_p = 170$) during rotation in a x, y simple shear flow. The open triangles ($\triangle$), open squares ($\square$) and open upside–down triangles ($\triangledown$) are the experiment data of Forgacs and Mason [46] for shear rate $\dot{\gamma} = 3.20, 3.54$ and 4.25sec.^{-1}. The solid line (—), dash line (- - -) and dot line ($\cdots$) are the corresponding simulation results
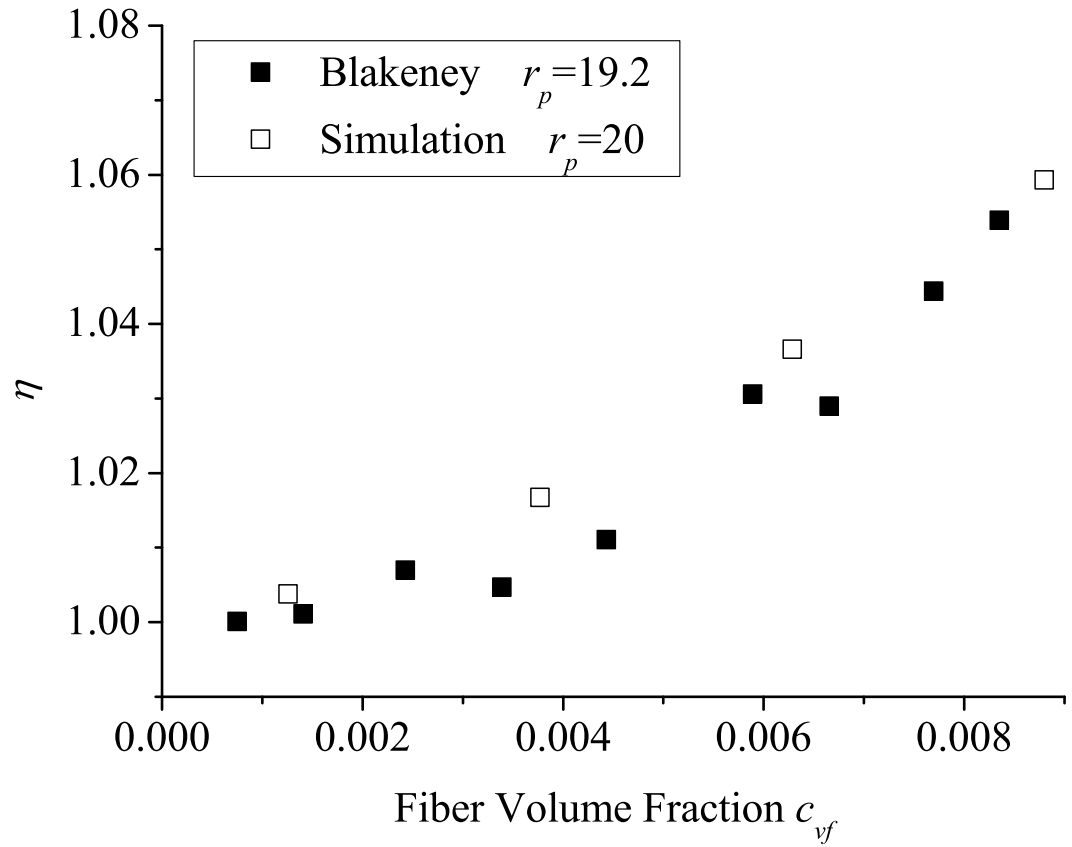
Figure 2.17: The relative shear viscosity η *vs.* fiber volume fraction c_{vf} in dilute regime. The solid squares (■) are the experiment data of Blakeney [14], the open squares (□) are the results from present LBM with EBF.

2.5.8 Rigid fiber suspensions

One of the main objectives of our work is to obtain a better understanding of the rheological behavior of flexible fiber suspensions. Experimental results are often presented in terms of relative shear viscosity, defined in equation (9)

Blakeney [14] used a Couette device to measure the viscosity of rigid fiber suspensions in a Newtonian fluid. We compare the relative shear viscosity computed from our simulations with his experimental results. In our simulation, the computational domain is $80 \times 80 \times 80$ lattice nodes and the suspending fibers have diameter of $D = 0.8$ LBM unit lattice size. The length and aspect ratio of a fiber is $L = 16$ LBM unit lattice size and $r_p = 20$ respectively. As shown in figure 2.17, the trend of the computational results follows experimental data well. The simulations seem to have small overprediction.

2.5.9 Flexible fiber suspensions

Fiber stiffness plays an important role in fiber suspension microstructure and rheology. Forgacs and Mason [46] and Goldsmith and Mason [52] have studied the flow induced deformation of a single flexible fiber in simple shear flow. A cylindrical flexible fiber is predicted to bend when the non–dimensional parameter bending ratio, given by equation (1), is small. There have been experiments to measure the viscosity of flexible fiber suspensions [12]. In Bibbo's experiment, the nylon fiber has density of $\rho_f = 1.25 \times 10^3 \text{kg/m}^3$, diameter of $D = 0.12$mm and Young's modulus $E_Y = 3.0$ GPa. The suspending fluid has density $\rho = 0.97 \times 10^3 \text{kg/m}^3$ and dynamic viscosity $\mu = 13$Pa·s. The flexible fiber suspensions are simulated with volume fraction $1.7\% \leqslant c_{vf} \leqslant 12.4\%$, corresponding to the number of fibers between 180 to 1260. The bending ratio corresponding to aspect ratios $r_p = 16$, 32 and 52 are $BR = 2942$, 248 and 42 respectively. In these simulations, the computational domain is $80 \times 120 \times 80$ lattice nodes and the suspending fibers have diameter of $D = 0.4$ LBM unit lattice size. As
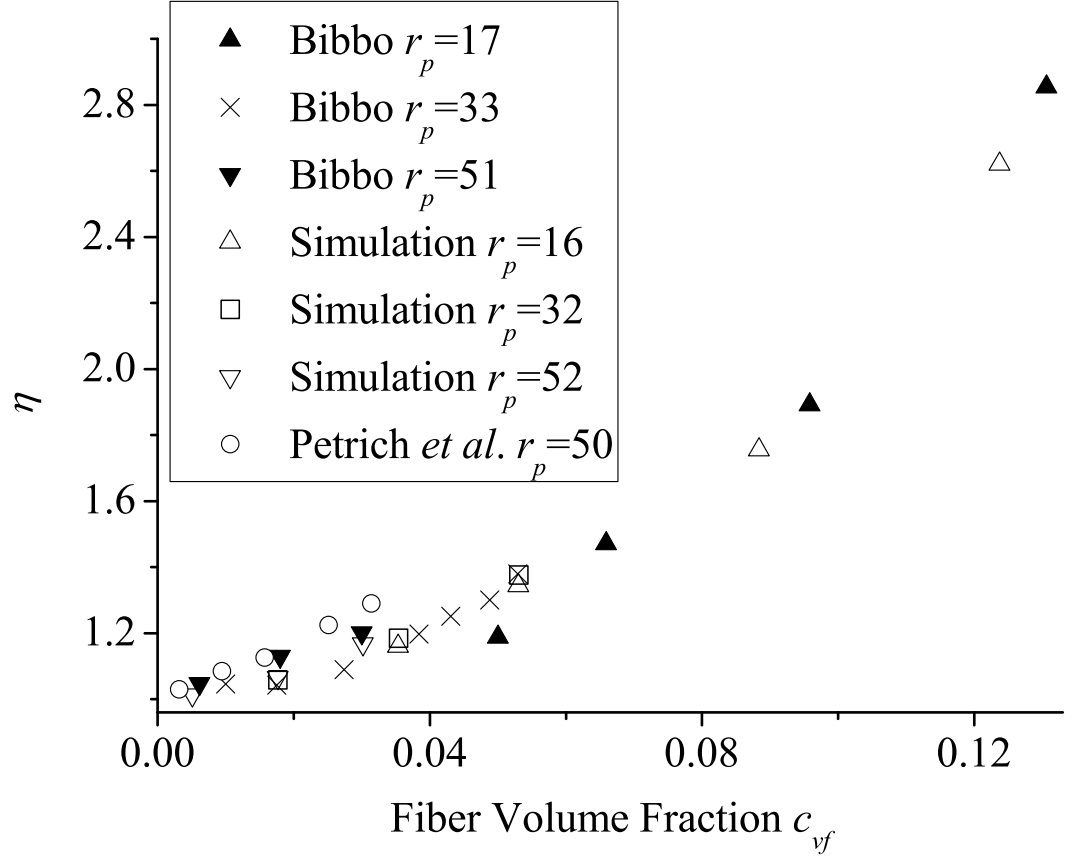
Figure 2.18: The relative shear viscosity η *vs.* fiber volume fraction c_{vf} for fibers with different aspect ratio. The solid triangles (▲), crosses (×) and solid upside–down triangles (▼) are the experiment data of Bibbo [12] ($r_p = 17, 33, 51$). The open circles (○) are the experiment data of Petrich *et al.* [98] ($r_p = 50$). The open triangles (△), open squares (□) and open upside–down triangles (▽) are the results from present LBM with EBF ($r_p = 16, 32, 52$).

shown in figure 2.18, the simulation results compare well with experimental results in the range of fiber aspect ratio and volume fraction covered by the experiments. The effect of aspect ratio at a given volume fraction on η seems to be relatively small.

CHAPTER III

RESULTS AND DISCUSSION

The validation of the lattice Boltzmann approach with the EBF method for fiber suspension is presented in the previous section §2.5 and in publications [122, 121]. Previous studies show that adding fibers to Newtonian fluids will increase both the relative viscosity and the first normal stress difference of the suspensions [95, 73, 45, 49, 107, 98, 106]. The focus of the present study is to investigate the effect of fiber stiffness on the microstructure and rheology of flexible fiber suspensions. Fibers with different stiffness, aspect ratio and volume concentration are being considered in this study, including the effect of fiber–fiber interactions.

An unbounded shear domain is implemented based on the Lees–Edwards boundary condition (LEBC) [81]; This was described by Wagner and Pagonabarraga [117] and Macmeccan *et al.* [85]. It is intended to improve computational efficiency and to remove wall effects. In these simulations, the suspending fluid has density $\rho = 0.97 \times 10^3 \text{kg/m}^3$ and dynamic viscosity $\mu = 13\text{Pa·s}$. The computational domain is $4L \times 5L \times 4L$, and the suspending fibers have diameter of $D = 0.4$ LBM unit lattice size.

3.1 Relative viscosity

To examine the effect of fiber stiffness on relative viscosity, three series cases with aspect ratio $r_p = 16$, 32 and 52 are considered. The results presented in figure 3.2, figure 3.3 and figure 3.4 clearly show that the fiber bending ratio (BR) has significant influence on the suspension's relative viscosity. In these figures, different symbols represent different fiber volume fraction, and simulations cover from the dilute to concentrated regime. When $BR < 3$, the suspension viscosity is indeed inversely related to the fiber stiffness, while for $BR > 3$, the fiber can be considered as rigid.

The difference between flexible fibers and rigid fibers is quite large. For fibers with the same aspect ratio, this difference increases as suspension concentration increases. For example, for fibers having aspect ratio $r_p = 32$, the relative viscosity η increases from 1.06 to 1.24 for volume fraction $c_{vf} = 0.018$, and from 1.18 to 1.81 for $c_{vf} = 0.035$, as shown in figure 3.3. The difference also increases with fiber aspect ratio for suspensions having the same fiber suspension concentration. For example, for suspensions having volume fraction $c_{vf} = 0.053$, η increases from 1.29 to 1.78 for $r_p = 16$ as shown in figure 3.2, and from 1.37 to 2.58 for $r_p = 32$ as shown in figure 3.3.

The relative viscosity of a flexible fiber suspension may be fitted using the empirical equation [70],

$$\eta = \eta_{rigid}\left(1 + \frac{A_0}{1 + e^{BR/A_1}}\right). \tag{80}$$

Here A_0 and A_1 are parameters that can be determined from the simulation data by least–squares curve–fitting. From the results shown in figure 3.2, figure 3.3 and figure 3.4, these two parameters are estimated to be

$$A_0 = r_p(1.00082c_{vf} + 0.69672c_{vf}^2), \qquad A_1 = 70/r_e^2. \tag{81}$$

Equation (80) is then used to fit the simulation data, as shown in figure 3.5, figure 3.6 and figure 3.7. This relation can be used to predict flexible fiber suspension viscosity. The relative viscosity of rigid fiber suspension can be easily found through existing methods; one only needs to know the fiber bending ratio BR, fiber aspect ratio r_p and the suspension volume fraction c_{vf} to find the two parameters (81) and then calculate the relative viscosity for flexible fiber suspension using (80).

The effect of fiber stiffness (bending ratio BR) on the relative viscosity can be explained based on the fiber orientation distribution. The relation based on Batchelor's theory is presented here. These equations are in principle valid only in the dilute regime. However, Batchelor's theory clearly relates rheological properties with

suspension microstructure, including the effects of hydrodynamic interactions. The equations are based on the fiber orientation distribution, implicitly including some of the effects of non–hydrodynamic interactions.

Based on the spherical coordinate system, as shown in figure 1.1, equation (12) becomes

$$\eta^B = 1 + \frac{\mu_{fiber}}{\mu} \left\langle p_x{}^2 p_y{}^2 \right\rangle = 1 + \frac{\mu_{fiber}}{4\mu} \left\langle \sin^4\theta \sin^2 2\phi \right\rangle. \tag{82}$$

Equation (82) shows that the fiber orientation has strong influence on the suspension shear viscosity. The shear stress has maximum value when fiber orientation angle ϕ is equal to $\pi/4$ or $3\pi/4$ and has minimum value when ϕ equal to 0, $\pi/2$ or π. In the present simulation, the orientation of every fiber at any given time step is given. It is advantageous to choose $\boldsymbol{p}$ so that $p_x \geqslant 0$ and $\phi \in [0, \pi)$. The probability distribution function obtained from the simulation is a discrete distribution. It was converted to a continuous distribution by using the Dirac delta function. For suspensions having n fibers, the probability function is

$$p(\phi) = \frac{1}{n} \sum_{i=1}^{n} \delta(\phi - \phi_i), \tag{83}$$

where $\phi_1, \cdots, \phi_n$ are the orientation angles for suspending fibers. This approach is applied for the remainder of this study.

Figure 3.8 to figure 3.16 show the ϕ distribution, with different aspect ratio, volume fraction and bending ratio BR for η depicted in figure 3.2, figure 3.3 and figure 3.4. For suspensions with the same volume concentration and fiber aspect ratio, decreasing bending ratio (more flexible fiber), the ϕ distribution becomes flatter showing that the suspending fibers are mostly oriented away from the xz–plane, thus increasing the suspension shear viscosity.

Also the asymmetry of the ϕ distribution, observed in the small BR range, indicates that the fiber–fiber mechanical interaction and fiber deformation are present at this regime. The consequences of this observation will be discussed further below.

It can also been seen in figure 3.8 to figure 3.16 that BR has stronger impact on more concentrated suspensions having the same fiber aspect ratio. For example, in the case of suspensions with fiber aspect ratio $r_p = 16$ at the same bending ratio $BR = 0.29$, the fiber orientation distribution $p(\phi)$ of the suspension with higher volume concentration is more flat and asymmetric as shown in figure 3.8, figure 3.9 and figure 3.10. Same pattern can be observed for suspensions with aspect ratio $r_p = 32$ and 52. This trend also causes the suspension's relative viscosity η to increase with fiber concentration as shown in figure 3.2, figure 3.3 and figure 3.4.

In figure 3.17, figure 3.18 and figure 3.19, the average number of contact points per fiber $\langle n_c \rangle$ is plotted as a function of the bending ratio BR for the same cases depicted in figure 3.2, figure 3.3 and figure 3.4. Mean values were taken for $\langle n_c \rangle$, by time averaging over one orbit period after preconditioning. The decrease of the bending ratio BR leads to the increase of $\langle n_c \rangle$, except in figure 3.17, for the very concentrated suspension with fiber volume fraction $c_{vf} = 0.124$; $\langle n_c \rangle$ increases first and then decreases from a very high value (~ 8). As $\langle n_c \rangle$ increases, fibers interact more frequently with increased contribution to the shear stress. The suspension shear viscosity increases with $\langle n_c \rangle$.

Fiber–fiber mechanical contacts can affect the suspension's microstructure and rheology in two ways: First, the contacts can change the Jeffery's orbit of the suspending fibers, and change the orientation distribution of the fibers, and consequently change the rheological properties of the suspension. Second, the lubrication force and contact force associated with fiber–fiber interaction will increase the suspension shear stress, and increase the relative viscosity of the fiber suspension. Koch and coworkers [74, 101, 112] have found that mechanical contacts can decrease the fiber rotation period. This is easy to understand, since based on Jeffery's equation (4), fiber spends most of the time in the positions that are close to the xz–plane as shown in figure 1.1. However, fiber–fiber interactions will push the fiber away from these positions.

This change on the fiber flipping decreases the time that the fiber spends around the xz–plane, changes the orientation distribution of the suspending fiber and the suspension rheology.

Figure 3.1 shows ten different combinations of fiber–fiber contact. In all cases, the fiber on the left is stationary and the fiber on the right is moving with the relative velocity U_{rel}. In the first six cases, the interaction interface is close to a point, but in the last four cases, the region of contact is a straight or curved line. The relative motions in these cases are also very different. In (a), (c), (e), (g), the relative motion is normal to the surface, and in (b), (d), (f), (h), the surfaces are in shear. In the real experiments and simulations, the situation could be even more complicated, especially for flexible fiber suspensions as shown in cases (i) and (j), which have different local curvature for fibers with different BR. The relative position and motion could be the combination of these example cases. In different cases, the models for interaction forces should be different.

One limitation of the current flexible fiber model is that, it treats different kind of contacts in the same manner, the criteria of the onset of contact are the same, the lubrication force and contact force are only depend on the shortest distance and the relative velocity between two contacting fibers. Another limitation is that, the number of contacts between two fibers is only counted once in the simulation. However, for flexible fiber suspensions, two neighboring fibers could have more than two contact points. The current contact model also does not include multi–body contacts. The last two limitations can strongly affect the result of $\langle n_c \rangle$, especially in the case of very concentrated suspension with very flexible suspending fibers. In the cases of $BR = 0.04$, 0.11, 0.42, and $c_{vf} = 0.124$, as shown in figure 3.17, $\langle n_c \rangle$ is under estimated in these situations. These limitations have been explained in section §5.2. The fiber–fiber interaction model could be an interesting subject in the future study.

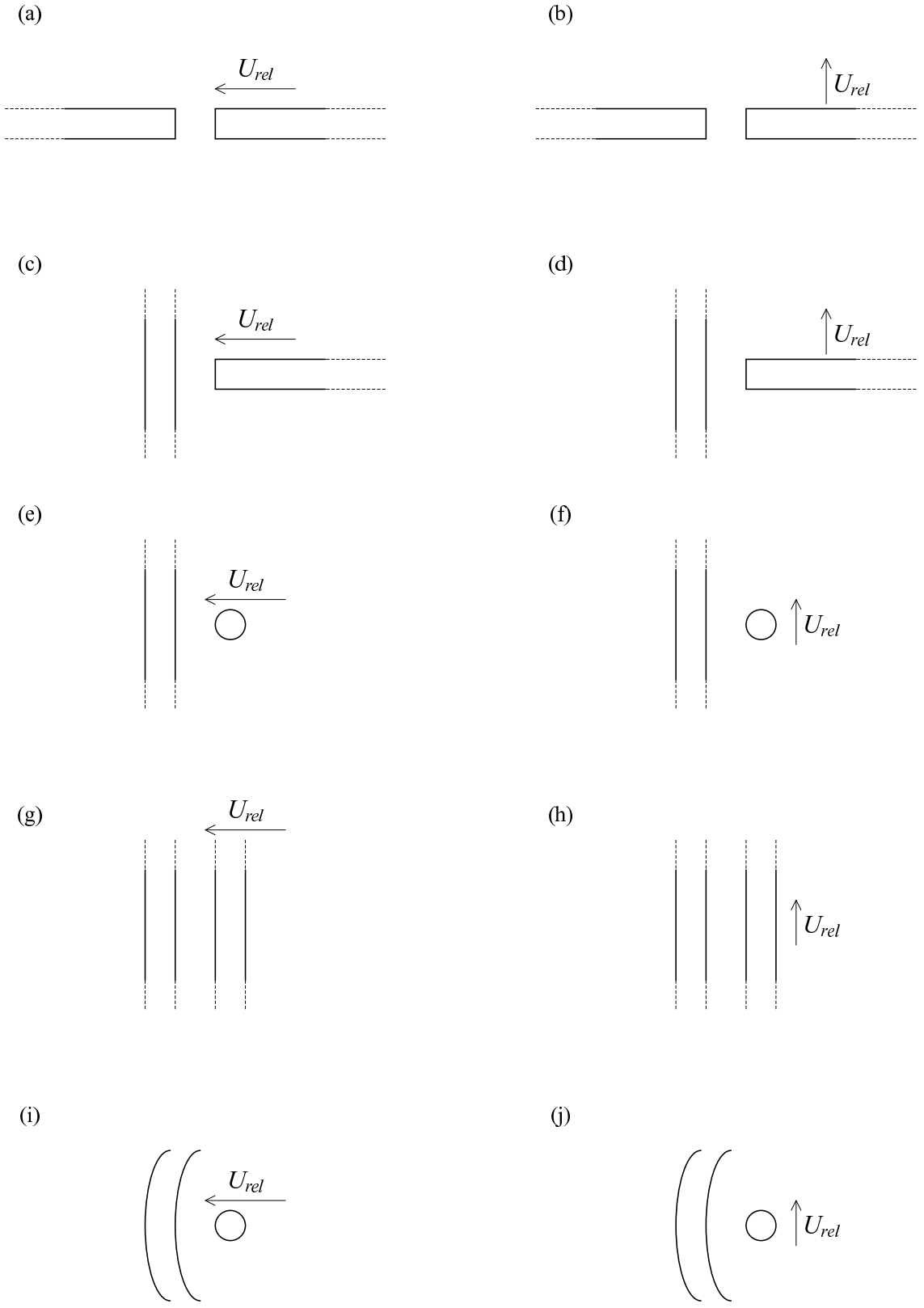The plots of $\langle n_c \rangle$ also confirm the previous observation that the relative viscosity

69

Figure 3.1: Ten different cases of fiber–fiber contact.

η of the flexible fiber suspensions increases with fiber aspect ratio. For example, for suspensions having volume fraction $c_{vf} = 0.018$, $\langle n_c \rangle$ increases from 0.78 to 1.25 for $r_p = 16$ as shown in figure 3.17, from 1.03 to 1.97 for $r_p = 32$ as shown in figure 3.18 and from 1.00 to 2.13 for $r_p = 52$ as shown in figure 3.19. For longer flexible fiber, decreasing bending ratio will make it easier to contact with its neighbors.

3.1.1 Relative viscosity η
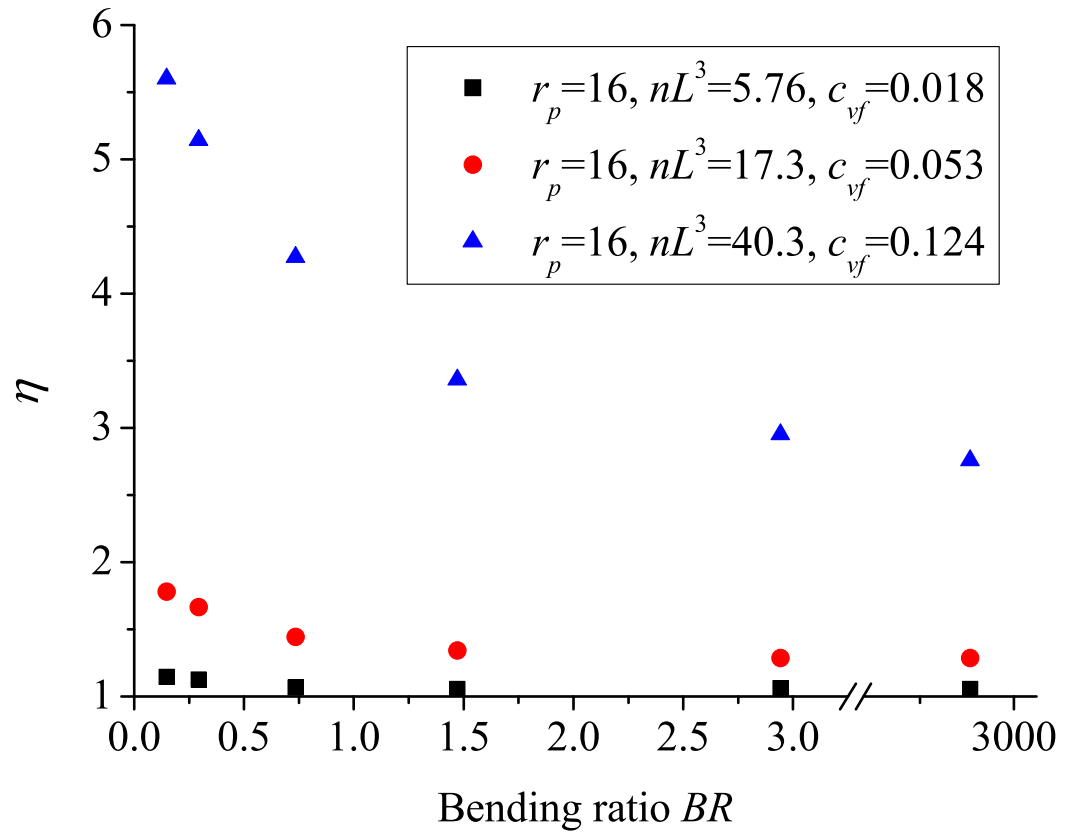
Figure 3.2: The relative shear viscosity η *vs.* bending ratio BR. Fiber aspect ratio $r_p = 16$, volume fraction $c_{vf} = 0.018$, 0.053 and 0.124.
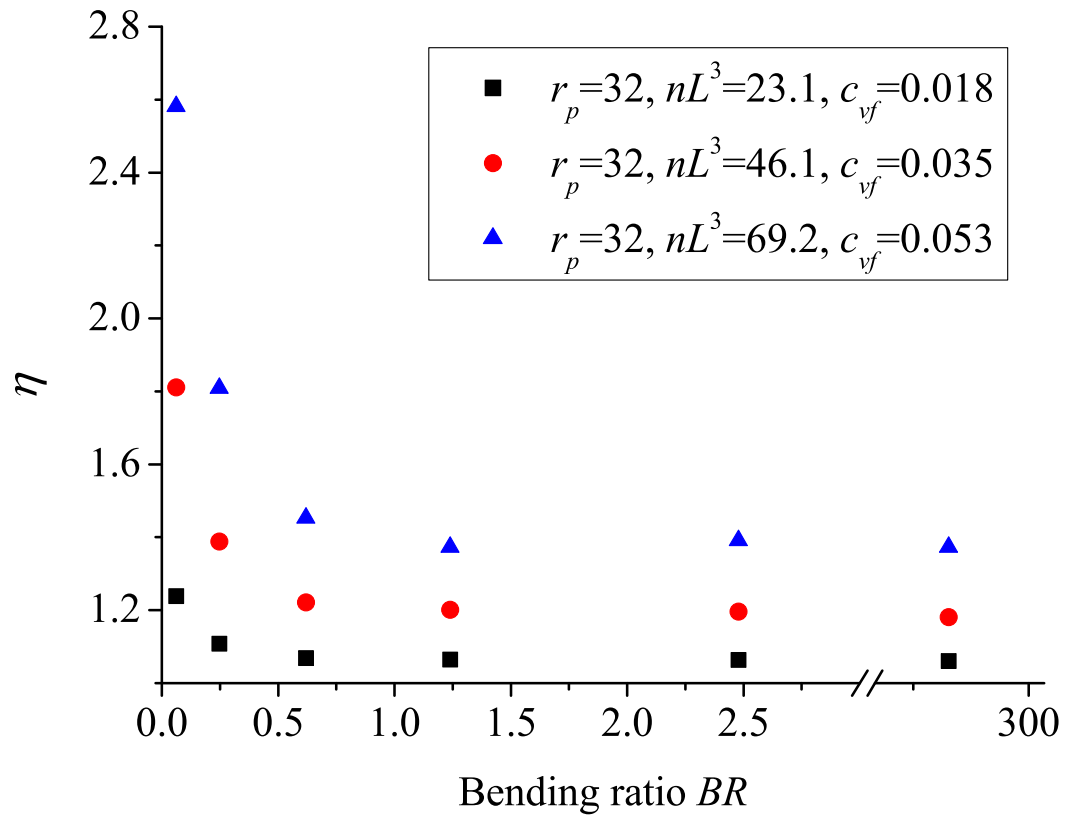
Figure 3.3: The relative shear viscosity η $vs.$ bending ratio BR. Fiber aspect ratio $r_p = 32$, volume fraction $c_{vf} = 0.018$, 0.035 and 0.053.
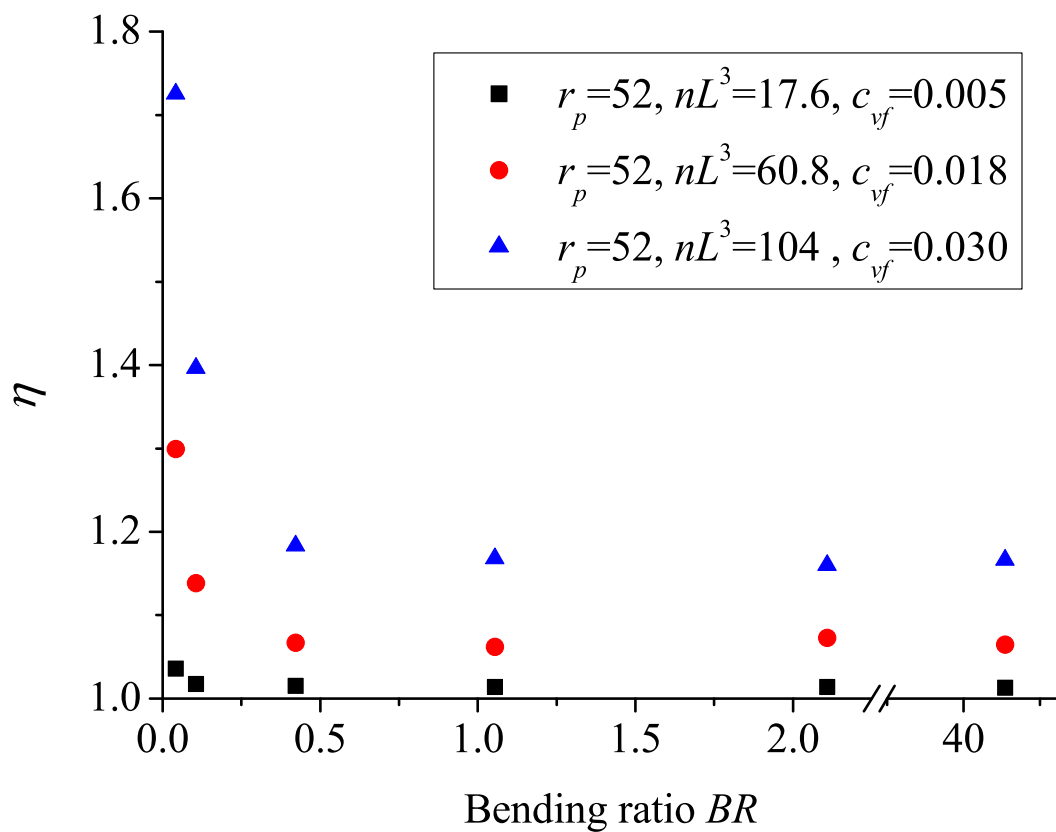
Figure 3.4: The relative shear viscosity η *vs.* bending ratio BR. Fiber aspect ratio $r_p = 52$, volume fraction $c_{vf} = 0.005$, 0.018 and 0.030.
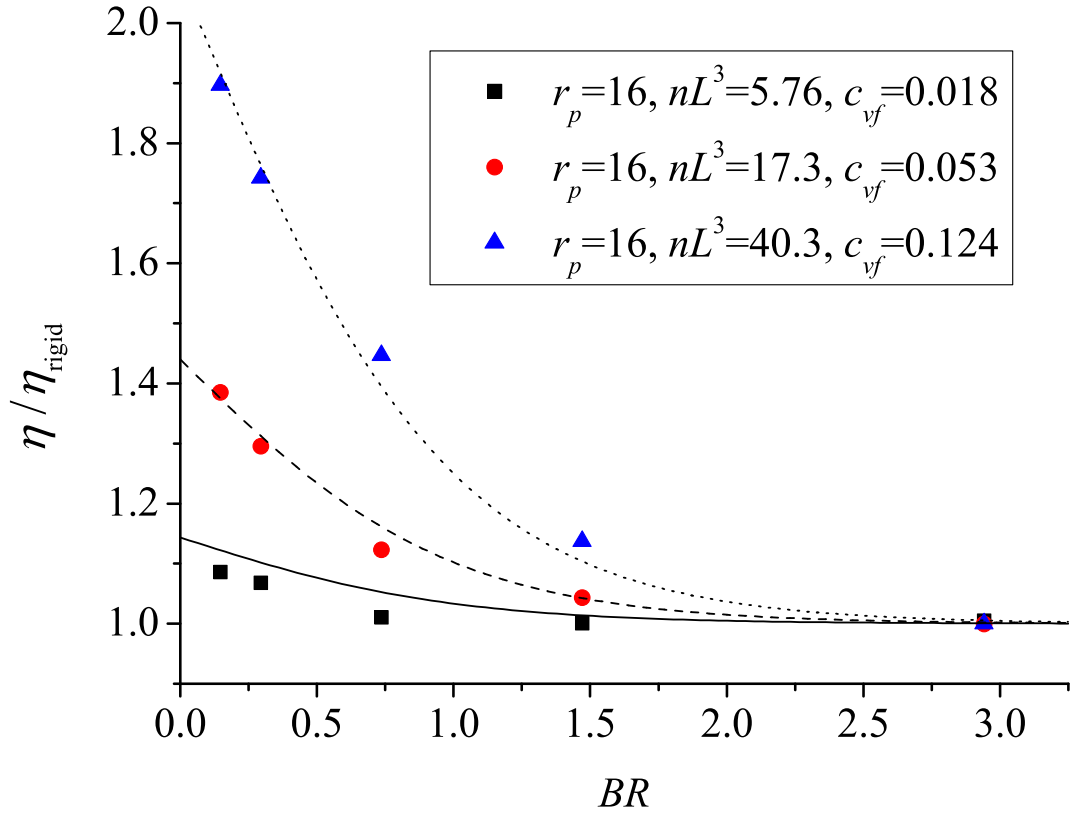
Figure 3.5: Normalized relative viscosity η/η_{rigid} *vs.* fiber bending ratio BR for flexible fiber suspensions. Fiber aspect ratio $r_p = 16$, volume fraction $c_{vf} = 0.018$, 0.053 and 0.124. The solid line (—), dash line (- - -) and dot line ($\cdots$) are the corresponding curve–fitting results.
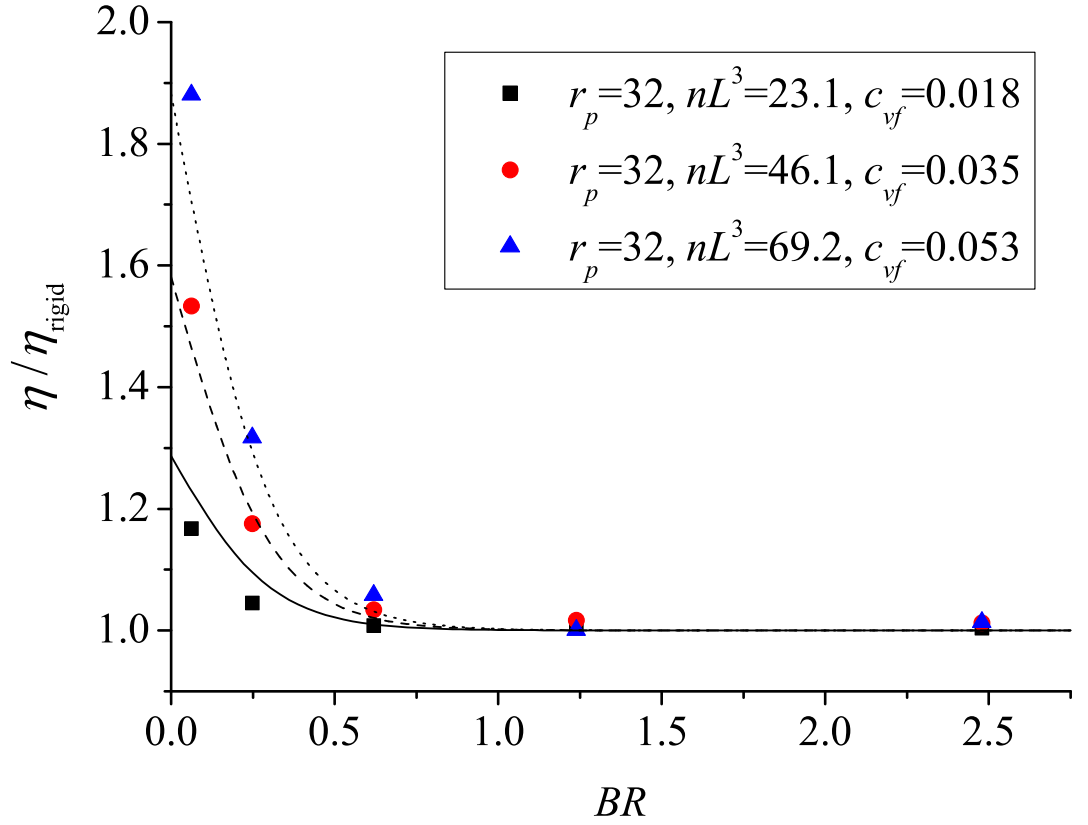
Figure 3.6: Normalized relative viscosity η/η_{rigid} *vs*. fiber bending ratio BR for flexible fiber suspensions. Fiber aspect ratio $r_p = 32$, volume fraction $c_{vf} = 0.018$, 0.035 and 0.053. The solid line (—), dash line (- - -) and dot line ($\cdots$) are the corresponding curve–fitting results.
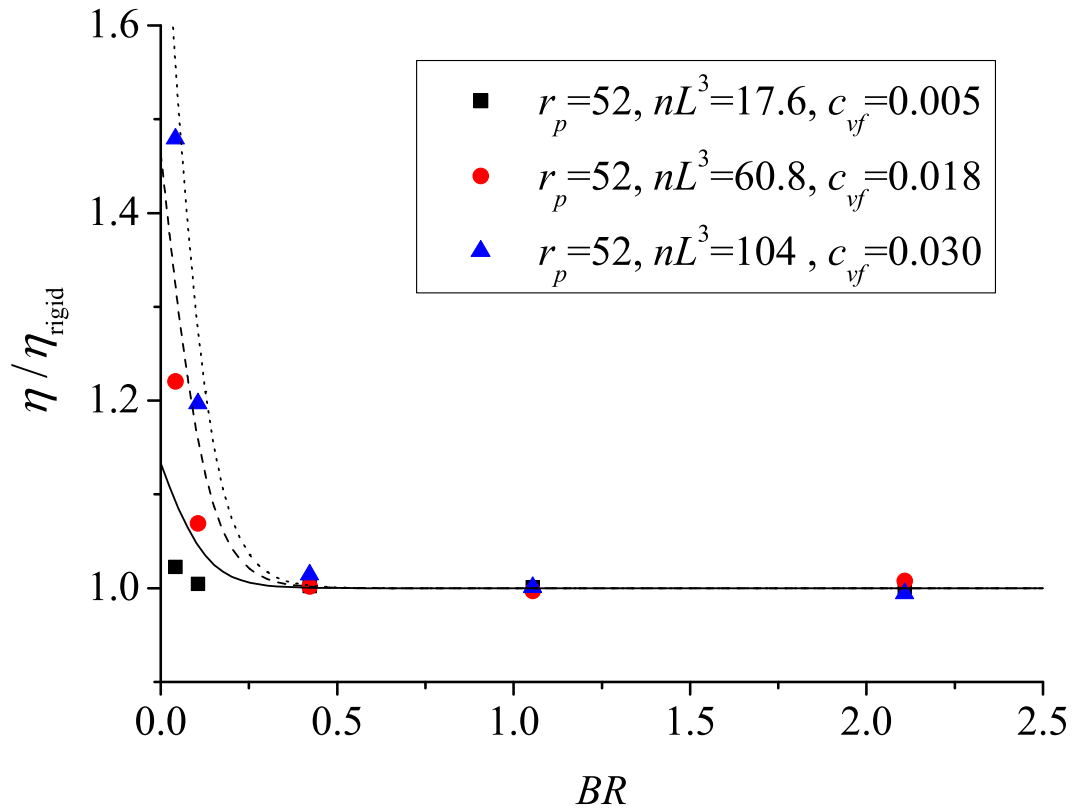
Figure 3.7: Normalized relative viscosity η/η_{rigid} vs. fiber bending ratio BR for flexible fiber suspensions. Fiber aspect ratio $r_p = 52$, volume fraction $c_{vf} = 0.005$, 0.018 and 0.030. The solid line (—), dash line (- - -) and dot line ($\cdots$) are the corresponding curve–fitting results.

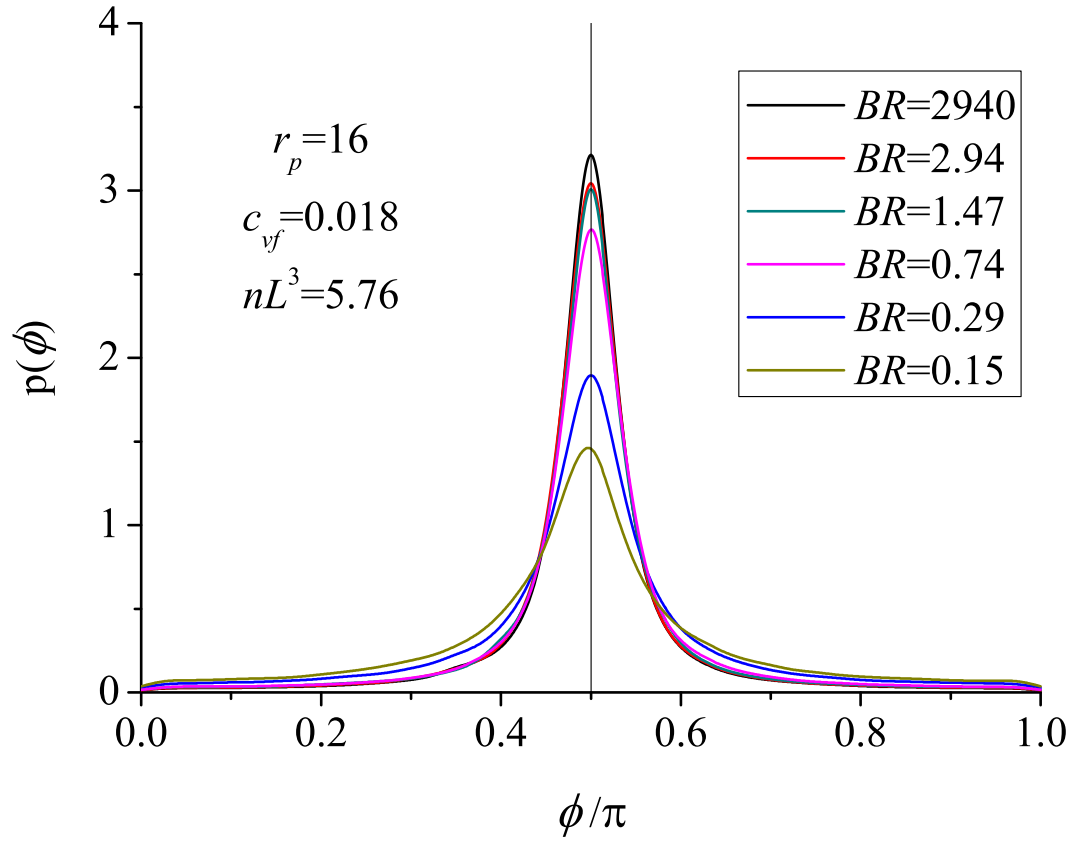## 3.1.2 Fiber orientation distribution $p(\phi)$

Figure 3.8: The ϕ distribution for different bending ratio BR. Fiber aspect ratio $r_p = 16$, volume fraction $c_{vf} = 0.018$.

Figure 3.9: The ϕ distribution for different bending ratio BR. Fiber aspect ratio $r_p = 16$, volume fraction $c_{vf} = 0.053$.

Figure 3.10: The ϕ distribution for different bending ratio BR. Fiber aspect ratio $r_p = 16$, volume fraction $c_{vf} = 0.124$.

Figure 3.11: The ϕ distribution for different bending ratio BR. Fiber aspect ratio $r_p = 32$, volume fraction $c_{vf} = 0.018$.

Figure 3.12: The ϕ distribution for different bending ratio BR. Fiber aspect ratio $r_p = 32$, volume fraction $c_{vf} = 0.035$.
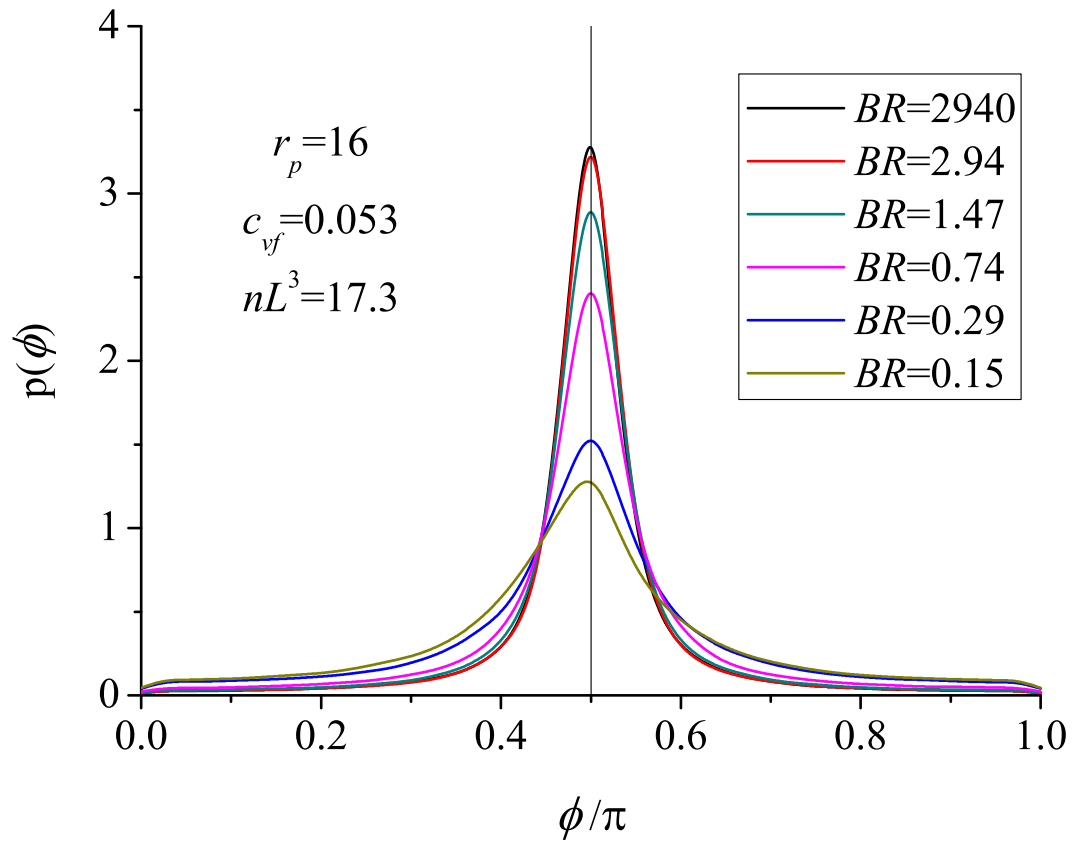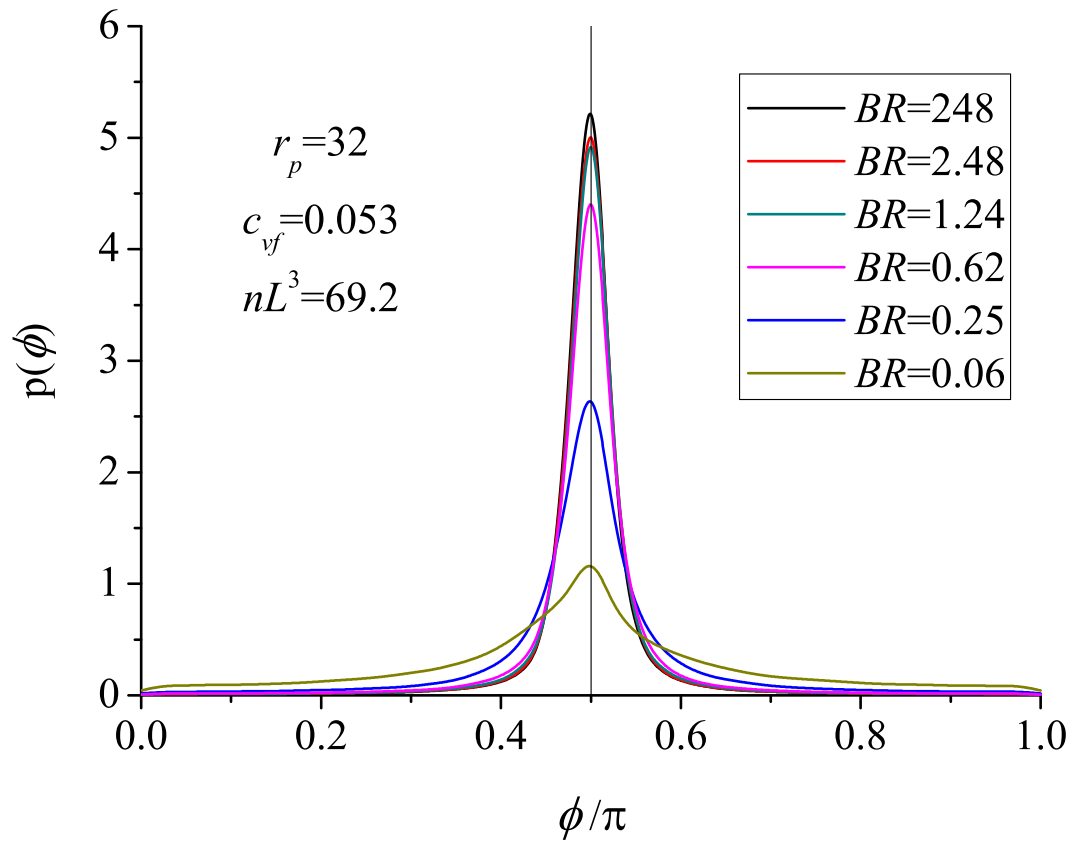
Figure 3.13: The ϕ distribution for different bending ratio BR. Fiber aspect ratio $r_p = 32$, volume fraction $c_{vf} = 0.053$.
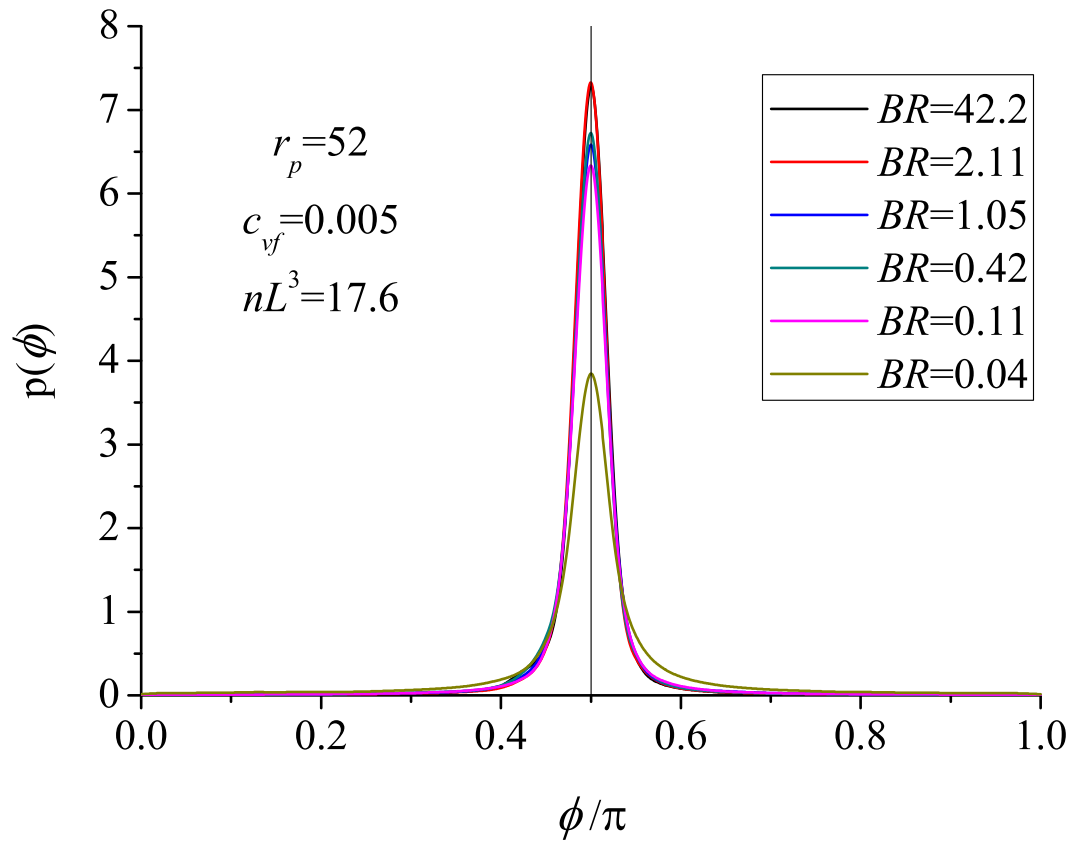
Figure 3.14: The ϕ distribution for different bending ratio BR. Fiber aspect ratio $r_p = 52$, volume fraction $c_{vf} = 0.005$.
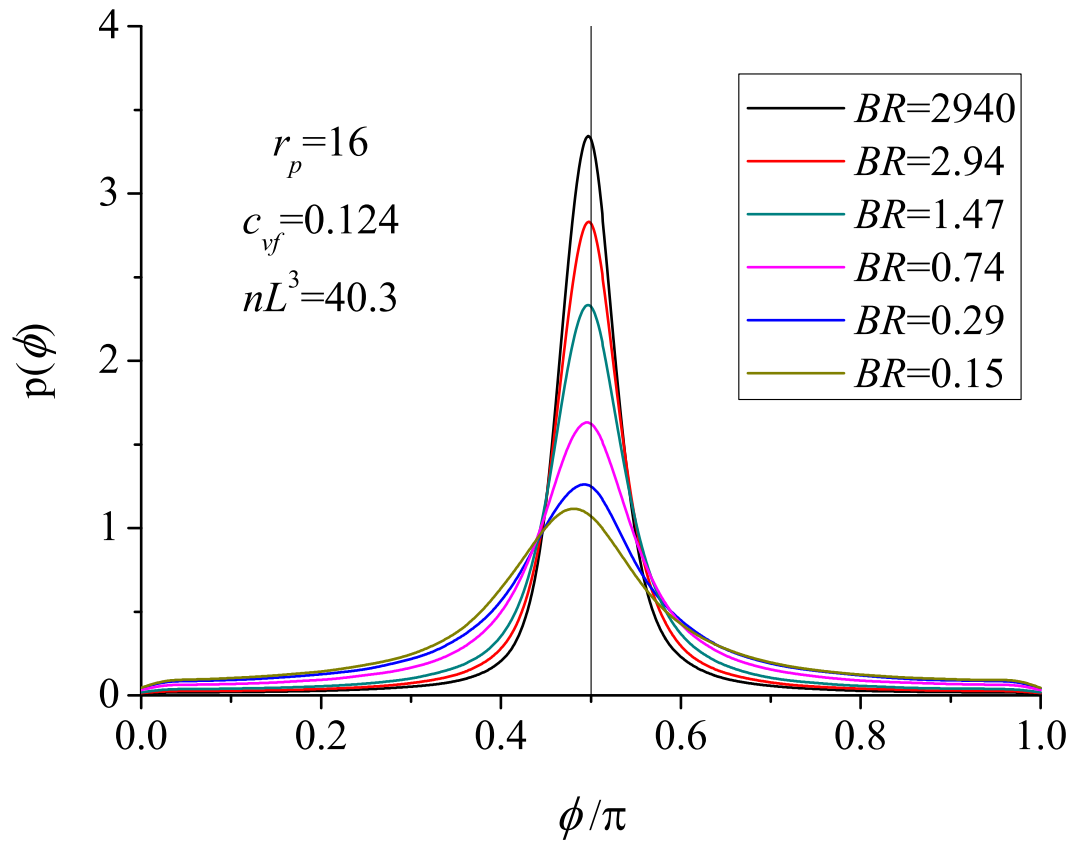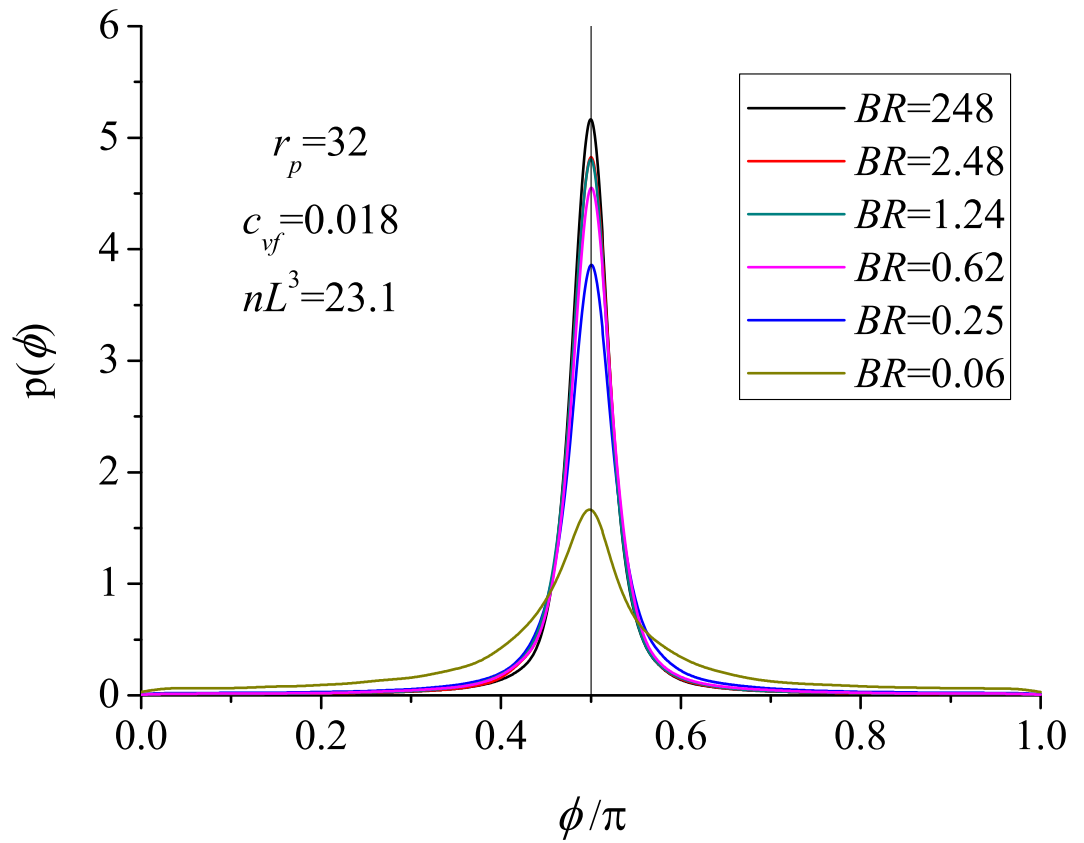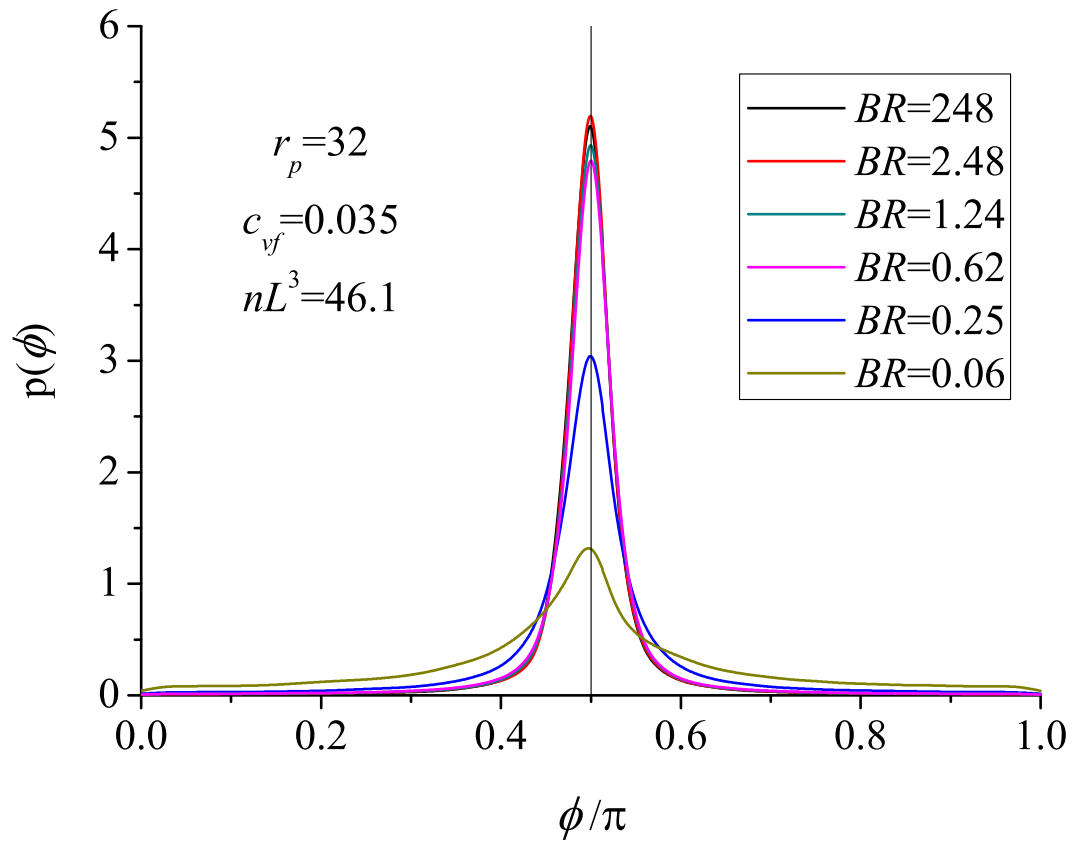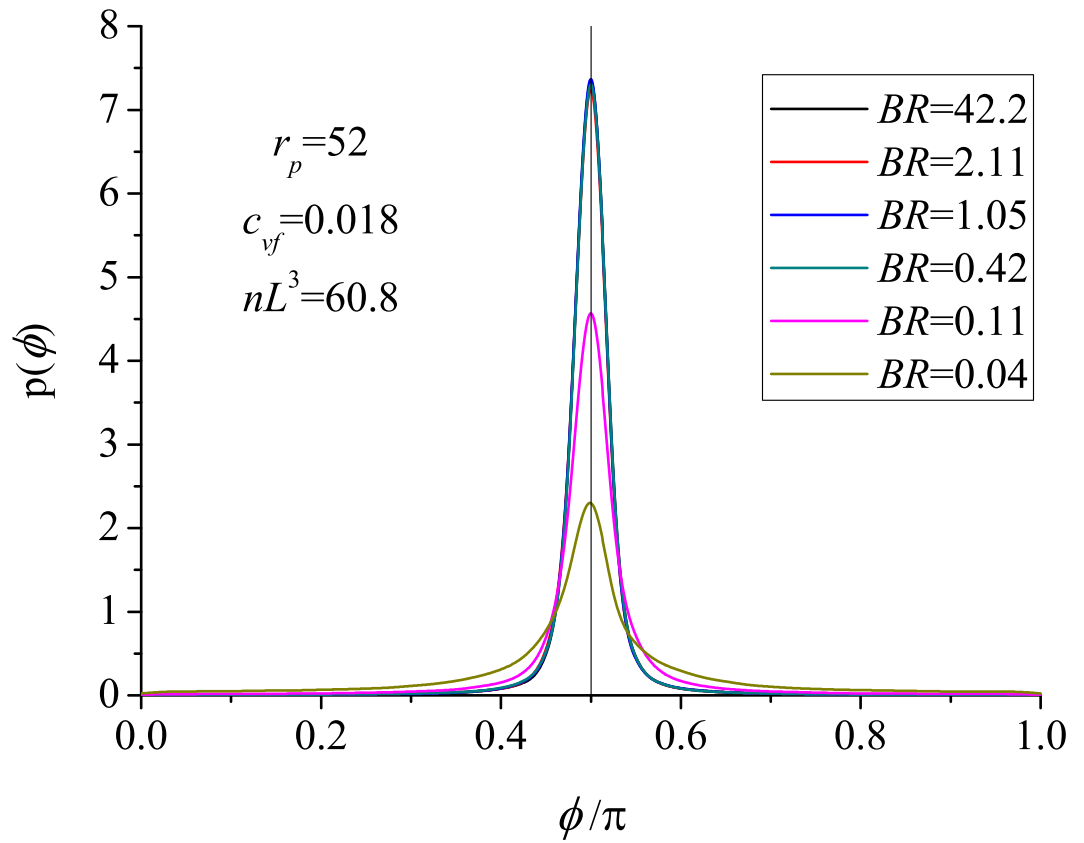
Figure 3.15: The ϕ distribution for different bending ratio BR. Fiber aspect ratio $r_p = 52$, volume fraction $c_{vf} = 0.018$.
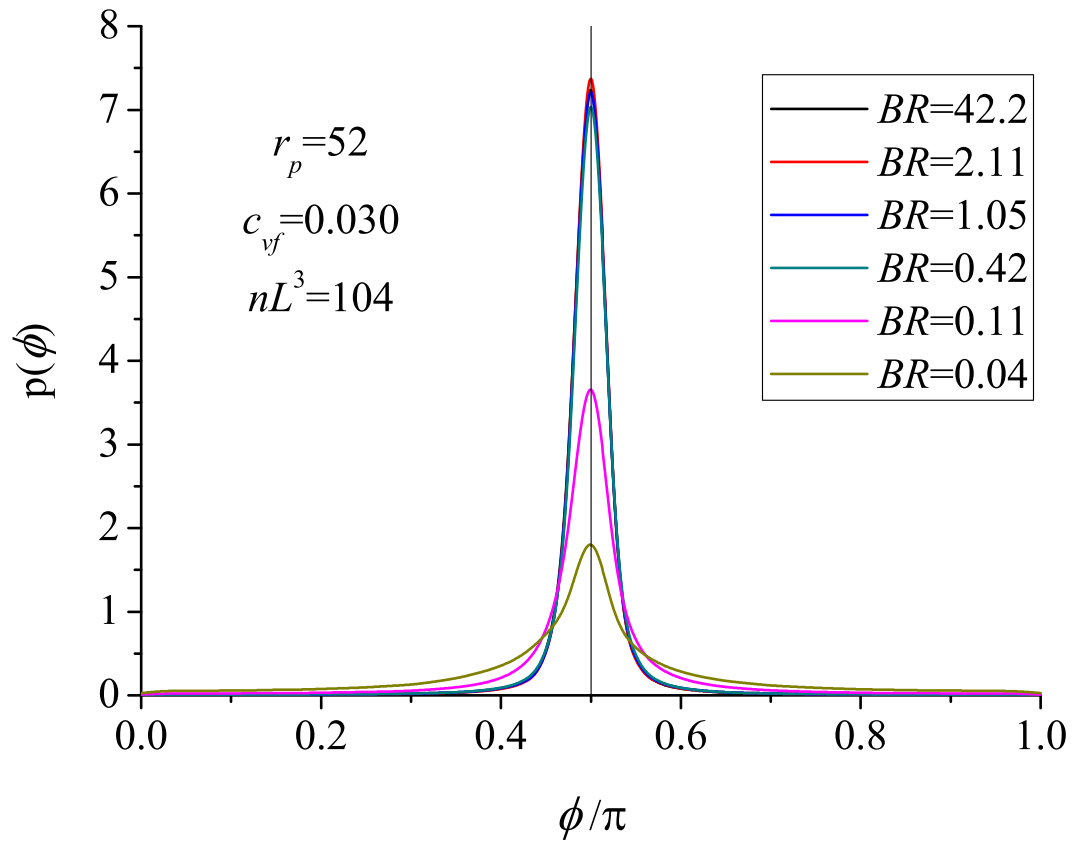
Figure 3.16: The ϕ distribution for different bending ratio BR. Fiber aspect ratio $r_p = 52$, volume fraction $c_{vf} = 0.030$.

3.1.3 Average number of contact points per fiber $\langle n_c \rangle$

Figure 3.17: The average number of contact points per fiber $\langle n_c \rangle$ *vs.* bending ratio BR. Fiber aspect ratio $r_p = 16$, volume fraction $c_{vf} = 0.018$, 0.053 and 0.124.

Figure 3.18: The average number of contact points per fiber $\langle n_c \rangle$ *vs.* bending ratio BR. Fiber aspect ratio $r_p = 32$, volume fraction $c_{vf} = 0.018$, 0.035 and 0.053.

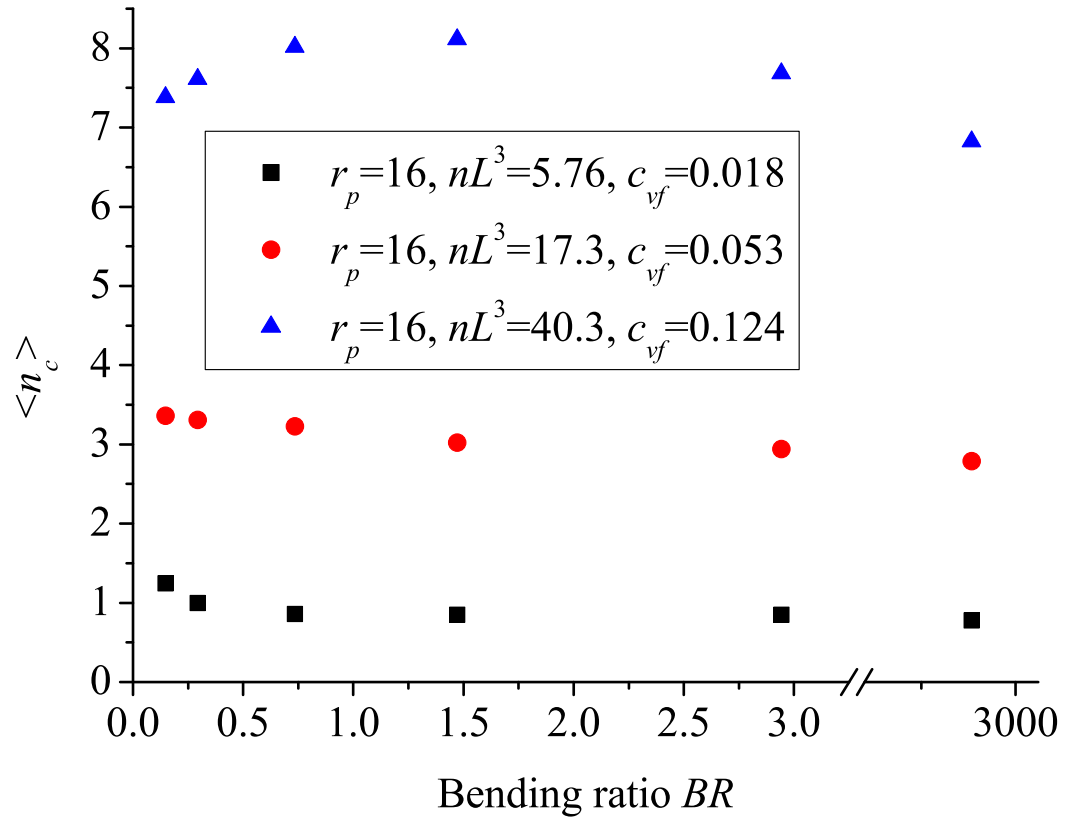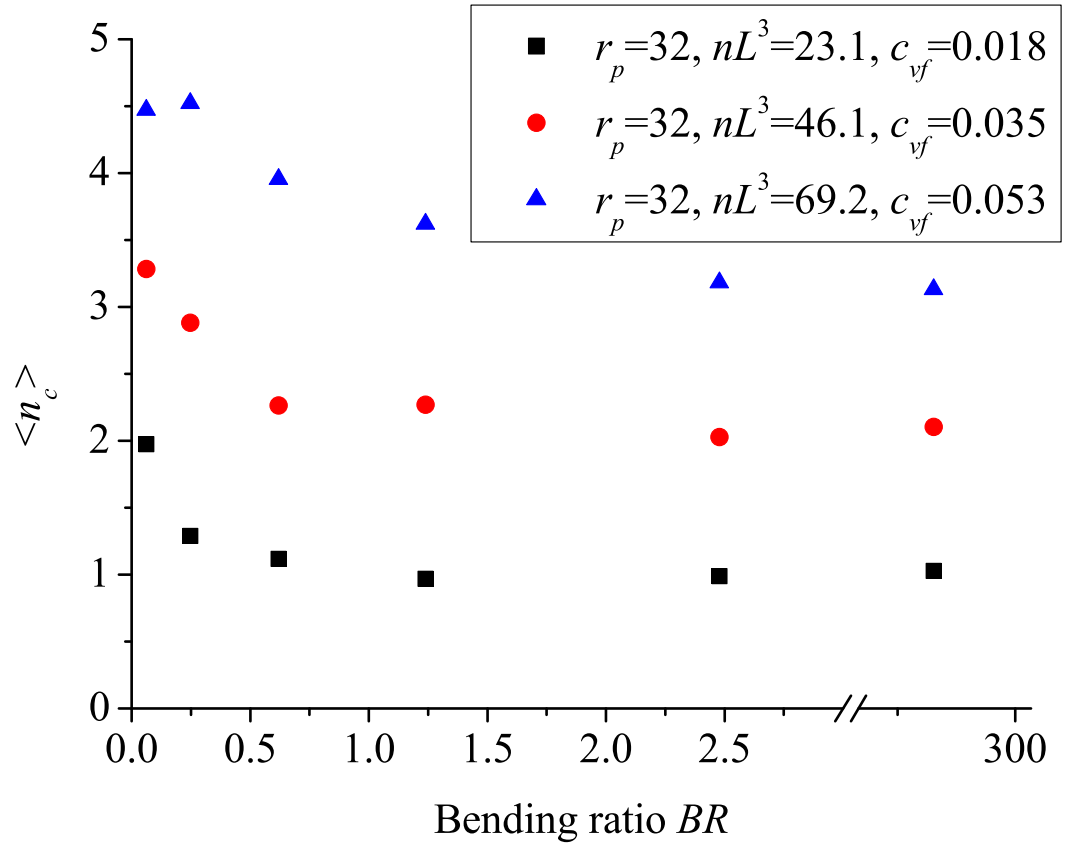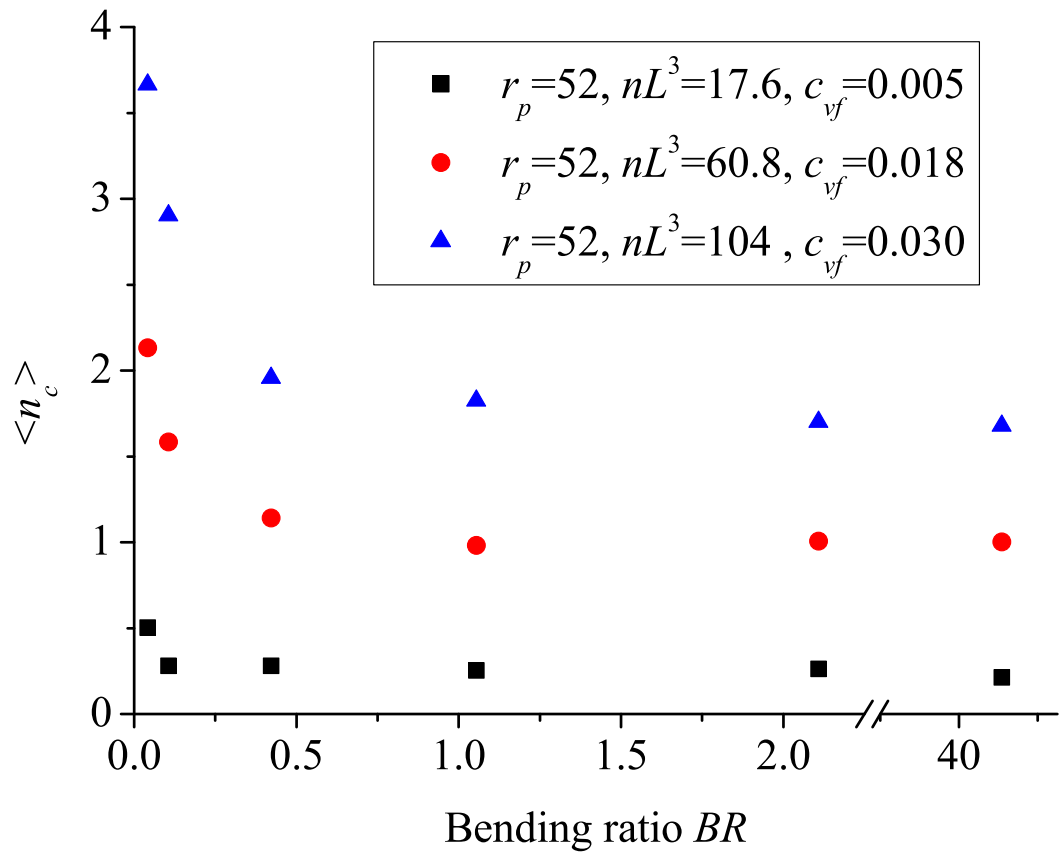**Figure 3.19:** The average number of contact points per fiber $\langle n_c \rangle$ *vs.* bending ratio BR. Fiber aspect ratio $r_p = 52$, volume fraction $c_{vf} = 0.005$, 0.018 and 0.030.

3.2 First normal stress difference

In this section, the dependence of the first normal stress difference N_1 on the fiber stiffness BR and fiber volume fraction c_{vf} is investigated. First, the simulation results are compared with experimental results from the literature as shown in figure 3.20. Petrich $et\ al.$ [98] and Carter [25] performed experiments in semi–dilute and concentrated regimes with results showing similar patterns with some discrepancy. Petrich $et\ al.$ also measured the average value of $(\langle p_x{}^3 p_y \rangle - \langle p_y{}^3 p_x \rangle)$ and calculated the Batchelor's first normal stress difference N_1^B by using equation (13), as shown in figure 3.20. The value of N_1^B computed by Petrich $et\ al.$ is much lower than the experimental result. The discrepancy increases with fiber concentration. As previously discussed, Batchelor's theory only includes hydrodynamic contributions, but in the semi–dilute and concentrated regimes, non–hydrodynamic interactions and fiber–fiber interactions become important. Present simulation results are more close to Carter's experimental results with the same discrepancy compared to Batchelor's solutions.

Based on the following relation, Carter [25] predicts the first normal stress difference for rigid fiber suspensions.

$$\frac{N_1^C}{\mu\dot{\gamma}} \propto \frac{c_{vf} r_p{}^2}{\ln(2r_p) - 1.8} \langle\sin(2\phi)\rangle. \tag{84}$$

He assumes that $\langle\sin(2\phi)\rangle \propto \sqrt{1/r_p}$, and equation (84) can be written as

$$\frac{N_1^C}{\mu\dot{\gamma}} = K_c \frac{c_{vf} r_p{}^{3/2}}{\ln(2r_p) - 1.8}, \tag{85}$$

where K_c is a constant to be determined experimentally. Different investigators applied Carter's model to their normal stress measurements [25, 73, 54, 132, 98, 106, 71]. These experimental data fall within a range for K_c from 0.04 to 0.32, although no clear relation between K_c and variables such as fiber volume fraction and aspect ratio has been discovered. We also implemented Carter's formula with our simulation results with $K_c = 0.08$, same as Petrich $et\ al.$ [98] ($K_c = 0.08$) and close to Keshtkar $et\ al.$ [71] ($K_c = 0.1 \pm 0.01$) in their studies, as shown in figure 3.20.

90

Carter's equation overpredicts the first normal stress difference in the dilute and semi–dilute regimes, most likely because the assumption of the $\langle\sin(2\phi)\rangle$ is not correct in those regimes. This was confirmed by Lindstrom and Uesaka [83] who showed that $\langle\sin(2\phi)\rangle$ is proportional to c_{vf}, not $\sqrt{1/r_p}$ in the dilute regime. It will continue to increase with the volume fraction and, in the concentrated regime, $\langle\sin(2\phi)\rangle$ becomes a constant and proportional to $\sqrt{1/r_p}$. The results from Carter's formula become more accurate as volume concentration increases. The same trend is also observed when comparing Carter's formula with our simulation results.

Figure 3.21, figure 3.22 and figure 3.23 show the effect of fiber flexibility on the non–dimensional fiber normal stress difference for fibers with aspect ratio $r_p = 16$, 32 and 52. These results show that an increase in fiber volume fraction leads to an increase of the first normal stress difference, and higher volume fraction will cause more fiber–fiber interaction and consequently increase N_1. A surprising finding, however, is that for suspensions that have the same fiber volume fraction, the first normal stress difference will decrease with decreasing bending ratio until $BR \sim 1$ and will then increase with the decreasing BR. A similar trend is also found from the experimental data of Keshtkar *et al.* [71]. The physical explanation for these simulation results can be provided with aid from Batchelor's theory.

Based on the spherical coordinate system, as shown in figure 1.1, (13) becomes

$$N_1^B = \mu_{fiber}\dot{\gamma}\left(\langle p_x{}^3 p_y\rangle - \langle p_y{}^3 p_x\rangle\right) = -\frac{\mu_{fiber}\dot{\gamma}}{4}\left(\langle\sin^4\theta\sin4\phi\rangle\right). \tag{86}$$

Equation (86) shows that if the suspension has no direct physical contact between fibers and if there is no fiber deformation (rigid fiber), the fiber orientation distribution $p(\phi)$ would necessarily be symmetric about xz–plane. Therefore, $N_1^B = 0$, since it is an odd function of p_y. In other words, if direct contact between fibers exists or if fibers are deformable, N_1^B will not vanish. Figure 3.8 to figure 3.16 clearly show that for decreasing bending ratio BR (more flexible fiber), the mean orientation angle $\langle\phi\rangle$ becomes slightly less than $\pi/2$, $\langle\sin4\phi\rangle$ becomes a small negative value, and this small

asymmetry of the fiber orientation distribution makes N_1^B become a positive value based on (86).

On the other hand, the orientation distribution of θ is also very important for the first normal stress difference, as shown in equation (86). N_1^B increases with θ, where θ is directly related to the orbit constant C_b, and C_b can be calculated numerically for every fiber with equation (5). Figure 3.24, figure 3.25 and figure 3.26 show the relation between the mean orbit constant $\langle C_b \rangle$ and the fiber bending ratio.

Based on bending ratio BR and equation (86), the relation between θ, $p(\phi)$ and N_1^B can be divided into two regimes. When $BR > 1$, the suspending fibers are rigid or slightly deformable. The suspensions have similar fiber orientation distribution, $p(\phi)$, as shown in figure 3.8 to figure 3.16 and the orientation angle θ is the main factor for changing N_1^B. Decreasing BR reduces the orientation angle θ and the mean orbit constant $\langle C_b \rangle$. N_1^B decreases with decreasing BR. When $BR < 1$, the suspending fibers become flexible. Both θ and $p(\phi)$ become important factors for N_1^B. In this regime, the suspending fibers are more randomly oriented and $\langle C_b \rangle$ increases with decreasing bending ratio, $\langle C_b \rangle \sim 0.45$ when $BR \to 0$. At the same time, the fiber orientation distribution $p(\phi)$ becomes more asymmetric and N_1^B increases with decreasing BR.

It is important to note that equation (86) only includes the hydrodynamic contributions from the suspension, and does not include non–hydrodynamic interactions and fiber–fiber interactions. So the first normal stress difference, shown in figure 3.21, figure 3.22 and figure 3.23, is not strictly proportional to the orbit constant C_b in figure 3.24, figure 3.25 and figure 3.26, even if they have the same fiber orientation distribution $p(\phi)$.
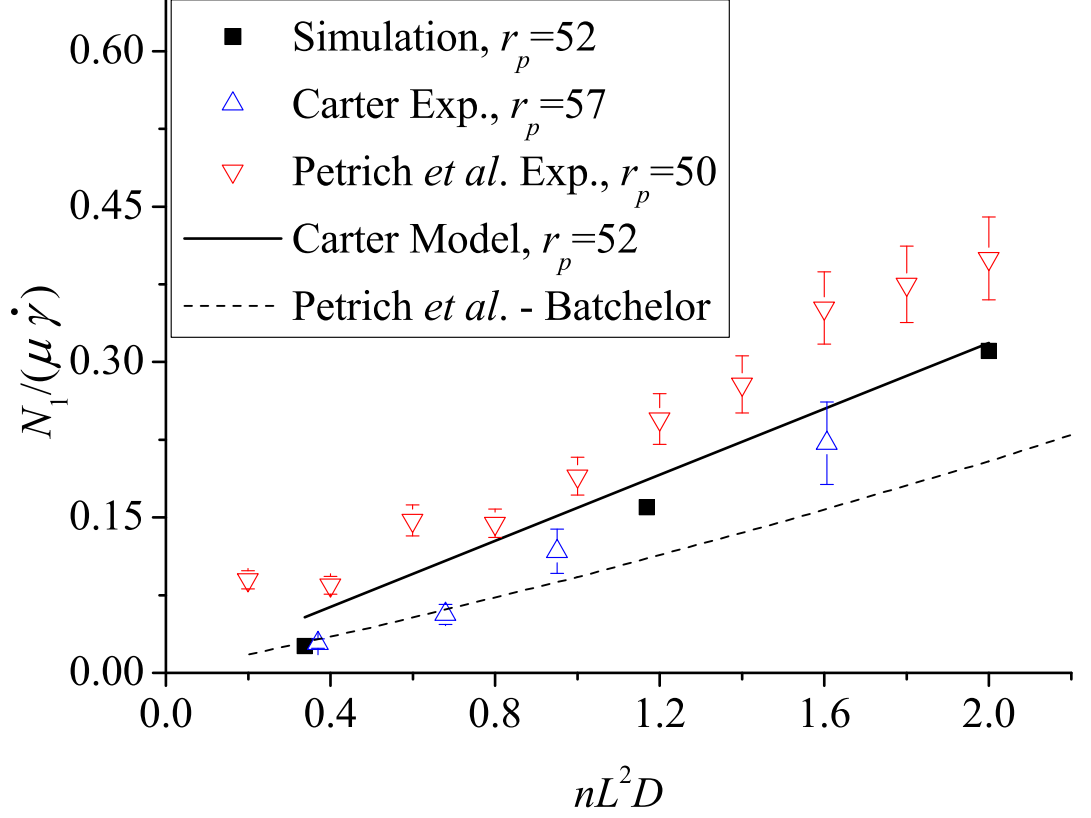
Figure 3.20: The non–dimensional first normal stress difference $N1/(\mu\dot{\gamma})$ as a function of nL^2D for rigid fiber suspensions. The open triangles ($\triangle$) are the experiment data of Carter [25] and the open upside–down triangles (∇) are the experiment data of Petrich *et al.* [98]. The solid line (—) is the prediction of Carter's model, equation (85), with $K_c = 0.08$. The dash line (- - -) is the Batchelor's first normal stress difference N_1^B, equation (13), calculated by Petrich *et al.* [98]. The solid squares ($\blacksquare$) are the simulation results from present LBM with EBF.

3.2.1   Non–dimensional first normal stress difference $N1/(\mu\dot{\gamma})$
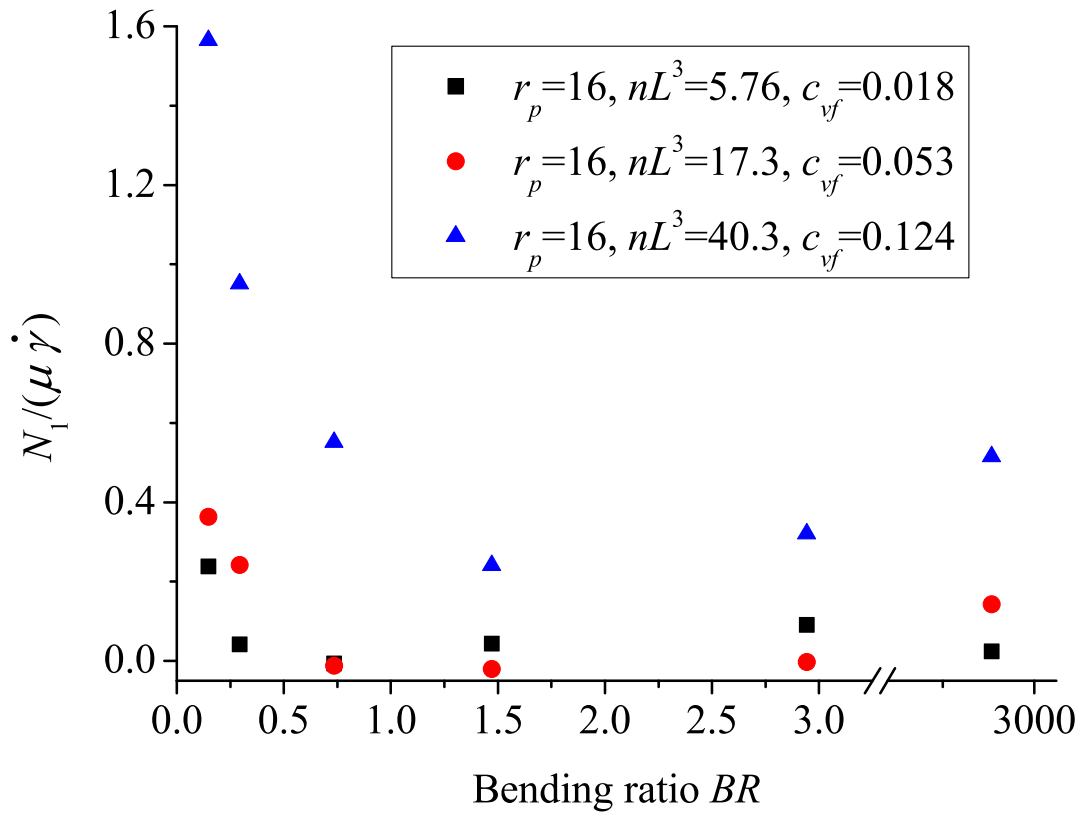
Figure 3.21: The non–dimensional first normal stress difference $N1/(\mu\dot{\gamma})$ *vs.* fiber bending ratio BR for flexible fiber suspensions. Fiber aspect ratio $r_p = 16$, volume fraction $c_{vf} = 0.018$, 0.053 and 0.124.
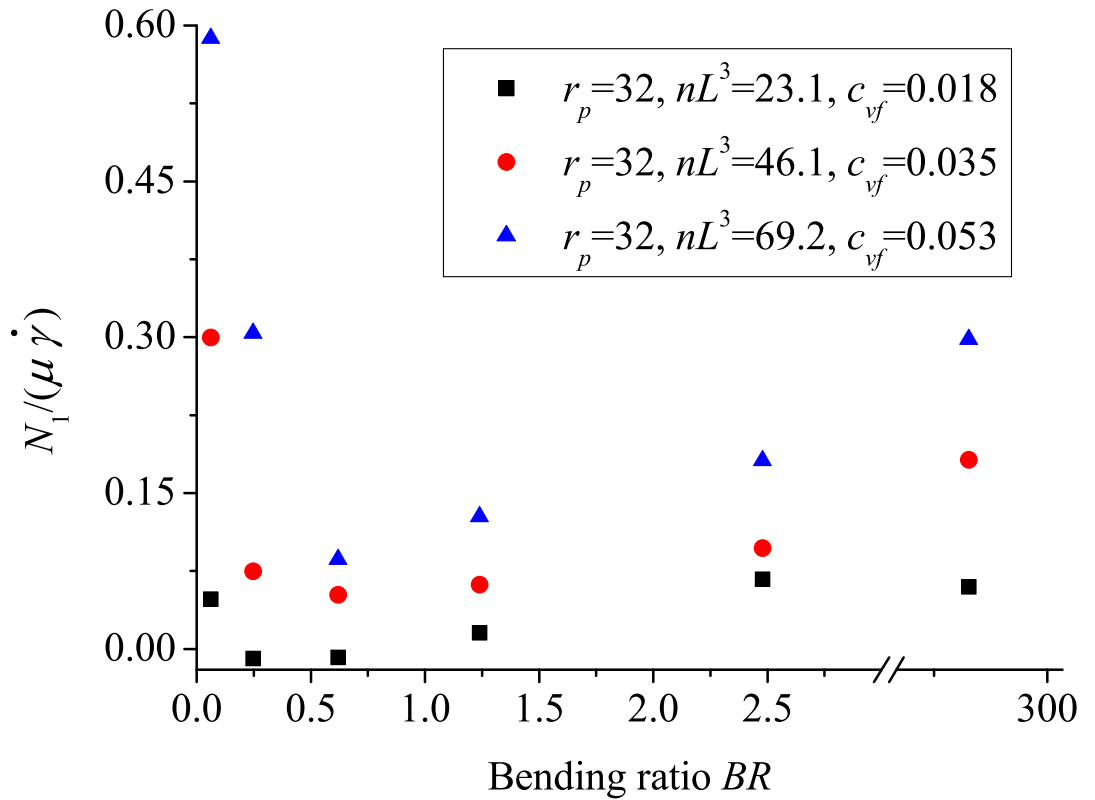
Figure 3.22: The non–dimensional first normal stress difference $N1/(\mu\dot{\gamma})$ *vs.* fiber bending ratio BR for flexible fiber suspensions. Fiber aspect ratio $r_p = 32$, volume fraction $c_{vf} = 0.018$, 0.035 and 0.053.
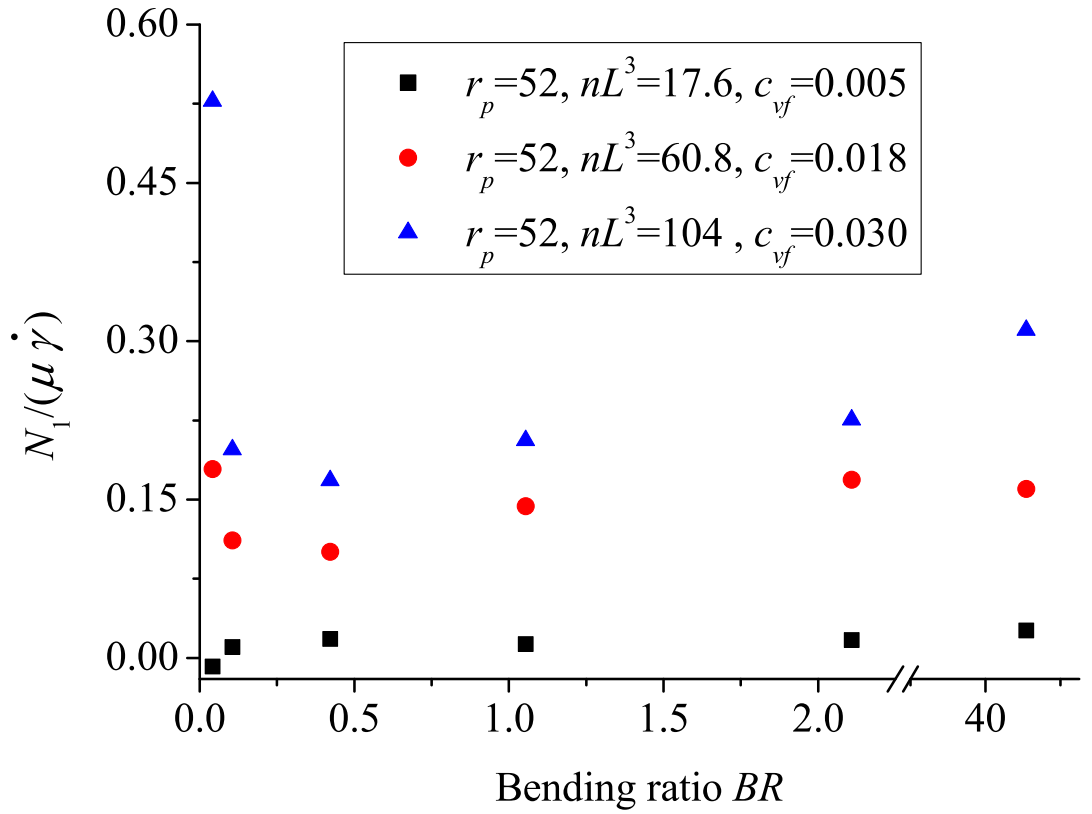
Figure 3.23: The non–dimensional first normal stress difference $N1/(\mu\dot{\gamma})$ *vs.* fiber bending ratio BR for flexible fiber suspensions. Fiber aspect ratio $r_p = 52$, volume fraction $c_{vf} = 0.005$, 0.018 and 0.030.

3.2.2 Mean orbit constant $\langle C_b \rangle$
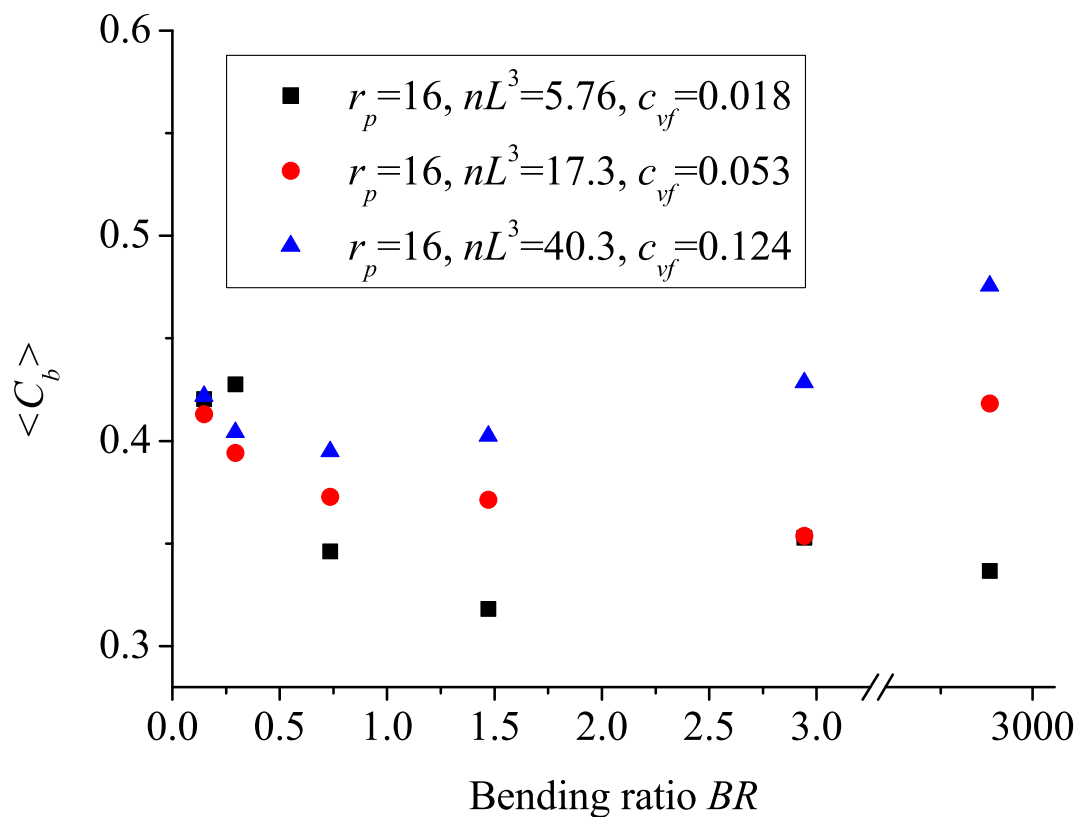
Figure 3.24: The mean orbit constant $\langle C_b \rangle$ *vs.* fiber bending ratio BR for flexible fiber suspensions. Fiber aspect ratio $r_p = 16$, volume fraction $c_{vf} = 0.018$, 0.053 and 0.124.

Figure 3.25: The mean orbit constant $\langle C_b \rangle$ *vs.* fiber bending ratio BR for flexible fiber suspensions. Fiber aspect ratio $r_p = 32$, volume fraction $c_{vf} = 0.018$, 0.035 and 0.053.
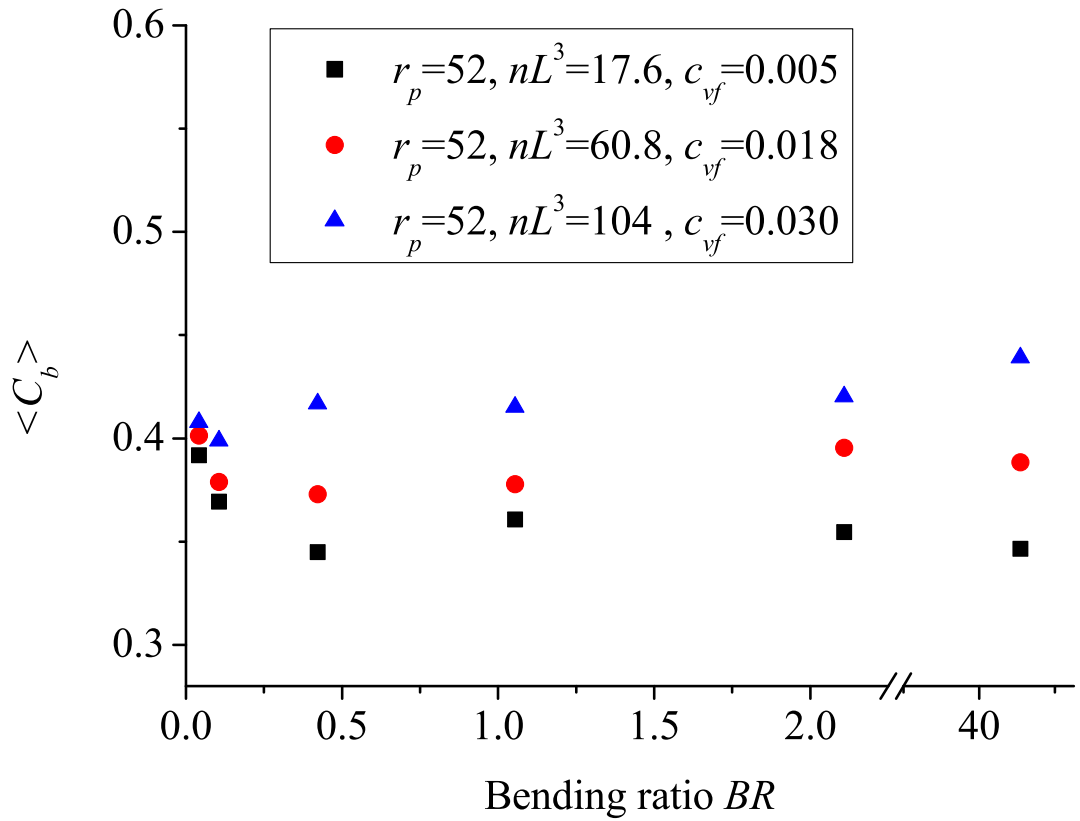
Figure 3.26: The mean orbit constant $\langle C_b \rangle$ *vs.* fiber bending ratio BR for flexible fiber suspensions. Fiber aspect ratio $r_p = 52$, volume fraction $c_{vf} = 0.005$, 0.018 and 0.030.
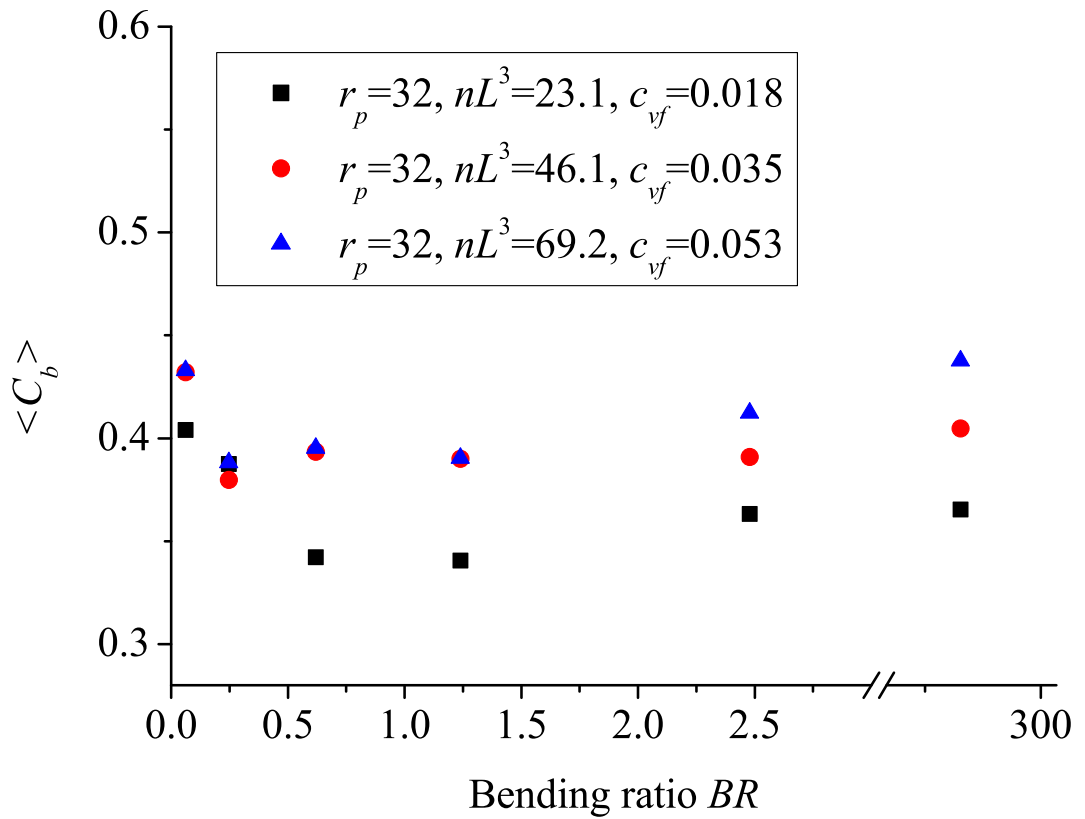
CHAPTER IV

PLATELET SIMULATION

4.1 *Background*

Bileaflet mechanical heart valves (BMHVs) have been widely used to replace native valves. Unfortunately, the design of bileaflet mechanical heart valves produces flow fields that may cause damage to blood elements, especially in the hinge area. Experimental work by Fallon [43] proved that channel geometry has a strong impact on platelet activation. In her thesis [43], by measuring the Thrombin–Antithrombin III (TAT) concentration of blood flow through the channels with different geometries and sizes, she concluded that for the small channels, size is more important to TAT formation than the geometry, but for the larger channels, the geometry play an important role. High fidelity simulations of the valve flow fields throughout the cardiac cycle are required to improve and refine existing valve designs, so as to ultimately develop BMHVs with minimal thromboembolic complications.

The objectives of this study are to analyze the flow properties for different channel geometries, and choose an appropriate blood damage index model. The new lattice Boltzmann method with external boundary force (LBM–EBF) simulation can help researchers further understand the cause of blood damage, and improve the design to reduce the adverse hemodynamic effects of valves that cause platelet activation and damage blood elements.

It has been established in the previous studies [123, 125] that hemodynamic shear stress is a primary biomechanical trigger for thromboembolic events . It is also well known that exposure time to shear stress is a critical parameter for platelet activation [50, 76, 114, 40, 96]. Several blood damage index models have been presented and

used in previous studies as a measure of blood damage. With a linear shear stress–exposure time model [40], the cumulative effects of shear stress and exposure time of a platelet can be computed as

$$BDI_D \equiv \frac{1}{n} \sum_{i=0}^{n} \tau_i \cdot \Delta t_i, \tag{87}$$

where BDI_D is the blood damage index, τ_i is the principal surface shear stress and Δt_i is the exposure time of platelet i.

Previous studies, however, have shown that the shear stress threshold for platelet activation is independent of exposure time [66]. Tambasco and Steinman [114] included a threshold shear stress parameter, in the linear BDI model by only considering platelets that have experienced high shear stress. Tambasco and Steinman's BDI model is defined as

$$BDI_T \equiv \frac{1}{n} \sum_{i=0}^{n} \tau_i^* \cdot \Delta t_i^*, \tag{88}$$

where BDI_T is the blood damage index, τ_i^* is the principal shear stress above the threshold and Δt_i^* is the exposure time. Tambasco and Steinman estimated the threshold stress for platelet activation to be 105 dyn/cm^2. The same threshold value was used in this study.

In the two afore mentioned models (equations (87) and (88)), the relationship between surface shear stress, exposure time and BDI value is linear. Other researchers found the actual relationship to be more complex. Wurzinger *et al.* [124] measured the amount of cytoplasm enzyme (LDH) released by platelets (which is proportional to the level of platelet activation) using a Couette–viscometer. Giersiepen *et al.* [50] derived a model for the blood damage index from the experimental results, given by

$$BDI_G \equiv \frac{1}{n} \sum_{i=0}^{n} \tau_i^{3.075} \cdot \Delta t_i^{0.77}. \tag{89}$$

One of the objectives of this research is to evaluate and compare these three different BDI models. In this study, we use a recently developed numerical method

[122, 121] to simulate flow with large numbers of platelets and calculate the BDI value for different geometries. By comparing the simulation results with existing experimental results [43], we can choose an appropriate blood damage index model for future numerical simulations.

4.2 Results

The platelets are modeled as ellipsoidal particles and are assumed to be neutrally buoyant in the suspending plasma. To numerically simulate the flow with platelets and to compare with Fallon's experiments [43], 40 platelets are released evenly along the radius of the channel with random azimuth angle at the inlet in the same channel geometries used in the experiments. By computing and recording the maximum shear stress on the platelet surface and the exposure time, three different BDI values are calculated for each platelet. For each platelet, the BDI values are weighted with the local flow rate at its initial position and added accordingly for each channel.

4.2.1 Experimental setup

In Fallon's experiments [43], four different geometries were studied with small (400 μm) and large (800 μm) minimum diameters as shown in figure 4.1. In the experiments, the channels were placed in a chamber and the pressure upstream of the orifices was maintained by a Biomedicus (Biomedicus TX50, Minneapolis, MN) centrifugal bypass pump at 120 mmHg (+/- 5 mmHg). Two 0.5 ml samples were taken at 0, 15, 30, 45 and 60 minutes for the TAT, PF4 and hemolysis assays. The TAT concentrations for all 8 channels after 60 minutes are shown in figure 4.2 and the differences between the channels are very clear. figure 4.2 shows that all the channels with small minimum diameter of 400 μm (odd–numbered channels) have approximately the same TAT concentration. However, the channels with a minimum diameter of 800 μm (even–numbered channels) show differences in TAT concentration between the geometries. In the numerical simulations, we used the same setup and flow conditions

to compare the computational results with the experimental results.

4.2.2 Numerical simulation results

Figure 4.3, 4.4 and 4.5 show the BDI_G, BDI_T and BDI_D values for all 8 channels, respectively. The platelet surface shear stress is divided by the threshold shear stress, $\tau_{thres} = 105\text{dyne/cm}^2$ and exposure time is divided by 1 sec, so the BDI values plotted are non–dimensional parameters. These plots show that the profiles of BDI_T and BDI_G are very different in comparison to the experiments. In both models, the non–dimensional BDI values for channels with larger internal diameter (even–numbered channels) are much less compared to channels that have the same geometry but smaller internal diameter (odd–numbered channels). However, the result of BDI_D model is very similar to the experimental results as shown in figure 4.5, except for channels 4 and 8. One possible reason for this deviation is that the current tracking algorithm cannot count the platelets that enter the recirculation zone in the experiments. All 40 platelets that were released at the inlet went through the domain without entering the recirculation zone. However, in Fallon's experiments [43], the platelets entered and stayed in the recirculation zone for a longer period of time compare to platelets that went through the channel. Since the shear stress in the recirculation zone is high, the BDI value of these platelets will strongly affect the average BDI value of the channel. This difference becomes significant for channels 4 and 8, since they have a sharp transition geometry with larger internal diameter and they have larger recirculation zones. Quantifying the contributions from this effect is an ongoing study.

In figure 4.5, the BDI_D value of channel 4 is higher than channel 2. These two channels have same dimensions except that channel 4 has a sharp 90 degree angle leading into the smaller internal diameter, and channel 2 has a much smoother transition to converge to the internal diameter. The sharper angle leads to higher

shear stresses, hence the larger damage in channel 4. Channel 8 and channel 6 have a similar situation except their geometry is diverging instead of converging.

On the other hand, all four channels with smaller internal diameter (odd–numbered channels) have similar and significantly larger BDI value than the channels with larger internal diameter (even–numbered channels). Based on these simulation results, it is evident that for the small channels, size is more important to blood damage. For channels with larger diameter, the geometry does play an important role. It was also found that large recirculation zones or sudden shape transitions will increase platelet activation.

4.3   *Discussion*

In this section we provide a thorough discussion of the BDI models and the results. The first part is the comparison and physical explanation of three different BDI models; the results and the limitations of the BDI_G (Giersiepen *et al.* [50]), BDI_D (Dumont *et al.* [40]) and BDI_T (Tambasco and Steinman [114]) models will be discussed here. The second part is the discussion and the suggestions about the numerical procedure that calculates the BDI value for a channel or a BMHV.

4.3.1   BDI models

In 1980's, Wurzinger and coworkers [123, 124, 125] conducted detailed experiments in blood to establish the relation between blood damage, shear stress and exposure time. By measuring the amount of cytoplasm enzyme released by platelets, they found that this relationship was not linear. Based on these observations, a mathematical correlation to calculate the blood damage level was developed by Giersiepen *et al.* [50] as shown by equation (3). It was argued that the platelet shear stress was more important than the exposure time, and high shear stress will dominate the result of this equation. In our simulations, the BDI_G of the platelet which experienced shear stress of 200 dynes/cm^2 is approximately 8000 times larger than platelet that experienced

a shear stress of 10 dynes/cm^2. This non–linear relation caused the significant differences between the BDI value of small channels (odd–numbered channels) and large channels (even–numbered channels). One reason for this large difference is that, the exponent constant in this model is based on experiments that have very different flow conditions. In their experiments [123, 124, 125], the platelet activation was investigated in a viscometer under constant shear stress. But in Fallon's experiments and in our simulations, the shear stresses vary significantly from the wall to the center of the channel. This difference can change the value of the exponent constant in the BDI model.

Bluestein and coworkers [15, 40, 96] have also conducted extensive research on shear-related platelet activation. They defined the platelet activation state (PAS) to model the blood damage under unsteady flow conditions. Grigioni et $al.$ [57] developed a mathematical model to evaluate the red blood cell damage. Based on this model, Nobili et $al.$ [96] calculated the platelet activation and compared their simulation results with the experimental results. In this model, a nonlinear least–square fitting method was applied to obtain the model parameters. The platelet shear stress history in the previous cycle was also counted in the PAS model by a damage accumulation model. Dumont et $al.$ [40] applied a similar model without the damage accumulation to compare the hemodynamic performance of two BMHVs. The model is given by equation (87), which is the BDI_D model. In the present simulation, this model gives the closest pattern compare to the simulation result.

The limitation of the BDI_D model, as pointed out by Tambasco and Steinman [114], is that, a platelet should only be activated when the platelet shear stress is higher than a threshold value. In the BDI_T model given by equation (88), this value is defined as the threshold shear stress and they used a value of 105 dynes/cm^2. The physical definition of the threshold shear stress is that, if platelet surface shear stress is lower than this value, it should not be activated and the activation of the platelets is

irrelevant with respect to the exposure time. The same threshold value is used in the current model. Based on the simulation results, as shown in figure 4.4, this value is too high and most shear stresses of platelets in large channels (even-numbered channels) were filtered out. Early experiments [20, 119, 120] have shown platelet secretion and aggregation when the shear stress was higher than 50 dynes/cm^2. Recent studies [62, 89, 94, 66] have demonstrated that at high level of shear stress (> 100 dynes/cm^2), platelets have aggregation and shedding of microparticles from their membrane. The appropriate threshold shear stress should lie between 12 dynes/cm^2 (the physiological shear stress) and 105 dynes/cm^2 (at which significant platelet activation is observed).

4.3.2 Numerical procedure

We want to emphasize here that one objective of this research is to choose an appropriate BDI model to optimize the design of BMHVs. It comes to our attention that all current models are Lagrangian–based models for platelets, and most of these models require the damage accumulation model to estimate the damage caused by the platelet shear stress history. This is correct for estimating the activation state of each platelet. However, it can cause problems when using these BDI models to evaluate the design of a channel or BMHV, since the initial conditions, such as the initial position, orientation and releasing time of the platelets, will affect the BDI value of the channel. For example, figure 4.6 shows a path line in a pressure driven channel flow. The BDI values from any existing BDI model will be different for platelets that are released at points A, B, C and D. Moreover, for the BDI models with damage accumulation model, the shear stress distribution from point C to point D is always more important than the distribution from point A to point B. In another words, the downstream shear stress distribution will always be more important than upstream distribution in these BDI models. However, the BDI value of a channel should only depend on the channel geometry and flow conditions, such as pressure gradient, and

106

it should NOT depend on the initial condition of the released tracking particles.

The presence of the recirculation zone makes the situation even more complex. If the platelets are only released at the inlet, these particles will not enter the recirculation zone (assuming no recirculation zone at the inlet of the fluid domain). Since the shear stress in the recirculation zone is high, and the platelets trapped in the zone experience a longer exposure time, this part of the blood damage is expected to be very important for the BDI calculation.

One solution to fix these problems is to calculate the space averaged shear stress of the channel. However, the amount of the blood damage should also depend on the number of platelets that pass through this region. Here we propose a universal approach: The platelets will be released uniformly in the entire fluid domain to make sure that the recirculation zones are included in the BDI calculation. A BDI model without the damage accumulation model will be applied. The BDI value of every platelet will be weighted by the local platelet concentration at the initial position, since in the whole blood flow, the platelets are pushed toward the wall [1, 130, 131]. In a given amount of time (1–2 cardiac cycles), the BDI value of the channel with certain pressure gradient should increase, similar to the plot shown in figure 4.7. Channel $c1$ which has a higher pressure gradient should have a higher BDI value compare to channel $c2$ which has same geometry but a lower pressure gradient. This numerical procedure can be used to assess the blood damage in BMHV hinges under different flow conditions (pressure gradient, unsteady flow, etc).

1.5 mm

Channel **1**
400 μm ID
800 μm OD

Channel **2**
800 μm ID
1200 μm OD

1.5 mm

Channel **3**
400 μm ID
800 μm OD

Channel **4**
800 μm ID
1200 μm OD

1.5 mm

Channel **5**
400 μm ID
800 μm OD

Channel **6**
800 μm ID
1200 μm OD

1.5 mm

Channel **7**
400 μm ID
800 μm OD

Channel **8**
800 μm ID
1200 μm OD
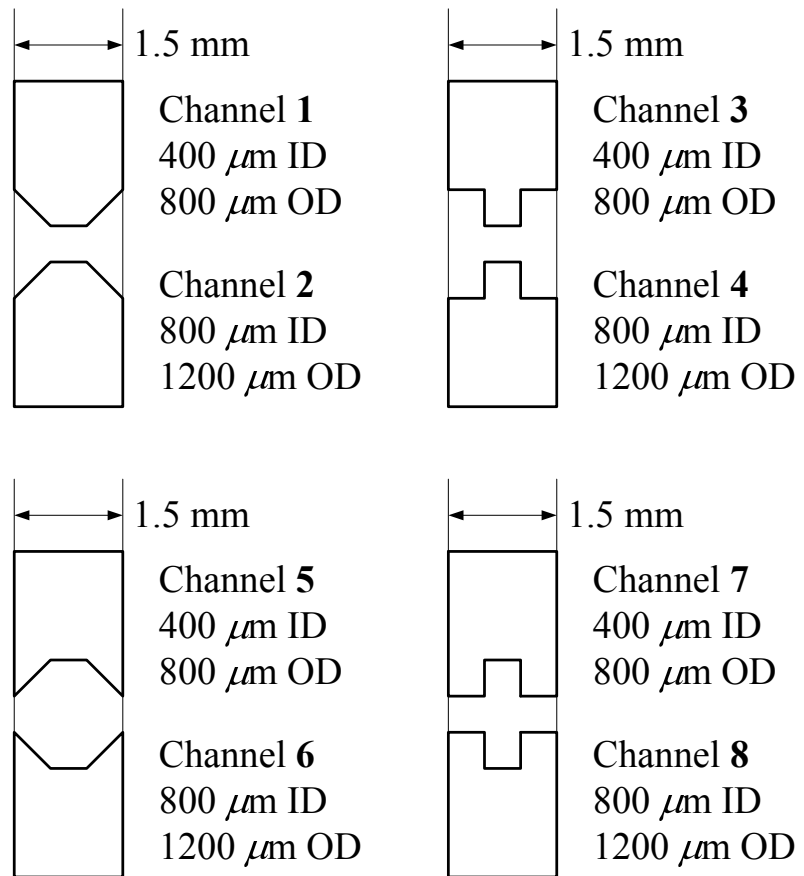
Figure 4.1: Channel diagrams.
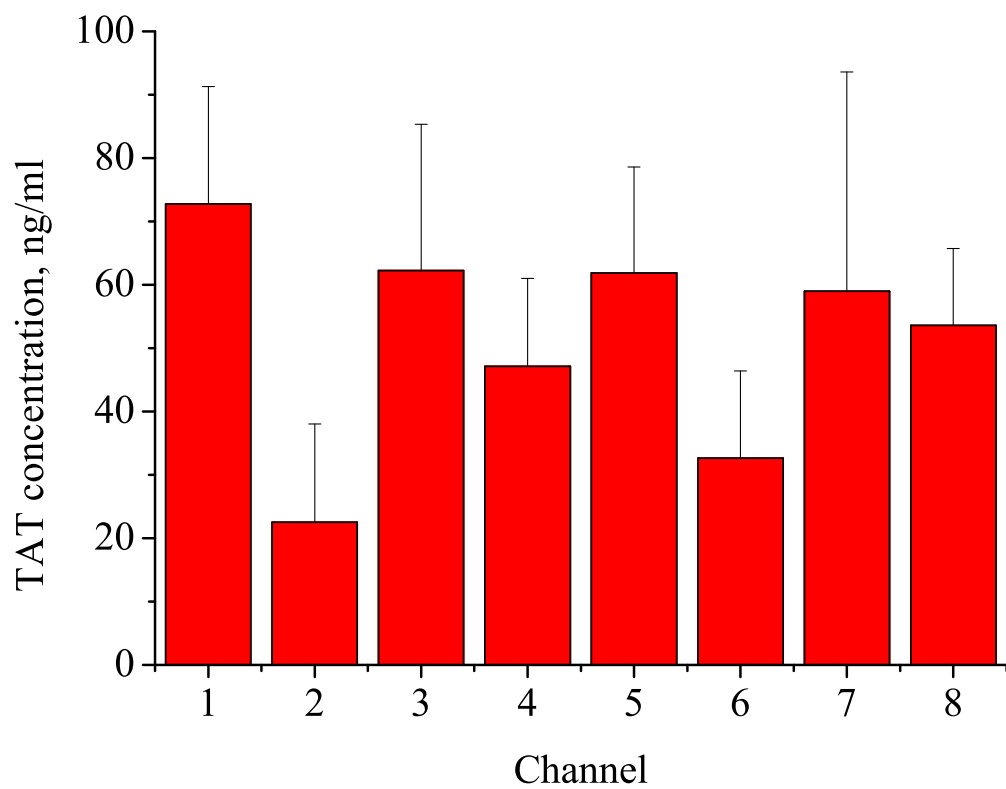
Figure 4.2: Fallon's experiment results of TAT concentration for all the channels at 60 minutes. (From Fallon [43])
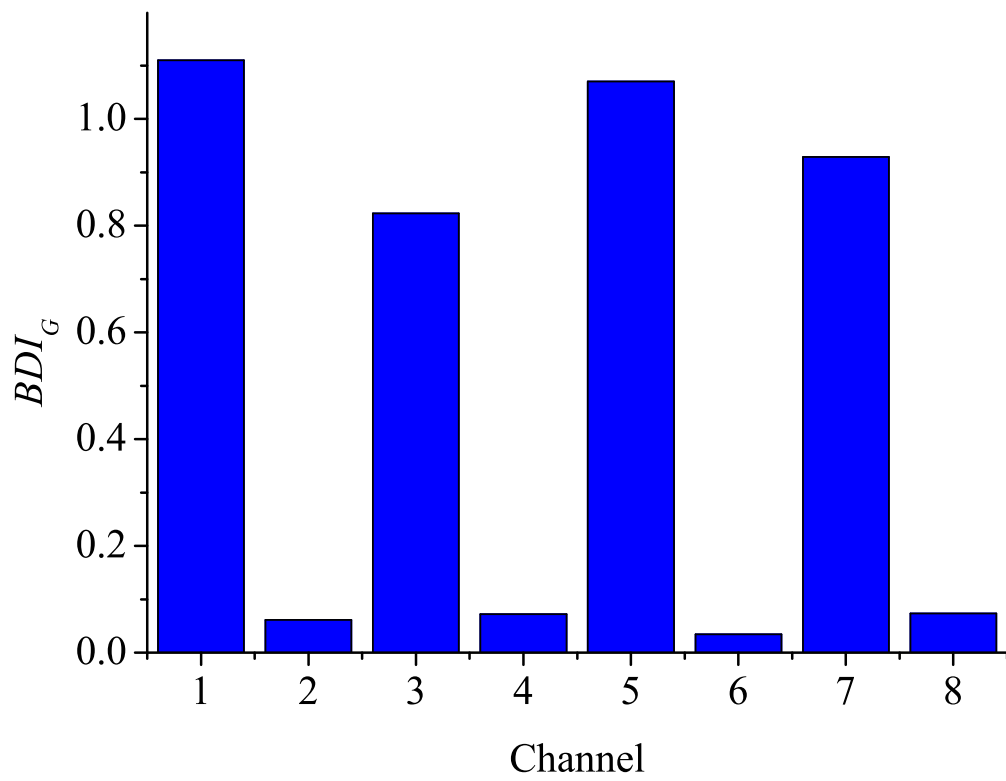
Figure 4.3: BDI_G for all 8 channels, LBM-EBF simulation results.
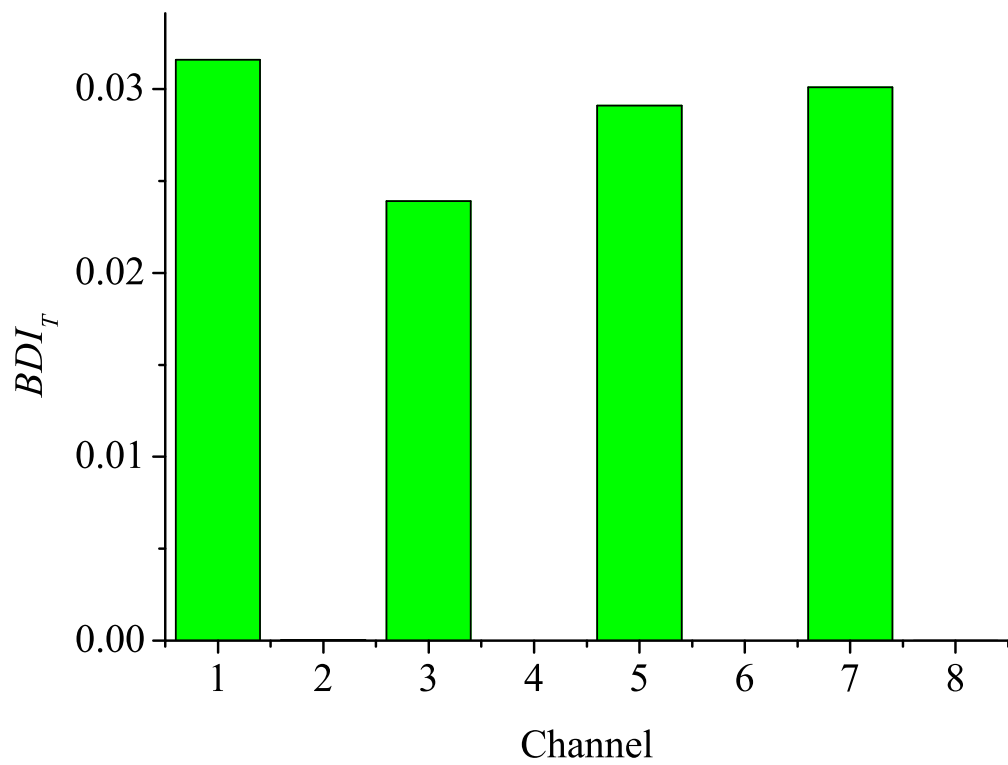
Figure 4.4: BDI_T for all 8 channels, LBM-EBF simulation results.
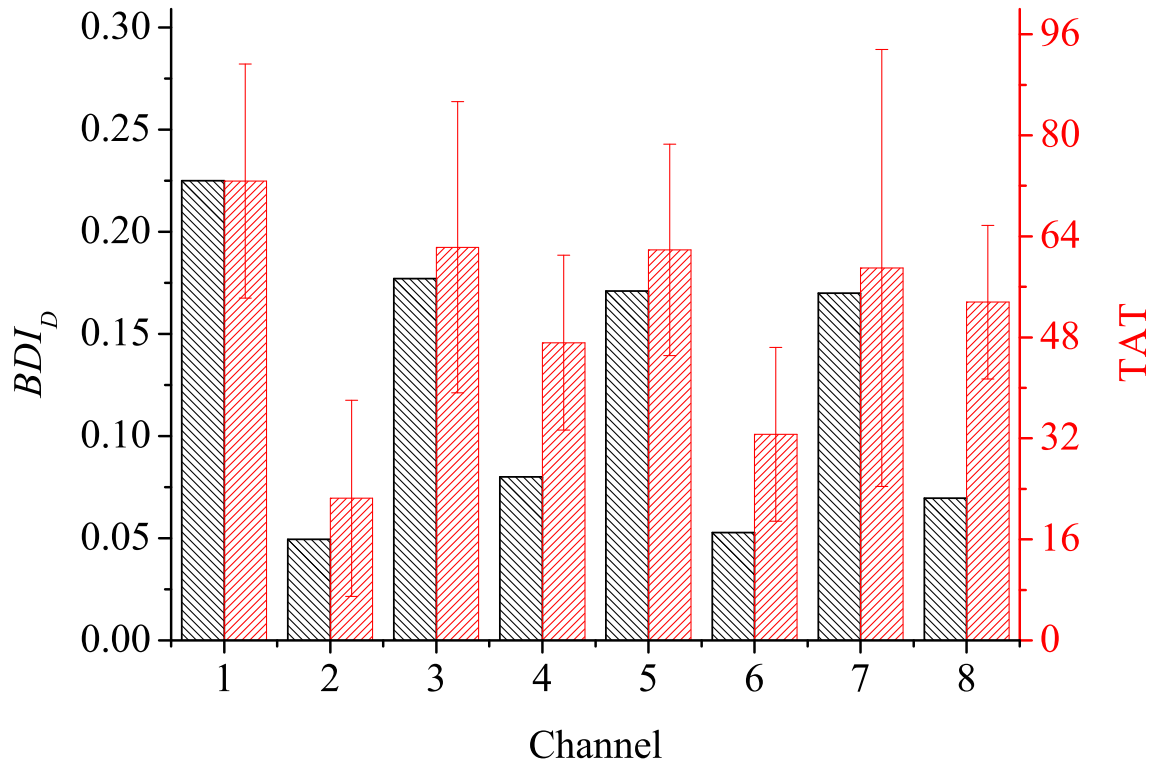
Figure 4.5: BDI_D for all 8 channels, the left y axis is for the black blocks which are the LBM-EBF simulation results and the right y axis is for the red blocks which are the TAT concentration from Fallon's experiment as shown in figure 4.2.
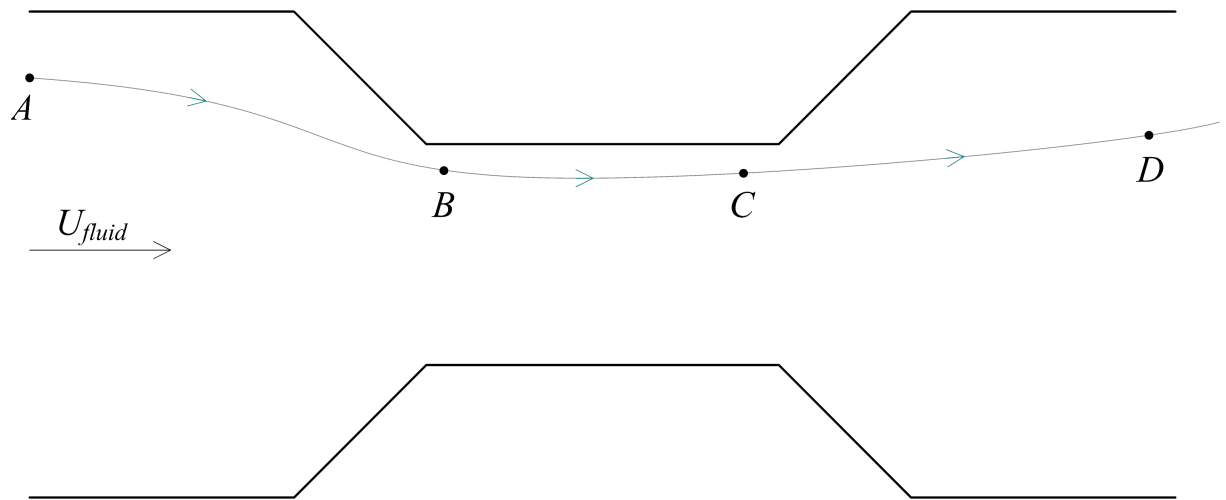
Figure 4.6: A path line in a pressure driven channel flow.
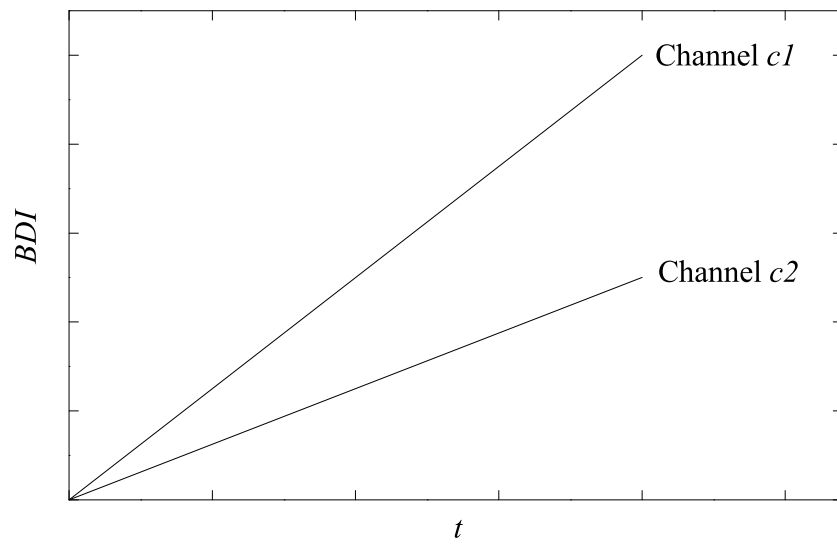
Figure 4.7: Example of the BDI values for two different channel flows.

CHAPTER V

CONCLUSIONS AND FUTURE RECOMMENDATIONS

5.1   Conclusions

In this research, a 3D numerical method is developed to simulate the microstructure and the rheological properties of flexible particle suspensions. Fundamental understanding of these flows is necessary for a full adhesion model that will be useful in engineering applications. The investigation into flows having a large number of deformable particles has shown the importance of particle deformation on the rheology of suspensions. The methodology developed here may be extended to more complex particle geometries and flow conditions. Thus, this research fits into the greater objective of prediction and optimization in engineering and clinical applications. The versatility of the coupled LBM–EBF method makes it attractive to use for investigating a wide range of applications.

We have presented the lattice–Boltzmann with external boundary force method for fluid–solid interaction problems. The novel application to the lattice Boltzmann method provides an efficient and more stable computational tool compared to the conventional LBM with SBB, particularly for large number of deformable particles suspended in viscous flow. By coupling this with the lattice–spring model, one can easily re–mesh the solid for different geometries. We can also prescribe the motion of the deformable particle. The operations in LBM with EBF are local; it can be easily programmed for parallel machines. This new method takes into account both long and short range hydrodynamic interactions and contact forces. The method has been validated by comparing the 3D computational results with experimental results and theoretical solutions. With this method, the concentration of suspensions can range

114

from dilute to concentrated volume fraction, deformable particles may have different density than the fluid and each particle can have different elastic properties with no additional demand on computational time.

The simulations seem to slightly over predict the shear viscosity in the dilute regime as compared to Blakeney's data, as shown in figure 2.17. This could be due to the unbounded periodic shear layer used in the simulations as compared with the wall–bounded experimental results. This effect may result in a small discrepancy in the magnitude of relative viscosity in the dilute regime. However, in the case of higher volume fraction suspension flow, considered in figure 2.18, the magnitude of relative viscosity is much higher, masking the small deviations between the experimental and computational results.

The flexible fiber suspension model proposed by [121] is used to simulate suspensions of non-Brownian fibers in simple shear flow. The results agree well with data from experimental and theoretical studies. It is shown that the fiber stiffness has strong impact on suspension rheology. The relative viscosity is well predicted by a curve–fitting relation. It can be used for calculating the relative viscosity of flexible fiber suspension from the result of rigid fiber suspension. Also, the effect of fiber stiffness on the first normal stress difference based on the fiber orientation distribution and orbit constant is explained. The influence of fiber stiffness on the fiber orientation distribution and orbit constant is a major contributor to the variation in rheological properties.

In chapter §4 the effect of 3D channel geometry on the shear–induced platelet activation and aggregation is modeled by using LBM–EBF method. Platelets can have different shapes, healthy platelets are ellipsoidal disk shape and activated platelets have rounded shape with irregular tassels, so the unsteady shear stress sensed by platelets is not the same as a spherical particle. Therefore, it is imperative to develop a particle–level numerical method with two-way coupling between fluid–solid phases.

The BDI value computed for different channels are compared to previously published experimental data [43]. Comparison of our simulations with Fallon's experiments shows a similar pattern and shows that Dumont's BDI model [40] is more appropriate for blood damage investigation. Furthermore, the simulations come to the same conclusion as Fallon's experiments [43], that channels with sharp contraction–expansion will have larger recirculation areas causing elevated BDI values.

The objective is to understand the fundamental principle regarding the impact of different design parameters on hinge flow fields. A new numerical procedure is proposed in this study to include the recirculation zones in the BDI calculation and to eliminate the effects of initial conditions. By investigating the effect of hinge area geometry on BDI value, we intend to use this multiscale computational method to optimize the design of BMHVs.

5.2   Future recommendations

The coupled lattice–Boltzmann external boundary force method presented in this work has been shown to be successful in simulating thousands of suspending flexible fibers, RBCs and platelets and producing continuum–scale physics. A number of physiologic problems and engineering applications are within the scope of this method. While most of the simulations presented in this work are performed in simple shear flow for comparison with experiments, extensions may be made to more complex particle geometries and flow conditions. The ease of creating new shapes within the lattice–spring model allows for the simulation of particles and flows with irregular boundaries.

Recent studies have shown that the lubrication force is not sufficiently strong to prevent fiber–fiber contacts. Contact force becomes an important parameter for fiber suspension simulations. Contact force models are readily available and can be easily implemented, since all needed information and function is presented in the

simulations. The effect of contact force on suspension microstructure and rheology could be an interesting subject, especially in concentrated regimes.

Although the EBF method is used in conjunction with the lattice–spring model for deformable particles in this application, it is a general coupling method for fluid–solid interaction simulations. Coupling the lattice–Boltzmann method with the finite–element method by using EBF is currently under development. The current code is written based on the OpenMP interface. To further improve the efficiency and performance and to run simulations at large cluster, algorithm optimization and full parallelization based on the MPI interface is necessary.

REFERENCES

[1] AARTS, P. A., V. D. BROEK, S. A., PRINS, G. W., KUIKEN, G. D., SIXMA, J. J., and HEETHAAR, R. M., "Blood platelets are concentrated near the wall and red blood cells, in the center in flowing blood," *Arteriosclerosis, Thrombosis, and Vascular Biology*, vol. 8, p. 819, 1988.

[2] AIDUN, C. K. and CLAUSEN, J. R., "Lattice–boltzmann method for complex flows," *Annual Review of Fluid Mechanics*, vol. 42, pp. 439–472, 2010.

[3] AIDUN, C. K. and DING, E., "A universal scale for cluster size distribution of solid spheres and red blood cells suspended in pressure–driven flow," in *59th Annual Meeting*, Div. Fluid Dynamics, American Physical Society, nov 2006.

[4] AIDUN, C. K. and LU, Y., "Lattice-boltzmann simulation of solid particles suspended in fluid," *Journal of statistical physics*, vol. 81, pp. 49–61, 1995.

[5] AIDUN, C. K., LU, Y., and DING, E., "Direct analysis of particulate suspensions with inertia using the discrete boltzmann equation," *Journal of Fluid Mechanics*, vol. 373, p. 287, 1998.

[6] ALEXEEV, A., VERBERG, R., and BALAZS, A. C., "Modeling the motion of microcapsules on compliant polymeric surfaces," *Macromolecules*, vol. 38, p. 10244, 2005.

[7] ANCZUROWSKI, E. and MASON, S. G., "The kinetics of following dispersions," *Journal of Colloid and Interface Science*, vol. 23, p. 533, 1967.

[8] ARBABI, S. and SAHIMI, M., "Test of universality for three-dimensional models of mechanical breakdown in disordered solids," *Physical Review B*, vol. 41, p. 772, 1990.

[9] BATCHELOR, G. K., "Slender–body theory for particles of arbitrary cross–section in stokes flow," *Journal of Fluid Mechanics*, vol. 44, p. 419, 1970.

[10] BATCHELOR, G. K., "The stress generated in a non–dilute suspensions of elongated particles by pure straining motion," *Journal of Fluid Mechanics*, vol. 46, p. 813, 1971.

[11] BERRY, D. H. and RUSSEL, W. B., "The rheology of dilute suspensions of slender rods in weak flows," *Journal of Fluid Mechanics*, vol. 180, pp. 475–494, 1987.

[12] BIBBO, M., *Rheology of semi-concentrated fiber suspensions.* PhD thesis, Massachusetts Institute of Technology, 1987.

[13] BIBBO., M., DINH, S., and ARMSTRONG, R., "Shear flow properties of semi-concentrated fibre suspensions," *Journal of Rheology*, vol. 29, pp. 905–929, 1985.

[14] BLAKENEY, W., "The viscosity of suspensions of straight, rigid rods," *Journal of Colloid and Interface Science*, vol. 22, p. 324, 1966.

[15] BLUESTEIN, D., "Research approaches for studying flow induced thromboem–bolic complications in blood recirculating devices," *Expert Review of Medical Devices*, vol. 1, pp. 65–80, 2004.

[16] BOUZIDI, M., FIRDAOUSS, M., and LALLEMAND, P., "Momentum transfer of a boltzmann–lattice fluid with boundaries," *physics of fluids*, vol. 13, p. 3452, 2001.

[17] BRENNER, H., "Rheology of a dilute suspension of axisymmetric brownian particles," *International Journal of Multiphase Flow*, vol. 1, pp. 195–341, 1974.

[18] BRETHERTON, F. P., "Slow motion round a cylinder in a simple shear," *Journal of Fluid Mechanics*, vol. 12, p. 591, 1962.

[19] BROOKS, D. E., GOODWIN, J. W., and SEAMAN, G. V., "Interactions among erythrocytes under shear," *Journal of Applied Physiology*, vol. 28, pp. 172–177, 1970.

[20] BROWN, C. H., LEVERETT, L. B., LEWIS, C. W., ALFREY, C. P., and HELLUMS, J. D., "Morphological, biochemical and functional changes in human platelets subjected to shear stress," *Journal of Laboratory and Clinical Medicine*, vol. 86, p. 462, 1975.

[21] BUICK, J. M. and GREATED, C. A., "Gravity in a lattice boltzmann model," *Physical Review E*, vol. 61, p. 5307, 2000.

[22] BURGERS, J., *On the motion of small particles of elongated form suspended in a viscous liquid, Second Report on Viscosity and Plasticity*. Kon. Ned. Akad. Wet., Verhand, North-Holland, Amsterdam, 1938.

[23] BUXTON, G. A., CARE, C. M., and CLEAVER, D. J., "A lattice spring model of heterogeneous materials with plasticity," *Modelling and Simulation in Materials Science and Engineering*, vol. 9, pp. 485–497, 2001.

[24] BUXTON, G. A., VERBERG, R., JASNOW, D., and BALAZS, A. C., "Newtonian fluid meets an elastic solid: Coupling lattice boltzmann and lattice - spring models," *Physical Review E*, vol. 71, p. 056707, 2005.

[25] CARTER, L. F., *A study of the rheology of suspensions of rod–shaped particles in a Navier–Stokes liquid*. PhD thesis, University of Michigan, 1967.

[26] CARTER, L. F. and GODDARD, J. D., "A rheology study of glass fibers in a newtonian fluid," *NASA Report*, vol. N67-30073, 1967.

[27] CHA, W. and BEISSINGER, R. L., "Augmented mass transport of macro-molecules in sheared suspensions to surfaces b. bovine serum albumin," *J. of Colloid and Interface Sci.*, vol. 178, p. 1, 1996.

[28] CHAPMAN, S., "On the law of distribution of molecular velocities, and on the theory of viscosity and thermal conduction, in a non–uniform simple monatomic gas," *Philosophical Transactions of the Royal Society*, vol. 216, p. 279, 1916.

[29] CHEN, H., CHEN, S., and MATTHAEUS, W. H., "Recovery of the navier-stokes equations using a lattice-gas boltzmann method," *Physical review A*, vol. 45, p. 5339, 1992.

[30] CHUN, B. and LADD, A. J. C., "Interpolated boundary condition for lattice boltzmann simulations of flows in narrow gaps," *Physical review E*, vol. 75, p. 066705, 2007.

[31] CLAEYS, I. L. and BRADY, J. F., "Suspensions of prolate spheroids in stokes flow. part 1. dynamics of a finite number of particles in an unbounded fluid," *Journal of Fluid Mechanics*, vol. 251, p. 411, 1993.

[32] COX, R. G., "The motion of long slender bodies in a viscous fluid. 2. shear flow," *Journal of Fluid Mechanics*, vol. 45, pp. 625–657, 1971.

[33] D. R. MIKULENCAK, J. F. M., "Stationary shear flow around fixed and free bodies at finite reynolds number," *Journal of Fluid Mechanics*, vol. 520, p. 215, 2004.

[34] DING, E. and AIDUN, C. K., "The dynamics and scaling law for particles suspened in shear flow with inertia," *Journal of Fluid Mechanics*, vol. 423, p. 317, 2000.

[35] DING, E. and AIDUN, C. K., "Extension of the lattice–boltzmann method for direct simulation of suspended particles near contact," *Journal of Statistical Physics*, vol. 112, pp. 685–708, 2003.

[36] DINH, S. and ARMSTRONG, R., "A rheological equation of state for semi–concentrated fiber suspensions," *Journal of Rheology*, vol. 28, p. 207, 1984.

[37] DOI, M., "Molecular dynamics and rheological properties of concentrated solutions of rodlike polymers in isotropic and liquid crystalline phases," *Journal of Polymer Science: Polymer Physics Edition*, vol. 19, pp. 229–243, 1981.

[38] DOI, M. and EDWARDS, S. F., "Dynamics of concentrated polymer systems i; brownian motion in equilibrim state," *Journal of the Chemical Society, Faraday Transactions II*, vol. 74, p. 1789, 1978.

[39] DOI, M. and EDWARDS, S. F., "Dynamics of concentrated polymer systems ii; molecular motion under flow," *Journal of the Chemical Society, Faraday Transactions II*, vol. 74, p. 1802, 1978.

[40] DUMONT, K., VIERENDEELS, J., KAMINSKY, R., NOOTEN, G. V., VER-DONCK, P., and BLUESTEIN, D., "Comparison of the hemodynamic and thrombogenic performance of two bileaflet mechanical heart valves using a cfd/fsi model," *Journal of Biomechanical Engineering*, vol. 129, pp. 558–565, 2007.

[41] DUPIN, M., HALLIDAY, I., CARE, C., ALBOUL, L., and MUNN, L., "Modeling the flow of dense suspensions of deformable particles in three dimensions," *Physical Review E*, vol. 75, p. 066707, 2007.

[42] ENSKOG, D., *Kinetische Theorie der Vorgäenge in mäessig verdüennten G.* PhD thesis, Uppsala, 1917.

[43] FALLON, A. M., *The Development of a Novel in vitro Flow System to Evaluate Platelet Activation and Procoagulant Potential Induced by Bileaflet Mechanical Heart Valve Leakage Jets.* PhD thesis, Georgia Institute of Technology, 2006.

[44] FENG, Z. and MICHAELIDES, E., "The immersed boundary - lattice boltzmann method for solving fluid - particles interaction problems," *Journal of Computational Physics*, vol. 195, p. 602, 2004.

[45] FOLGAR, F. and TUCKER, C. L., "Orientation behavior of fibers in concentrated suspensions," *Journal of reinforced plastic composite*, vol. 3, p. 98, 1984.

[46] FORGACS, O. L. and MASON, S. G., "Particle motions in sheared suspensions. 9. spin and deformation of thread-like particles," *Journal of Colloid and Interface Science*, vol. 14, p. 457, 1959.

[47] FUNG, Y., *Biomechanics: Mechanical Properties of Living Tissues.* Springer, 1993.

[48] GANANI, E. and POWELL, R. L., "Suspensions of rodlike particles: Literature review and data correlations," *Journal of Composite Materials*, vol. 19, pp. 194–215, 1985.

[49] GANANI, E. and POWELL, R. L., "Rheological properties of rodlike particles in a newtonian and a non–newtonian fluid," *Journal of Rheology*, vol. 30, pp. 995–1013, 1986.

[50] GIERSIEPEN, M., WURZINGER, L. J., OPITZ, R., and REUL, H., "Estimation of shear stress–related blood damage in heart valve prostheses – in vitro comparison of 25 aortic valves," *International Journal Of Artificial Organs*, vol. 13, pp. 300–306, 1990.

[51] GINZBURG, I. and D'HUMIERES, D., "Multireflection boundary conditions for lattice boltzmann models," *Physical Review E*, vol. 68, p. 066614, 2003.

[52] GOLDSMITH, H. L. and MASON, S. G., "The microrheology of dispersions," *Rheology*, vol. 4, pp. 85–201, 1967.

[53] GOLDSTEIN, D., HANDLER, R., and SIROVICH, L., "Modeling a no-slip flow boundary with an external force field," *Journal of Computational Physics*, vol. 105, pp. 354–366, 1993.

[54] GOTO, S., NAGAZONO, H., and KATO, H., "The flow behavior of fiber suspensions in newtonian fluids and polymer solutions. i: Mechanical properties," *Rheologica acta*, vol. 25, p. 119, 1986.

[55] GOTO, S., NAGAZONO, H., and KATO, H., "The flow behavior of fiber suspensions in newtonian fluids and polymer solutions. ii: Capillary flow," *Rheologica acta*, vol. 25, p. 246, 1986.

[56] GRAD, H., "Principles of the kinetic theory of gases," *Handbuch der Physik (Thermodynamics of Gases)*, vol. 12, p. 205, 1958.

[57] GRIGIONI, M., MORBIDUCCI, U., D'AVENIO, G., BENEDETTO, G. D., and GAUDIO, C. D., "Proposal for a new formulation of the power law mathematical model for blood trauma prediction," *Biomechanics and Modeling in Mechanobiology*, vol. 4, p. 249, 2005.

[58] GUO, Z., ZHENG, C., and SHI, B., "Discrete lattice effects on the forcing term in the lattice boltzmann method," *Physical Review E*, vol. 65, p. 046308, 2002.

[59] GUTH, E., "On the theory of the viscosity of suspensions of ellipsoidal particles," *Physical Review*, vol. 53, p. 926, 1938.

[60] HARKNESS, J. and WHITTINGTON, R. B., "Blood–plasma viscosity: an approximate temperature invariant arising from generalised concepts," *Biorheology*, vol. 6, pp. 169–187, 1970.

[61] HE, X., ZOU, Q., LUO, L. S., and DEMBO, M., "Analytic solutions and analysis on non–slip boundary condition for the lattice boltzmann bgk model," *Journal of Statistical Physics*, vol. 87, p. 115, 1997.

[62] HELLUMS, J. D., "Whitaker lecture: Biorheology in thrombosis research," *Annals of Biomedical Engineering*, vol. 22, p. 445, 1994.

[63] HINCH, E. J. and LEAL, L. G., "The effect of brownian motion on the rheological properties of a suspension of non-spherical particles," *Journal of Fluid Mechanics*, vol. 52, p. 683, 1972.

[64] HINCH, E. J. and LEAL, L. G., "Time–dependent shear flows of a suspension of particles with weak brownian rotations," *Journal of Fluid Mechanics*, vol. 57, pp. 753–767, 1973.

[65] HINCH, E. J. and LEAL, L. G., "Constitutive equations in a suspension mechanics. part 2. approximate forms for a suspension of rigid particles affected by brownian rotations," *Journal of Fluid Mechanics*, vol. 76, pp. 187–208, 1976.

[66] HOLME, P. A., ORVIM, U., HAMERS, M. J. A. G., SOLUM, N. O., BROSSTAD, F. R., BARSTAD, R. M., and SAKARIASSEN, K. S., "Shear–induced platelet activation and platelet microparticle formation at blood flow conditions as in arteries with a severe stenosis," *Arteriosclerosis, Thrombosis, and Vascular Biology*, vol. 17, pp. 646–653, 1997.

[67] HOU, S., ZOU, Q., CHEN, S., DOOLEN, G., and COGLEY, A. C., "Simulation of cavity flow by lattice boltzmann method," *Journal of Computational Physics*, vol. 118, p. 329, 1995.

[68] HUR, D. U., *Flow of semidilute glass fibre suspensions in tubular entry flows*. PhD thesis, University of Melbourne, 1987.

[69] JEFFERY, G. B., "The motion of ellipsoidal particles immersed in a viscous fluid," *Proceedings of the Royal Society of London. Series A*, vol. 102, p. 161, 1922.

[70] JOUNG, C. G., PHAN-THIEN, N., and FAN, X. J., "Direct simulation of flexible fibers," *Journal of Non–Newtonian Fluid Mechanics*, vol. 99, p. 1, 2001.

[71] KESHTKAR, M., HEUZEY, M. C., and CARREAU, P. J., "Rheological behavior of fiber–filled model suspensions: Effect of fiber flexibility," *Journal of Rheology*, vol. 53, p. 631, 2009.

[72] KIM, D. and BEISSINGER, R. L., "Augmented mass transport of macro-molecules in sheared suspensions to surfaces," *Journal of Colloid and Interface Science*, vol. 159, pp. 9–20, 1993.

[73] KITANO, T. and KATAOKA, T., "The rheology of suspensions of vinylon fibers in polymer liquids. i. suspensions in silicone oil," *Rheologica Acta*, vol. 20, pp. 390–402, 1981.

[74] KOCH, D. L., "A model for orientational diffusion in fiber suspensions," *Physics of Fluids*, vol. 7, p. 2086, 1995.

[75] KOCH, D. L. and SHAQFEH, E. S. G., "The average rotation rate of a fiber in the linear flow of a semidilute suspension," *Physics of Fluids A: Fluid Dynamics*, vol. 2, pp. 2093–2102, 1990.

[76] KROLL, M. H., HELLUMS, J. D., McINTIRE, L. V., SCHAFER, A. I., and MOAKE, J. L., "Platelets and shear stress," *Blood*, vol. 88, pp. 1525–1541, 1996.

[77] KUHN, W. and KUHN, H., "Die abhangkeit der viskositat vom stromungsge-falle bei hochverdam suspensionen und losungen," *Helv. Chim. Acta*, vol. 28, pp. 97C–127, 1945.

[78] LADD, A. J. C., "Numerical simulations of particulate suspensions via a discretized boltzmann equation. part 1. theoretical fundation," *Journal of Fluid Mechanics*, vol. 271, p. 285, 1994.

[79] LADD, A. J. C. and VERBERG, R., "Lattice-boltzmann simulation of particle-fluid suspensions," *Journal of Statistical Physics*, vol. 104, p. 1191, 2001.

[80] LARSON, R. G., *The Structure and Rheology of Complex Fluids*. Oxford University Press: New York, 1999.

[81] LEES, A. W. and EDWARDS, S. F., "The computer study of transport processes under extreme conditions," *Journal of Physics C*, vol. 5, p. 1921, 1972.

[82] LIBOFF., R., *Kinetic Theory: Classical, Quantum, and Relativistic Descriptions (3rd Edition)*. Springer, 2003.

[83] LINDSTROM, S. B. and UESAKA, T., "Simulation of semidilute suspensions of non–brownian fibers in shear flow," *Journal of Chemical Physics*, vol. 128, p. 024901, 2008.

[84] MACKAPLOW, M. B. and SHAQFEH, E. S. G., "A numerical study of the rheological properties of suspensions of rigid, non–brownian fibres," *Journal of Fluid Mechanics*, vol. 329, p. 155, 1996.

[85] MACMECCAN, R. M., CLAUSEN, J. R., NEITZEL, G. P., and AIDUN, C. K., "Simulating deformable particle suspensions using a coupled lattice-boltzmann and finite-element method," *Journal of Fluid Mechanics*, vol. 618, p. 13, 2009.

[86] MARTYS, N. S., SHAN, X., and CHEN, H., "Evaluation of the external force term in the discrete boltzmann equation," *Physical Review E*, vol. 58, p. 6855, 1998.

[87] MASON, S. G., "Fiber motions and flocculation," *TAPPI*, vol. 37, pp. 494–501, 1954.

[88] MCNAMARA, G. R. and ZANETTI, G., "Use of the boltzmann equation to simulate lattice-gas automata," *Physical review letters*, vol. 61, p. 2332, 1988.

[89] MERINO, A., COHEN, M., BADIMON, J. J., FUSTER, V., and BADIMON, L., "Synergistic action of severe wall injury and shear forces on thrombus formation in arterial stenosis: Definition of a thrombotic shear rate threshold," *Journal of the American College of Cardiology*, vol. 24, p. 1091, 1994.

[90] MERRILL, E. W., COKELET, G. C., BRITTEN, A., and WELLS, R. E., "Non-newtonian rheology of human blood – effect of fibrinogen deduced by "subtraction"," *Circulation Research*, vol. 13, pp. 48–55, 1963.

[91] MEYER, R. and WAHREN, D., "On the elastic properties of three-dimensional fibre networks," *Svensk Papperstidning*, vol. 67, pp. 432–436, 1964.

[92] MILLIKEN, W. J., GOTTLIEB, M., GRAHAM, A. L., MONDY, L. A., and POWELL, R. L., "The viscosity–volume fraction relation for suspensions of rod-like particles by falling–ball rheometry," *Journal of Fluid Mechanics*, vol. 202, pp. 217–232, 1989.

[93] MIYAMURA, A., IWASAKI, S., and ISHII, T., "Experimental wall correction factors of single solid spheres in triangular and square cylinders, and parallel plates," *International Journal of Multiphase Flow*, vol. 7, p. 41, 1981.

[94] MIYAZAKI, Y., NOMURA, S., MIYAKE, T., KAGAWA, H., KITADA, C., TANIGUCHI, H., KOMIYAMA, Y., FUJIMURA, Y., IKEDA, Y., and FUKUHARA, S., "High shear stress can initiate both platelet aggregation and shedding of procoagulant containing microparticles," *Blood*, vol. 88, p. 3456, 1996.

[95] NAWAB, M. A. and MASON, S. G., "Viscosity of dilute suspensions of thread–like particles," *Journal of Physical Chemistry*, vol. 62, pp. 1248–1253, 1958.

[96] NOBILI, M., SHERIFF, J. F., MORBIDUCCI, U., REDAELLI, A., JESTY, J., and BLUESTEIN, D., "Platelet activation due to hemodynamic shear stresses: damage accumulation model and comparison to in vitro measurements," *ASAIO Journal*, vol. 54, pp. 64–72, 2008.

[97] PESKIN, C. S., "The immersed boundary method," *Acta Numerica*, vol. 11, p. 479, 2002.

[98] PETRICH, M. P., KOCH, D. L., and COHEN, C., "An experimental determination of the stress–microstructure relationship in semi–concentrated fiber suspensions," *Journal of Non–Newtonian Fluid Mechanics*, vol. 95, p. 101, 2000.

[99] POE, G. G. and ACRIVOS, A., "Closed-streamline flows past rotating single cylinders and spheres: inertia effects," *Journal of Fluid Mechanics*, vol. 72, p. 605, 1975.

[100] QI, D., "A new method for direct simulations of flexible filament suspensions in non-zero reynolds number flows," *International Journal for Numerical Methods in Fluids*, vol. 54, p. 103, 2006.

[101] RAHNAMA, M., KOCH, D. L., and SHAQFEH, E. S. G., "The effect of hydrodynamic interactions on the orientation distribution in a fiber suspension subject to simple shear flow," *Physics of Fluids*, vol. 7, p. 487, 1995.

[102] REZAK, S., *Analysis of Flexible Fiber Suspensions Using the Lattice Boltzmann method*. PhD thesis, Georgia Institute of Technology, 2008.

[103] ROSS, R. F. and KLINGENBERG, D. J., "Dynamic simulation of flexible fibers composed of linked rigid bodies," *Journal of Chemical Physics*, vol. 106, p. 2949, 1997.

[104] Schmid, C. F., Switzer, L. H., and Klingenberg, D. J., "Simulation of fiber flocculation: Effects of fiber properties and interfiber friction," *Journal of Rheology*, vol. 44, p. 781, 2000.

[105] Schwartz, L. M., Feng, S., Thorpe, M. F., and Sen, P. N., "Behavior of depleted elastic networks: Comparison of effective-medium and numerical calculations," *Physical Review B*, vol. 32, p. 4607, 1985.

[106] Sepehr, M., Carreau, P. J., Moan, M., and Ausias, G., "Rheological properties of short fiber model suspensions," *Journal of Rheology*, vol. 48, pp. 1023–1048, 2004.

[107] Shaqfeh, E. S. G. and Fredrickson, G., "The hydrodynamic stress in a suspension of rods," *Physics of Fluids A*, vol. 2, pp. 7–24, 1990.

[108] Shin, S., Ku, Y., Park, M. S., and Suh, J. S., "Measurement of red cell deformability and whole blood viscosity using laser-diffraction slit rheometer," *Korea-Australia Rheology Journal*, vol. 16, pp. 85–90, 2004.

[109] Sierou, A. and Brady, J. F., "Rheology and microstructure in concentrated noncolloidal suspensions," *Journal of Rheology*, vol. 46, pp. 1031–1056, 2002.

[110] Simha, R., "The infuence of brownian movement on the viscosity of solutions," *Journal of Physical Chemistry*, vol. 44, pp. 25–34, 1940.

[111] Stover, C. A., Koch, D. L., and Cohen, C., "Observations of fiber orientation in simple shear flow of semi–dilute suspensions," *Journal of Fluid Mechanics*, vol. 238, p. 277, 1992.

[112] Sundararajakumar, R. R. and Koch, D. L., "Structure and properties of sheared fiber suspensions with mechanical contacts," *Journal of Non–Newtonian Fluid Mechanics*, vol. 73, p. 205, 1998.

[113] Switzer, L. H. and Klingenberg, D. J., "Rheology of sheared flexible fiber suspensions via fiber-level simulations," *Journal Of Rheology*, vol. 47, pp. 759–778, 2003.

[114] Tambasco, M. and Steinman, D. A., "Path–dependent hemodynamics of the stenosed carotid bifurcation," *Annals of Biomedical Engineering*, vol. 31, pp. 1054–1065, 2003.

[115] Trevelyan, B. G. and Mason, S. G., "Particle motions in sheared suspensions. 1. rotations," *Journal of Colloid Science*, vol. 6, p. 354, 1951.

[116] Tsukada, K., Sekizuka, E., and Oshio, C., "Direct measurement of erythrocyte deformability in diabetes mellitus with transparent microchannel capillary model and high-speed video camera system," *Microvascular Reasearch*, vol. 61, pp. 231–239, 2001.

[117] WAGNER, A. and PAGONABARRAGA, I., "Lees-edwards boundary conditions for lattice boltzmann," *Journal of Statistical Physics*, vol. 107, p. 521, 2002.

[118] WAUGH, R. and EVANS, E. A., "Thermoelasticity of red blood cell membrane," *Biophysical Journal*, vol. 26, pp. 115–132, 1979.

[119] WEISS, H. J., BAUMGARTNER, H. R., TSCHOPP, T. B., TURITTO, V. T., and COHEN, D., "Correction by factor viii of the impaired platelet adhesion to subendothelium in von willebrand's disease," *Blood*, vol. 51, p. 267, 1978.

[120] WEISS, H. J., TURITTO, V. T., and BAUMGARTNER, H. R., "Effect of shear rate on platelet interaction with subendothelium in citrated and native blood. shear rate–dependent decrease of adhesion in von willebrand disease and the bernard soulier syndrome," *Journal of Laboratory and Clinical Medicine*, vol. 92, p. 750, 1978.

[121] WU, J. and AIDUN, C. K., "A method for direct simulation of flexible fiber suspensions using lattice–boltzmann equation with external boundary force," *International Journal of Multiphase Flow*, vol. 36, pp. 202–209, 2010.

[122] WU, J. and AIDUN, C. K., "Simulating 3d deformable particle suspensions using lattice boltzmann method with discrete external boundary force," *International Journal for Numerical Method in Fluids*, vol. 62, pp. 765–783, 2010.

[123] WURZINGER, L. J., OPITZ, R., BLASBERG, P., and SCHMID-SCHONBEIN, H., "Platelet and coagulation parameters following millisecond exposure to laminar shear shress," *Thrombosis and Haemostasis*, vol. 54, pp. 381–386, 1985.

[124] WURZINGER, L. J., OPITZ, R., and ECKSTEIN, H., "Mechanical blood trauma: An overview," *Angeiologie*, vol. 38, pp. 81–97, 1986.

[125] WURZINGER, L. J., OPITZ, R., WOLF, M., and SCHMID-SCHONBEIN, H., "Ultrastructural investigations on the question of mechanical activation of blood platelets," *Annals of Hematology*, vol. 54, pp. 97–107, 1987.

[126] YAMAMOTO, S. and MATSUOKA, T., "A method for dynamic simulation of rigid and flexible fibers in a flow field," *Journal of Chemical Physics*, vol. 98, p. 644, 1992.

[127] YAMANE, Y., KANEDA, Y., and DOI, M., "Numerical simulation of semi-dilute suspensions of rodlike particles in shear flow," *Journal of Non–Newtonian Fluid Mechanics*, vol. 54, p. 405, 1994.

[128] YU, D., MEI, R., LUO, L., and SHYY, W., "Viscous flow computations with the method of lattice boltzmann euqation," *Progress in Aerospace Sciences*, vol. 39, p. 329, 2003.

[129] Zettner, C. M. and Yoda, M., "The circular cylinder in simple shear at moderate reynolds numbers: An experimental study," *Experiments in Fluids*, vol. 30, p. 346, 2001.

[130] Zhao, R., Kameneva, M. V., and Antaki, J. F., "Investigation of platelet margination phenomena at elevated shear stress," *Biorheology*, vol. 44, p. 161, 2007.

[131] Zhao, R., Marhefka, J. N., Shu, F., Hund, S. J., Kameneva, M. V., and Antaki, J. F., "Micro–flow visualization of red blood cell–enhanced platelet concentration at sudden expansion," *Annals of Biomedical Engineering*, vol. 36, p. 1130, 2008.

[132] Zirnsak, M., Hur, D., and Boger, D., "Normal stresses in fibre suspensions," *Journal of Non-Newtonian Fluid Mechanics*, vol. 54, pp. 153–193, 1994.

VITA

JINGSHU WU

Born on November 14, 1978 in Guangji, Hubei Province, P. R. China, Jingshu Wu has always been interested in the fields of fluids and thermal sciences. He attended Department of Jet Propulsion at Beijing University of Aeronautics and Astronautics (BUAA), and received a Bachelor of Science in 2000. He was recommended to the graduate program of the same major after waiving the mandatory admission test, because of his excellent performance. He received the Master's degree in 2002 and published his first paper in AIAA Journal with his advisor, Dr. Xiaofeng Sun. He then pursued higher education after been accepted into the School of Aerospace Engineering at Georgia Institute of Technology (GATECH), where he received a Master's degree in 2004 under the tutelage of Dr. Lakshmi Sankar. Jingshu married Dan Wan in 2003. He was then admitted into the Georgia Tech School of Mechanical Engineering, for PhD study under Dr. Cyrus Aidun. In the Spring of 2010, he was awarded a Doctorate of Philosophy in Mechanical Engineering.